Velocity control of single-rod hydrostatic actuators: component sizing and controller design

by

Moosa Rafiq

A Thesis submitted to Faculty of Graduate Studies in partial fulfillment of the requirements for the degree of

Master of Science

Department of Mechanical Engineering

University of Manitoba

Winnipeg, Manitoba, Canada

Abstract

Pump-controlled hydraulic actuation of single-rod actuators is more challenging than double-rod actuators due to difference in areas on two sides of single-rod actuators and a need to compensate for differential flow. The performance of a single-rod pump-controlled hydraulic circuit can be significantly affected by variations in load, velocity and circuit design. Designing a simple-to-implement velocity controller for such hydraulic configurations is challenging under these conditions. This thesis presents velocity control of two typical hydraulic circuits; one is commonly used while the other is a novel design. Two issues involved are controller design and component sizing.

The design of velocity controllers is based on Quantitative Feedback Theory (QFT) as the design criteria are graphically illustrated for whole range of plant uncertainties in this design procedure. In order to design QFT controllers for closed-loop velocity control of pump-controlled single-rod hydraulic actuators, smooth open loop performance of hydraulic circuit becomes important. Hence component sizing, i.e., choosing optimal hydraulic components and having an optimal hydraulic design becomes necessary. Hence, a methodology to choose hydraulic components and hence improve system performance is proposed. First, a mathematical model of hydraulic circuit is developed, which is later used in simulations. Next, initial values of selected parameters of circuit components (pilot operated check valves and counterbalance valves) to be used in system are chosen based on manufacturer's specifications, experimental data and conservative judgement. This is followed by choosing few parameters which need to be optimised. Next, an optimisation algorithm is used on the simulation model to optimize parameters chosen based on an optimization criteria. In optimization, particle swarm optimization (PSO) and modified Nelder-Mead (MNM) algorithms are used to obtain smooth, least jerky system performance.

Next QFT Controllers are designed based on uncertainties found where families of transfer functions are to be obtained. For this purpose, system identification is used in order to obtain frequency responses from measured data and hence uncertainties. All the development reported

in this research is experimentally validated. First hydraulic circuit is a commonly used circuit incorporating pilot-operated check valves, while as the second novel circuit uses counterbalance valves. A multistep polynomial input and an alternating step input under different loading conditions is used. In this research a maximum of ten parameter optimization is used.

Acknowledgments

First I would like to thank my advisor, Professor Nariman Sepehri, for his supervision, advice and support. From him, I learnt a lot about problem solving approach and presenting my research. His expertise and knowledge has been a great help in my Master's program. I would also like to thank the members of dissertation committee: Dr. Q. Peng and Dr. U. Anakkage for their help and support.

I would like to thank Ahmed Imam at fluid power and tele-robotics research laboratory U of M for his help, valuable suggestions and friendship. I would like to thank Khurram Butt for his help and support. I would like to thank Ali Maddahi for his support during my research. I would like to thank G.Ren for being a wonderful friend. I would like to thank Y.Cai, George, X.Kaiwen and M.Maziar for always being there for my help. I wish them all the best for their future endeavors. Apart from being colleagues, they have been my best friends throughout my stay at U of M!

I would like to thank my family, especially my parents, who have always been there for my support. I would also like to thank my friends who have helped and supported me always.

Thanks!

Table of Contents

List of figures

List of Tables

Nomenclature

MNM	Globalized and bounded Nelder-Mead algorithm with deterministic restarts
PSO	Particle swarm optimization algorithm
$P(s,\gamma)$	Plant
$P(s,\alpha)$	Uncertainty in Plant for configuration 1
$P(s,\beta)$	Uncertainty in Plant for configuration 2
POCV	Pilot operated check valve
CBV	Counter balance valve
α_r	Area ratio A_b/A_a
C_H	Hydraulic compliance
τ_p	Time constant for pump
β_p	Normalized pump displacement
POCV	Pilot operated check valve
CBV	Counter balance valve
Δ PP	Pressure differential across pump(P_a - P_b)
Q_{quad1}	Quadrant 1
Q_{quad2}	Quadrant 2
Q_{quad3}	Quadrant 3
Q_{quad4}	Quadrant 4
F_L	Load due to external mass attached
k_1	Coefficient relating flow area to effective pressure on $POCV_A$
k_2	Coefficient relating flow area to effective pressure on $POCV_B$
A_{max1}	Maximum opening area of $POCV_A$
A_{max2}	Maximum opening area of $POCV_B$
p_{max1}	Effective pressure when $POCV_A$ undergoes full cracking
p_{max2}	Effective pressure when $POCV_B$ undergoes full cracking
K_{pilot1}	Pilot ratio of $POCV_A$
K_{pilot2}	Pilot ratio of $POCV_B$

p_{cr1}	Cracking pressure of $POCV_A$
p_{cr2}	Cracking pressure of $POCV_B$
A_{max3}	Maximum opening area of CBV_A
A_{max4}	Maximum opening area of CBV_B
p_{max3}	Effective pressure when CBV_A undergoes full cracking
p_{max4}	Effective pressure when CBV_B undergoes full cracking
K_{pPOCV}	Pilot ratio of POCV on either side of the hydraulic circuit
s_3	Number of rotations for CBV_A
s_4	Number of rotations for CBV_B
Q_{pmp}	Output flow from pump
v_e	Input signal (volt)
x_1	Actuator displacement (m)
x_2	Actuator velocity (m/s)
A_a	Area of actuator on cap side
A_b	Area of actuator on rod side
L_s	Length of stroke(m)
T	Sweep record length(s)
ω_{max}	Maximum frequency tested
ω_{min}	Minimum frequency tested
k_{oil}	Bulk modulus(Pa)
ρ	Density of hydraulic oil
p_c	Charge pressure(Pa)
M	External load attached
m	Equivalent mass of piston and rod
f_v	Vicious friction coefficient
f_c	Coulomb friction coefficient
f_{c0}	preload force
A_1	Area of pilot check valve 1
A_2	Area of pilot check valve 2

A_3	Area of pilot assisted part of CBV_A
A_4	Area of pilot assisted part of CBV_B
A_5	Area of check valve part of CBV_A
A_6	Area of check valve part of CBV_B
k_{pmp}	Gain relating pump flow and input voltage
p_{e1}	Effective pressure for $POCV_A$
p_{e2}	Effective pressure for $POCV_B$
p_{e3}	Effective pressure for CBV_A
p_{e4}	Effective pressure for CBV_B

List of constants used

A_a	$31.67 \times 10^{-4}\ m^2$
A_b	$23.75 \times 10^{-4}\ m^2$
L_s	0.54 m
T	70 s
ω_{max}	18.85 Rad/s
ω_{min}	0.37 Rad/s
k_{oil}	1.2×10^9 N/m^2
ρ	860 Kg/m^3
p_c	14.48×10^5 N/m^2
c_m	95.3
M	41-368 kg
M_{eq}	80 kg
f_v	2000 N/m/s
f_c	10^{-6} N/Pa
f_{c0}	250 N
A_{PC1}	$0.44^{-4}\ m^2$
A_{PC2}	$0.44^{-4}\ m^2$
A_3	$0.385^{-4}\ m^2$
A_4	$0.385^{-4}\ m^2$
k_{pmp}	$105 \times 10^{-6}\ \frac{m^3}{s}/V$
k	$8.33 * 10^{-11}$
k_L	-95.3×m
C_d	0.61

Chapter 1

Introduction

1.1. Problem statement

Single-rod hydraulic actuators are used in various applications like aviation, agriculture, food processing, oil and construction. Metering valves used in such hydraulic systems can decrease the energy efficiency by approximately 35% [1, 2]. Hence pump-controlled hydraulic actuation is discussed in this research as it is energy efficient. Various hydraulic configurations have been designed and tested using single-rod actuators [2-6]. The performance of these hydraulic configurations is significantly affected by variations in load, velocity and hence operational quadrants. The area difference between two sides of a single-rod actuator results in flow differential across actuator. As such three types of challenges are encountered. First, the design of hydraulic circuit. Secondly, the selection of optimal hydraulic components (component sizing). Lastly, velocity control in such systems is challenging as well. Hence designing a simple-to-implement velocity controller for such hydraulic configurations becomes important. The circuit design (number and specifications of hydraulic components used in a particular hydraulic configuration in context) is chosen primarily based on experience. As such, many hydraulic circuit designs proposed make it pretty hard to decide which design is the optimal one for a particular application. This provides motivation for the proposed research where optimal hydraulic circuit design and closed loop velocity control are discussed.

1.2. **Methodology** (Proposed solution)

In this research a methodology to choose optimal hydraulic component parameters (sizing), via optimal component selection is proposed. As such choosing hydraulic components becomes easier. This is followed by designing velocity controllers for closed loop control. Starting from mathematical modelling of the system, the values of various parameters of components to be

used in the hydraulic design are obtained through experiments, manufacturer's specifications or conservative judgement. In order to optimize the performance of system, few important parameters are chosen based on parametric identification and optimisation criteria (Sections 5.1). The optimal design is tested at different loads and velocities in simulation as well as in experiments. The proposed solution will help in choosing the optimal hydraulic components which result in better performance in open loop. This is followed by system identification where frequency responses and as such range of uncertainties in the system transfer functions are used for designing a controller. Designing a simple-to-implement controller is possible due to CIFER (comprehensive identification from frequency responses) system identification technique where an equivalent low order transfer function is obtained to represent the system, which otherwise can be a higher order system.

1.3. Objectives of this thesis

The primary objective of this research is to develop simple-to-implement QFT velocity controllers for the class of single-rod hydraulic actuations. The secondary objective of this research is to propose a methodology for choosing optimal hydraulic component parameters (optimal sizing of hydraulic components) for a given configuration. Effects of load and velocity variations will be taken into account. Results in both cases are verified using simulation and experimental tests. Two configurations will be considered to demonstrate the development in this thesis, the first uses pilot operated check valves and the second uses counterbalance valves.

Important questions that will be addressed in this research are:

1. How can we design a simple-to-implement velocity controller for a single-rod hydraulic configuration where variations in load, velocity and circuit design are taken into account?
2. How can we choose optimal hydraulic components for a given hydraulic configuration?
3. How does system identification help us to distinguish between different hydraulic configurations?
4. Can undesirable performance in certain regions of operation be removed by optimisation?

1.4. Thesis outline

Chapter 2 includes the literature review of this thesis. Chapter 3 presents modelling of two hydraulic configurations of interest. Chapter 04 includes description of test rig. Next, a methodology is proposed for selection of hydraulic components which is presented in chapter 05. Results obtained before and after optimization using simulation and experimental tests are discussed. In chapter 06, system identification technique is used to find transfer functions of two hydraulic configurations. Here input chirp excitation signals are used to obtain parametric uncertainties in the system. Next controllers are designed for both configurations. Simulation and experimental tests are used for validation. Finally, in chapter 7 conclusions is presented and suggestions for future work are discussed.

Chapter 2

Single Rod Hydrostatic Actuation: Design, Sizing and Control

Hydraulic actuation systems use hydraulic pressure to drive an output member or transmit power by using pressurized fluids. Main advantages of using hydraulic actuation systems are high power to weight ratio, high stiffness and stability. Hydraulic circuits can be valve controlled or throttle-less (pump-controlled). Valve-controlled hydraulic configurations are inefficient as compared to valveless, due to the power losses in throttling valves. Approximately one third of the energy delivered to hydraulic system gets used in just heating up the hydraulic oil in metering valves[1,2]. Hence valve-controlled hydraulic circuit configurations can be replaced by pump-controlled hydraulic circuits for higher efficiency. Pump controlled hydraulic systems or electro-hydrostatic systems or throttle-less hydraulic systems [7] supply fluid directly to the cylinder without using central hydraulic power unit. When the pump is fixed displacement and prime mover is a variable revolutions per minute (RPM) motor, the system is known as variable speed pump-controlled system. When the actuator is controlled with a variable displacement pump and prime mover is a fixed revolutions per minute (RPM) motor, then the circuit is known as VDPC system or variable displacement pump-controlled hydraulic system.

Hydraulic actuators used widely can be either single-rod (asymmetric) or double rod (symmetric) as shown in Figure 2.1. Double rod actuators are used widely in aircraft industry as they take less space and are more compact. The applications include Airbus and F-35 fighter [4, 8]. However, single-rod cylinders are used in 80% of electrohydraulic applications [9]. They find a wide variety of applications in various industries and construction equipment. The main problem in pump-controlled single-rod actuators is the flow differential across the two ends of actuator due to area difference, which may result in poor performance under certain loading conditions.

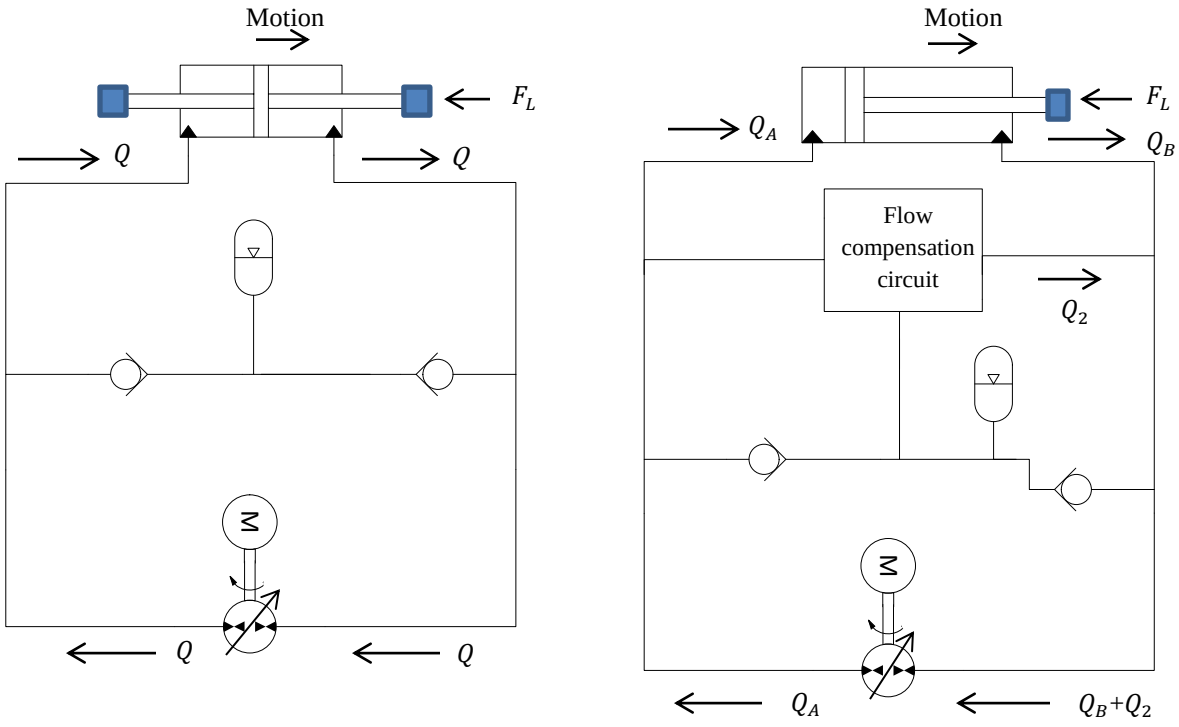

(a) (b)

Figure 2.1 Typical pump-controlled actuation: (a) double rod system; (b) single-rod system.

Figure 2.2 (a) shows a hydraulic circuit designed for a hydraulic flight simulator to control hydraulic actuators on a stewart platform [10]. But this design used two fixed displacement pumps. Figure 2.2 (b) shows a hydraulic circuit which used a 3-way 2-position shuttle valve to compensate differential flow rates of a single-rod actuator [11]. This circuit used a bi-directional pump/motor and can be used under variable loading conditions. Figure 2.2 (c) shows a hydraulic circuit configuration with two pilot operated check valves that consists of a variable displacement pump in order to fix the flow differential problem in case of single-rod cylinders has been designed [12]. A variable displacement pump was used and pump operated in 4 quadrants.

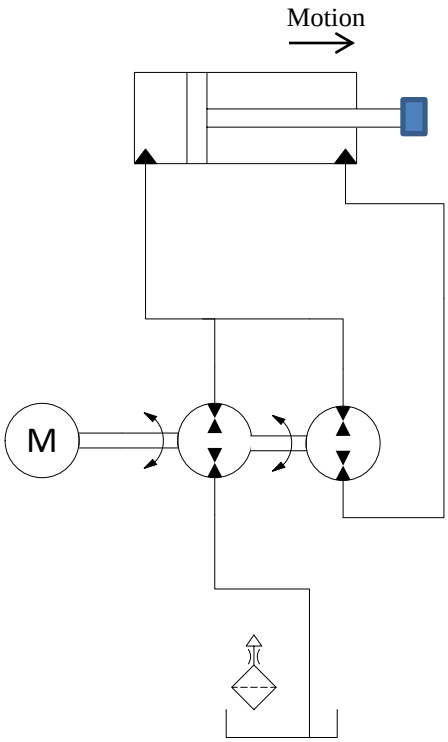

(a)

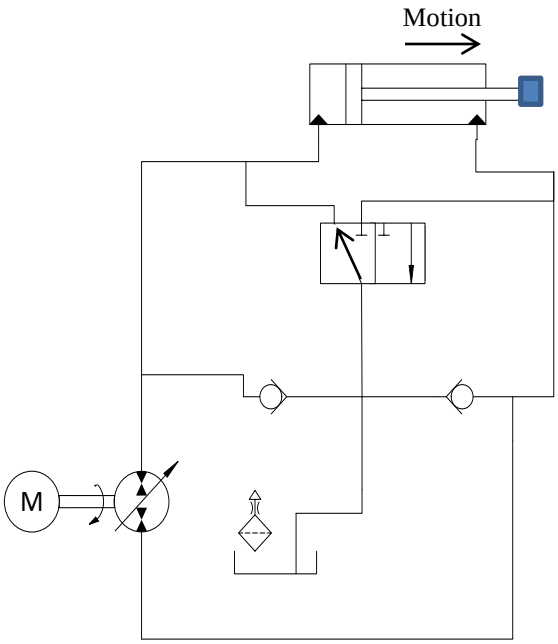

(b)

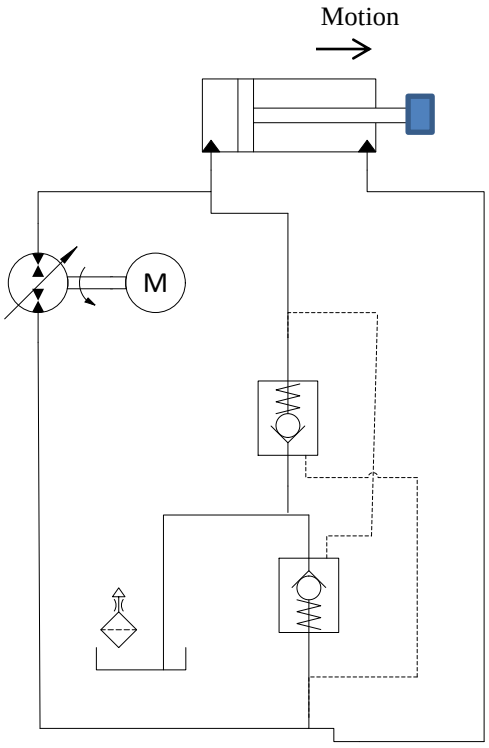

(c)

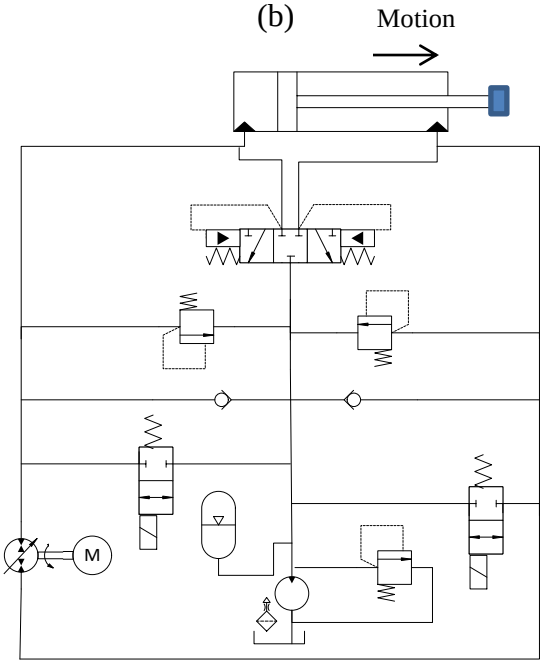

(d)

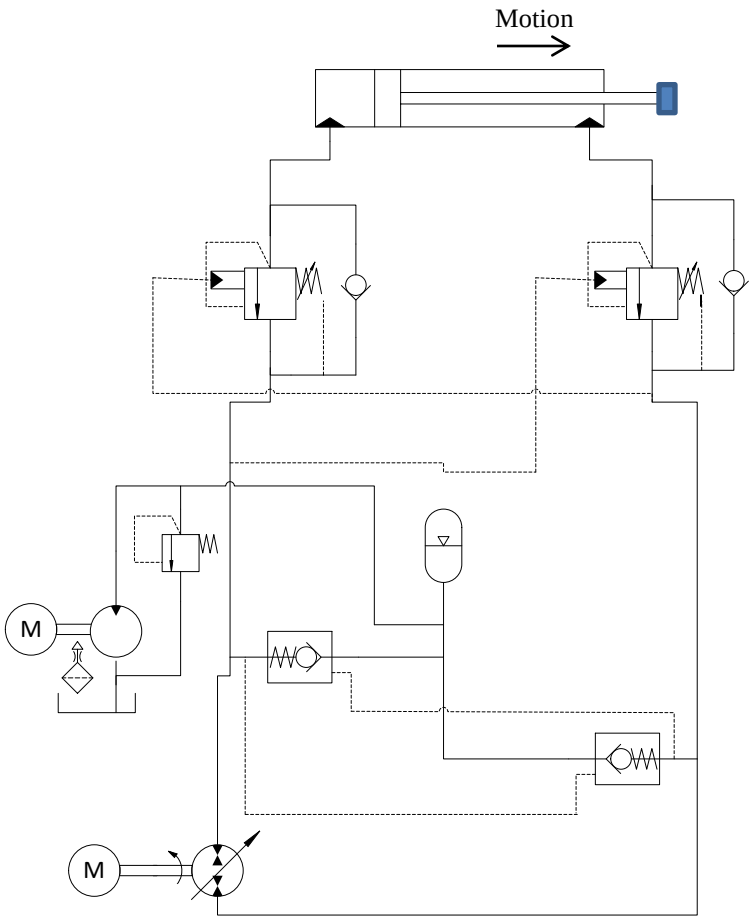

(e)

Figure 2.2 Hydraulic circuit configurations: (a) hydraulic circuit using two pumps; (b) hydraulic circuit using 3-way 3-position shuttle valve with two regulating valves; (c) two pump control of a single-rod actuator shown; (d) hydraulic circuit using pilot check operated valves; (e) hydraulic circuit using counterbalance valves.

Figure 2.2 (d) shows a 3/3 closed-center shuttle valve used to compensate for flow differential [3]. Here two regulating valves were added to allow metered leakage in order to improve stability. An open center shuttle valve was also used to incorporate leakage which improved stability [13]. It was reported that under low loading conditions, the configuration with two pilot operated check valves is not stable [14, 3].

Different hydraulic circuit designs were proposed regulating load motion with the help of counter balance valve [15, 4, 5]. In 2017 it was reported that the problem can be fixed by proper utilisation of counterbalance valves [6]. Two throttling valves were used to improve the stability of hydraulic circuit by using limited throttling at critical regions (Figure 2.2e). In this thesis two

hydraulic circuit designs are discussed. Circuit configuration 1 [12] where pilot operated check valves are used and circuit configuration 2 [6] where counterbalance valves are incorporated into the hydraulic circuit.

As hydraulic valves are important components of any hydraulic system, they can be configured in different ways to get desired performance. More hydraulic valves in the hydraulic configuration means more possibilities of different hydraulic designs and hence need for optimisation. Various optimisation techniques have been developed. Particle swarm optimisation (PSO) technique is easy to implement, having fast convergence, hence making it highly useful in engineering applications [16-18]. It is a metaheuristic which is able to search a large complex candidate solutions. Various optimisation techniques (like PSO) with muti-objective optimisation have been developed [19,20] In some cases we may be interested to determine global and local objective functions whereas in other cases we may use decomposition approach where Multiple objective optimisation problems are converted into various single objective optimisation problems. Various factors such as how quickly the problem is solved, accuracy and number of iterations are important in choosing an optimisation technique. The iterative runs for online tuning methods based on heuristics and metaheuristics are time consuming and results in high costs usually [21]. Nelder-Mead method or downhill simplex method is used to find minimum or maximum of an objective function in a multidimensional space. It is a heuristic and can be applied to non-linear optimisation problems (local exploitation method in deterministic optimisation).For global optimization of multiminima functions a two process algorithm known as continuous hybrid algorithm was developed [22]. A globalised and bounded Nelder-Mead algorithm with deterministic restarts (MNM) was developed [21]. It globalises Guin augmented [23] variant of Nelder-Mead algorithm sequentially by deterministic restarts. This algorithm exploits the simplicity of search space formed by simple bounds on design variables for deterministic restarts. It is a model based, globalized local search, multimodal optimization method. It uses reflection, expansion, contraction and shrinkage. It has been used effectively in case of robust non-linear SMC (sliding mode control) control for pneumatic equipment with variable load. In this research, the results obtained by using this algorithm have been compared

with PSO in this work, and later only MNM method has been used, as it proves to be much faster than PSO.

In order to control the velocity of actuators in hydraulic systems, a stable and robust controller is needed. The hydraulic systems are subjected to different uncertainties. These can be due to friction, external disturbances and leakage (internal/ external). Lyapunov controllers guarantee nonlinear stability at high computational burden and increase in complexity cost [24]. QFT controllers have been developed with low computational burden, although they may work in certain range of uncertainties [25-27]. Designing a QFT velocity controller for a single-rod system is challenging due to difference in areas on two sides of single-rod actuator. Designing a controller which is simple in structure is another challenge. Hence there is a need for a simple and robust velocity controller that can improve performance of single-rod hydraulic systems.

Chapter 3

Modelling of single-rod hydraulic circuit actuations

In this chapter two hydraulic circuit configurations are discussed followed by their mathematical models for simulation purposes.

3.1. Configuration 1

Figure 3.1 shows a hydraulic circuit for actuating a single-rod cylinder where pilot operated check valves are used (configuration 1). Pump delivers flow Q in clockwise direction pumping fluid towards cap end of actuator during extension.

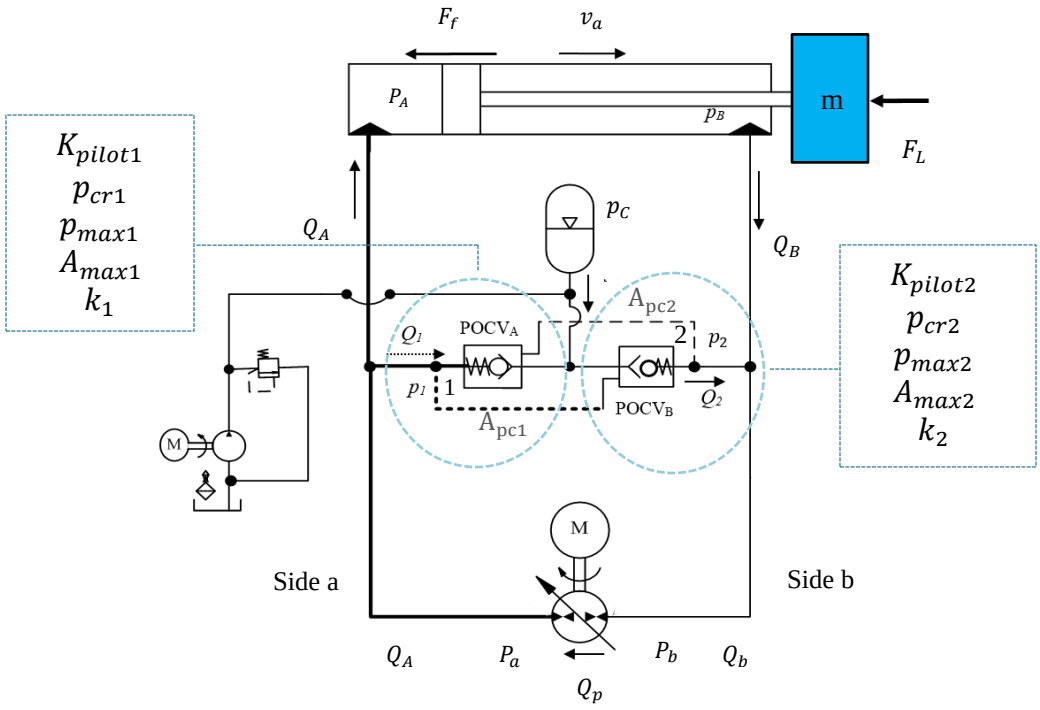

Figure 3.1 Circuit working with pilot-operated check valves (Configuration 1).

As pressure increases on side 'a' of configuration, $POCV_B$ (Pilot Operated Check Valve on side 'b') opens up via pilot to compensate for the differential flow. Complete working cycle is described in [6].

Dynamics of actuator and flow continuity equations are described below. Here 'm' represents equivalent moving mass of piston and rod. p_A and p_B are pressures on two sides of actuator. p_a and p_b are pressures on each side of pump as shown in Figure 3.1. A_a and A_b are effective piston areas. K_{oil} is bulk modulus of oil, V_A and V_B represent volume of oil on each side of actuator.

$$m\dot{v}_a = (p_A A_a - p_B A_b) - F_f - F_L \tag{3.1}$$

$$\dot{p_A} = \frac{K_{oil}}{V_A}(Q_A - A_a v_a) \tag{3.2}$$

$$\dot{p_B} = \frac{K_{oil}}{V_B}(-Q_B + A_b v_a) \tag{3.3}$$

where V_A and V_B are given by following equations:

$$V_A = V_{01} + (A_a x_a) \tag{3.4a}$$

$$V_B = V_{02} - (A_b x_a) \tag{3.4b}$$

Where V_{01} and V_{02} are measured when cylinder is in mid stroke. Friction force denoted by F_f is summation of Stribeck, Coulomb and viscous friction components. F_C denotes the coulomb friction, k_{br} and c_{va} denote breakaway friction force and velocity transition coefficients, f_v and f_c are viscous and coulomb friction coefficients, f_{c0} represents preload force during cylinder installation due to seal deformation [6].

$$F_f = F_C\,(1 + (k_{br} - 1)e^{-c_{va}\ mod(v_a)})(sign\ v_a) + f_v v_a \tag{3.5}$$

$$F_C = f_{c0} + f_c(p_A + p_B) \tag{3.6}$$

Q_A , Q_B , Q_a, Q_b, Q_1 and Q_2 denote flows across actuator, across pump and points 1 and 2 shown in circuit configuration 1 diagram.

If p_c , p_1 and p_2 represent charge pressure, pressure at points 1 and 2, respectively (Figure 3.1); then flow across POCV valves is given by equations as follows:

$$Q_1 = C_d\ A_{PC1}\sqrt{\frac{2}{\rho}(p_1 - p_c)} \tag{3.7}$$

$$Q_2 = C_d\, A_{PC2}\sqrt{\frac{2}{\rho}}(p_2 - p_c) \tag{3.8}$$

where A_{PC1} and A_{PC2} represents areas of $POCV_A$ and $POCV_B$ respectively. The effective cracking pressure (p_{ePOCV}) of POCV on either side (i) is based on equation as follows:

$$p_{ePOCV} = K_{pPOCV}\,(p_{pilot} - p_c) - (p_i - p_c) \tag{3.9}$$

provided $p_i \geq p_c$ or else is given by $p_{ePOCV} = (p_c - p_i)$ where p_i denotes pressure on valve side (p_1 or p_2 in Figure 3.1), p_{c} denotes the charge pressure, $\mathrm{p_{ePOCV}}$ is effective pressure of POCV i.e. p_{e1} or p_{e2} for $POCV_A$ and $POCV_B$ respectively. K_{pPOCV} is the pilot ratio of POCV on either side i.e. K_{pilot1} and K_{pilot2} for $POCV_A$ and $POCV_B$ respectively. p_{pilot} represents pressure via pilot line for POCV. The relationship between area of valve and effective cracking with respect to cracking pressure is assumed to be proportional as given below:

$$A_{POCV} = k_{POCV}(p_{ePOCV} - p_{crPOCV}) \tag{3.10}$$

where A_{POCV} represents area of POCVs i.e. A_1 or A_2, while as p_{crPOCV} denotes cracking pressure p_{cr1} and p_{cr2} for $POCV_A$ and $POCV_B$ respectively. k_{POCV} is the coefficient relating flow area to effective pressure, denoted by k_1 and k_2 for $POCV_A$ and $POCV_B$ respectively. If $p_{\mathrm{e1}} \leq p_{\mathrm{cr1}}$, then flow across POCV is assumed to be zero. $A_1 = A_{max1}$ if $p_{e1} = p_{max1}$, where p_{max1} is the effective pressure when $POCV_A$ undergoes full cracking and A_{max1} represents maximum opening area. Same applies to A_2. The pressure drops at two ends of transmission lines are calculated using lumped resistance model as follows:

$$\Delta p = C_{Tv}\ Q + C_{Tl}\ Q^2 \tag{3.11}$$

where C_{Tv} and C_{Tl} denote combined viscous friction and local drag coefficients.

3.2. Configuration 2

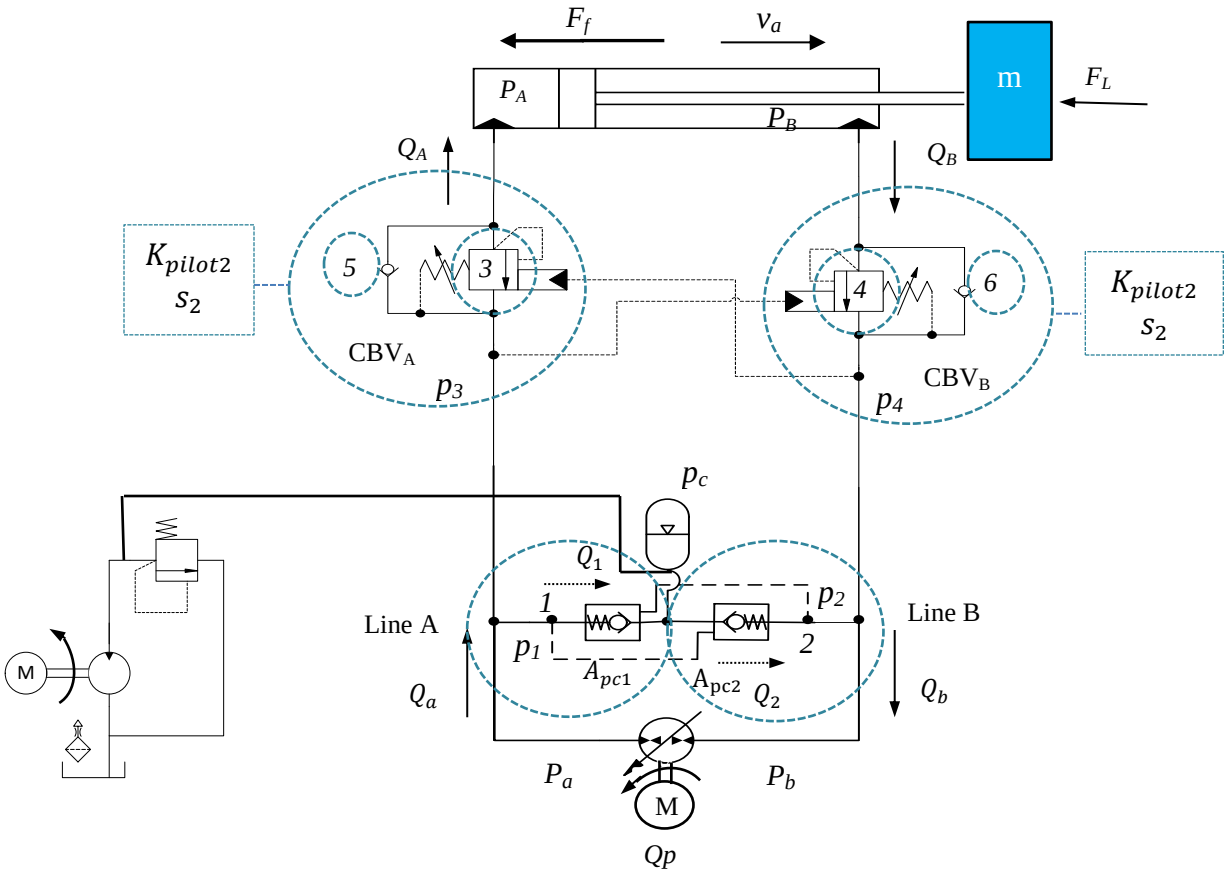

Figure 3.2 Circuit working with counterbalance valves (Configuration 2): 1, 2. Piot operated check valves A and B; 3, 4. Pilot assisted areas of counter balance valves A and B; 5, 6. Check valve areas of counter balance valves A and B.

In Figure 3.2 two counter balance valves (CBVs) are added, which act as resistance to flow and also restricts the flow in one direction of motion. Complete working cycle is described in [6]. Dynamics of actuator and flow continuity equations are described below for configuration 2:

$$m\dot{v}_a = (p_A A_a - p_B A_b) - F_f - F_L \tag{3.12}$$

terms used in equation 3.12 have same meaning as in configuration 1

$$\dot{p_A} = \frac{K_{oil}}{V_A}(Q_A - A_a v_a) \tag{3.13}$$

$$\dot{p_B} = \frac{K_{oil}}{V_B}(-Q_B + A_b v_a) \tag{3.14}$$

Here Q_A and Q_B denote flows across counterbalance valves

$$\dot{p_a} = \frac{K_{oil}}{V_{03}}(Q_a - Q_1 - Q_A) \tag{3.15}$$

$$\dot{p_b} = \frac{K_{oil}}{V_{04}}(Q_B + Q_2 - Q_b) \tag{3.16}$$

Q_a, Q_b, Q_1 and Q_2 denote flows across pump and POCV valves. Flow across CBV_A and CBV_B (Figure 3.2) is given by the following equations:

$$Q_A = C_{35}\, A_{VA} \sqrt{\frac{2}{\rho}(p_3 - p_A)} \tag{3.17}$$

$$Q_B = C_{46}\, A_{VB} \sqrt{\frac{2}{\rho}(p_B - p_4)} \tag{3.18}$$

where A_{VA} and A_{VB} are the areas of CBV_A and CBV_B, C_{35} and C_{46} are flow coefficients, p_3 and p_4 are the pressures at counter balance valves as shown in Figure 3.2. The effective cracking pressure (p_{eCBV}) of CBV on each side is based on equations as follows:

$$p_{eCBV} = (K_{pCBV} \times p_{pilot}) + p_{load} \tag{3.19}$$

where p_{eCBV} represents p_{e3} or p_{e4} for CBV_A and CBV_B respectively. K_{pCBV} is the pilot ratio of CBV_A and CBV_B respectively i.e. K_{pilot3} and K_{pilot4}. p_{pilot} represents pressure via pilot line for CBV. p_{load} denotes the pressure due to load. The relationship between area of valve and effective cracking with respect to cracking pressure is assumed to be proportional as given below:

$$A_{CBV} = k_{CBV}(p_{eCBV} - p_{crCBV}) \tag{3.20}$$

where A_{CBV} represents area of CBVs, p_{crCBV} denotes cracking pressures of CBV_A and CBV_B. k_{CBV} is the coefficient relating flow area to effective pressure, for each POCV, p_{eCBV} denotes effective cracking pressure of CBV on each side.

A_{CBV} for each valve is further divided into two areas as shown in Figure 3.3. CBV_A comprises of throttled pilot assisted area (A_3) and check valve area (A_5) represented by:

$$A_3 = k_3(p_{e3} - p_{cr3}) \tag{3.21}$$

$$A_5 = k_5(p_{e5} - p_{cr5}) \tag{3.22}$$

k_3 and k_5 are coefficients relating flow area to effective pressures, p_{e3} and p_{e5} denote two effective cracking pressures of two areas, p_{cr3} and p_{cr5} denote cracking pressures. Areas $A_3$and $A_5$are also shown in Figure 3.2 numbered 3 and 5 respectively. Similarly, for CBV_B area is subdivided into two areas A_4 and A_6.

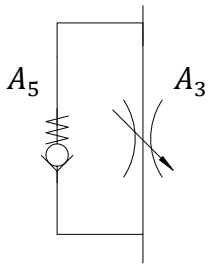

Figure 3.3 Areas shown in a counterbalance valve.

For CBV_A, $A_3 = A_{max3}$ if $p_{e3} = p_{max3}$ where p_{max3} is the effective pressure when valve undergoes full cracking, A_{max3} is maximum opening area of valve.

Cracking pressure of CBV_A and CBV_B depends upon number of rotations the valve is set at as follows:

$$p_{cr3} = p_{\min\_set\_3} + s_3 \times p_{turn\_3} \tag{3.23}$$

$$p_{cr4} = p_{\min\_set\_4} + s_4 \times p_{turn\_4} \tag{3.24}$$

where p_{cr3}, $p_{\min\_set\_3}$, s_3 and p_{turn_3} represents cracking pressure, minimum pressure setting, number of rotations and pressure increase in each rotation for CBV_A (A_3). Similarly, p_{cr4}, $p_{\min\_set\_4}$, s_4 and p_{turn_4} represents cracking pressure, minimum pressure setting, number of

rotations and pressure increase in each rotation for CBV_B (A_4). The flow equations of POCV valves and their cracking criteria remain same as discussed in circuit configuration 1.

Table 3.1 shows the list of parameters chosen in two circuits which will be used in optimization.

Table 3.1. List of parameters chosen in two circuits which will be used in optimization.

Configuration 1		
S.No.	Parameters	Nomenclature
1.	K_{pilot1}	Pilot ratio of $POCV_A$
2.	K_{pilot2}	Pilot ratio of $POCV_B$
3.	p_{cr1}	Cracking pressure of $POCV_A$
4.	p_{cr2}	Cracking pressure of $POCV_B$
5.	p_{max1}	Effective pressure when $POCV_A$ undergoes full cracking
6.	p_{max2}	Effective pressure when $POCV_B$ undergoes full cracking
7.	A_{max1}	Maximum opening area of $POCV_A$
8.	A_{max2}	Maximum opening area of $POCV_B$
9.	k_1	Coefficient relating flow area to effective pressure on $POCV_A$
10.	k_2	Coefficient relating flow area to effective pressure on $POCV_B$
Configuration 2		
1.	K_{pilot1}	Pilot ratio of CBV_A
2.	K_{pilot2}	Pilot ratio of CBV_B
3.	s_3	Number of rotations for CBV_A
4.	s_4	Number of rotations for CBV_B

Chapter 4

Description of Test Rig

Figure 4.1 shows the test rig used in this research. The test rig consists of a John-Deere backhoe attachment (JD-48) on a frame. The main components of this system are single-rod actuator, variable displacement pump, a charge pressure unit, pressure transducers and displacement sensor. Specifications of these components are given in table 4.1

A variable displacement swash plate pump is used with a charge circuit. Charge circuit ensures that a constant charge pressure is maintained which is essential for the case drain of pump and is used for flow compensation as well. Pressure transducers are used to measure pressures across the actuator and at pump ports. Velocity is measured from encoder using regression method. Two hydraulic circuit configurations tested include two important circuit components i.e. pilot operated check valves and counterbalance valves. They are used as part of main circuit with swash plate pump. Each cycle of operation is divided into four quadrants a shown in Figure 4.2 and 4.3. ΔP_P represents pressure differential across pump (P_a - P_b) and Q_{pmp} represents flow at pump port (assuming $Q_a = Q_b$); clockwise being positive direction for flow. Then, pump is working in pumping mode if both ΔP_P and Q_{pmp} have same sign. Otherwise the pump is assumed to be working in motoring mode. If actuator velocity (v_p) and load due to external mass attached (F_L) is having same sign, then actuator is assumed to be working in resistive mode of operation. Otherwise, actuator is working in assistive mode.

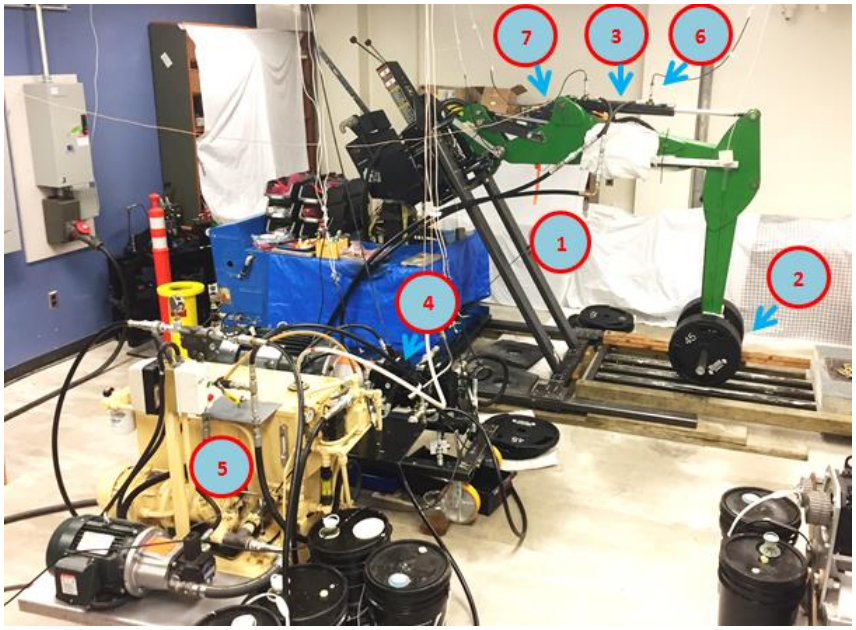

Figure 4.1 Experimental test rig: Main components; (1) frame; (2) load; (3) single rod actuator; (4) variable displacement pump; (5) charge pressure unit; (6) pressure transducers; (7) displacement sensors.

Table 4.1. Specifications of main components of experimental test rig.

1	JD-48 backhoe with frame	
2	Load attached	41-368 kg
3	single-rod actuator (Area of cap-side, area ratio and length of stroke)	31.67 cm^2, 0.75, 55 cm
4	Variable displacement pump	28 cm^3/rev variable swash plate piston pump (Sauer-Danfoss 42 series) coupled with 50 hp, 1775 rpm induction motor (Toshiba 320 TC)
5	Charge pressure unit	1.25-1.96 MPa adjustable pressure van pump (Northman VPVC-F40-A1)
6	Pressure transducer	Ashcroft K1, accuracy 0.5% at 3000 psi
7	Displacement sensor	Bourns, accuracy 5 μm

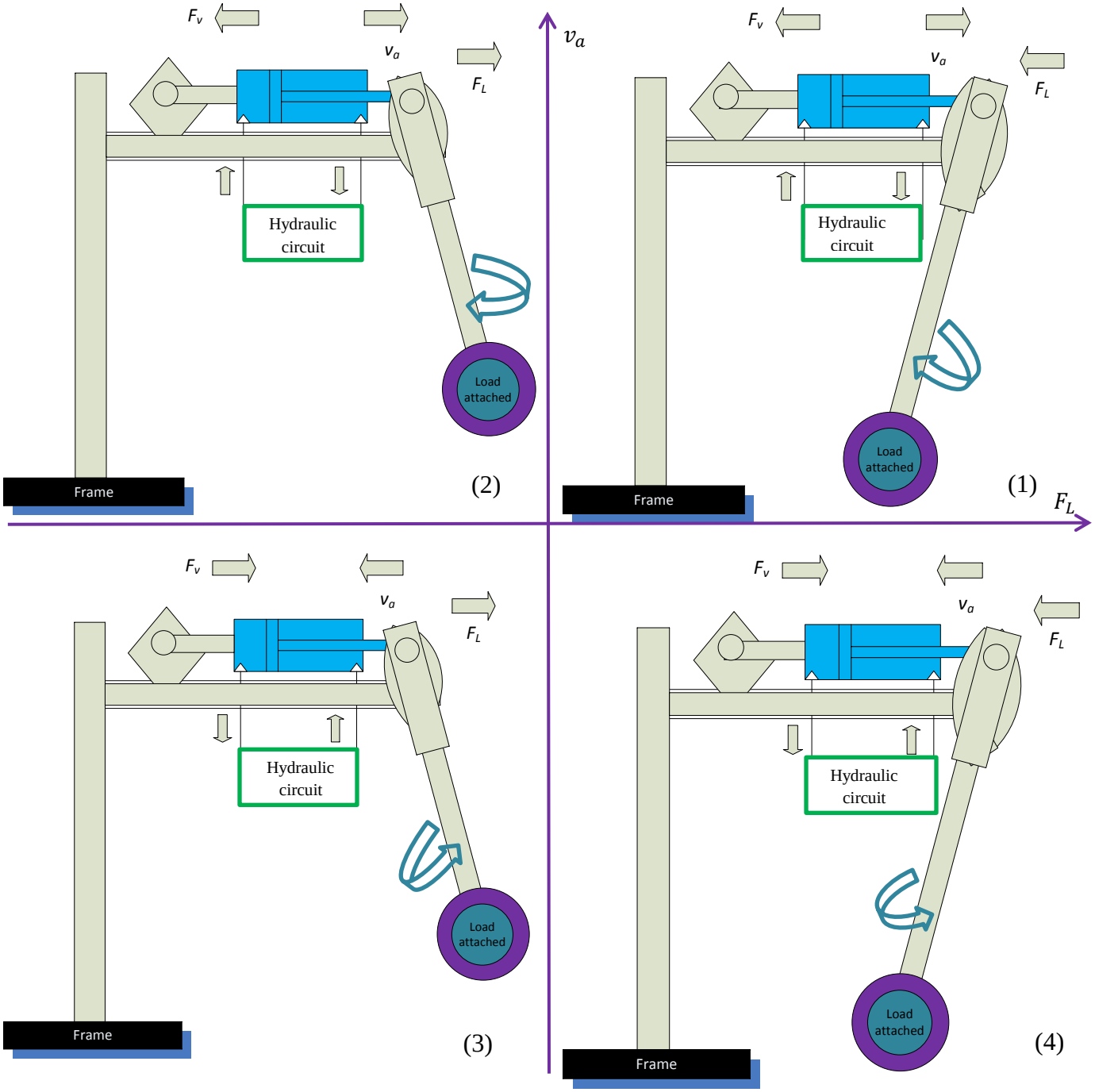

Figure 4.2 Four quadrants operation for test rig.

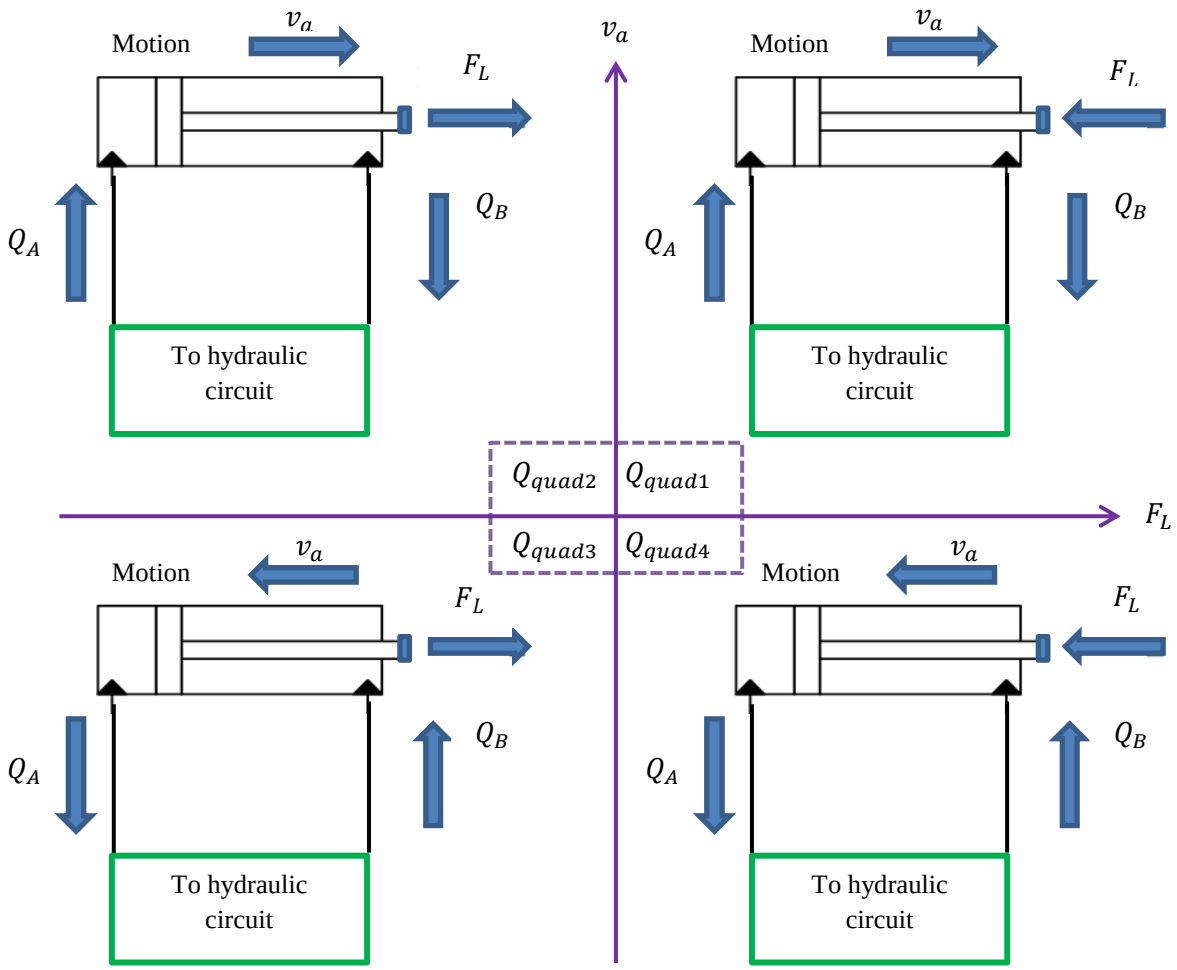

Figure 4.3 Flow directions of hydraulic circuit in four quadrants of operation.

In quadrant 1(Q_{quad1} in Figure 4.3) actuator undergoes extension (as it moves towards right) where load (due to external mass attached) is resistive. In quadrant 2 (Q_{quad2}) actuator undergoes extension (as it moves towards right) where load (due to external mass attached) is assistive. In quadrant 3 (Q_{quad3}) actuator undergoes retraction (as it moves towards left) where load (due to external mass attached) is resistive. In quadrant 4 (Q_{quad4}) actuator undergoes retraction (as it moves towards left) where load (due to external mass attached) is assistive.

Sequence of operation as external mass attached moves from center towards left, then right and back to center: 1.Q_{quad1} ; 2.Q_{quad4}; 3.Q_{quad3} ; 4.Q_{quad2} . Table 4.2 shows values of various parameters of the system.

Table 4.2. Values of various parameters of test rig.

Parameters	Values
A_a	$31.67 \times 10^{-4}\ m^2$
A_b	$23.75 \times 10^{-4}\ m^2$
L_s	0.54 m
p_c	14.48×10^5 N/m^2
c_m	95.3
m	41-368 kg
M_{eq}	80 kg
f_v	2000 N/m/s
F_L	95.3× c_m ×m
f_c	10^{-6} N/Pa
f_{c0}	250 N
k_{pmp}	$105 \times 10^{-6}\ \frac{m^3}{s}/V$

Chapter 5

Hydraulic component sizing

5.1. Proposed methodology for selection of components

In order to improve the performance, proper sizing of components is important in a hydraulic circuit. Hence selecting the optimal setting of components becomes important. First a mathematical model is needed for this purpose. Next, initial values and search space of different component parameters to be used in system are chosen, based on manufacturer's specifications, experimental observations and conservative judgement. This is followed by choosing few parameters which need to be optimised (initial component selection). Next, optimisation algorithms are used on the simulation model using proposed optimization criteria. Optimal settings obtained for component parameters are evaluated in simulation followed by experimental tests.

5.2. Initial component selection

Cracking pressures and maximum opening areas of POCV and CBV valves

In order to choose the initial values and search space for parameters which need to be optimized, experimental data, manufacturer's specifications and conservative judgement is used. Cracking pressures of pilot operated check valves are obtained from manufacturer's specifications. But in CBV valves cracking pressure is dependent on number of rotations the valve is initially set at. In order to find cracking pressure of CBV valves an example of high load is taken. A step input is used as shown in Figure 5.2. For CBV_A throttling area 3 (Figure 3.2), assuming throttled flow though area 3 only, we have:

$$A_3 = k_3(p_{e3} - p_{cr3}) \tag{5.1}$$

When $p_{e3} = p_{max3}$ then $A_3 = A_{max3}$ where p_{max3} is the effective pressure when valve undergoes full cracking, A_{max3} is maximum opening area of valve. Similarly, for CBV_B we have (assuming throttled flow though area 4 only):

$$A_4 = k_4(p_{e4} - p_{cr4}) \tag{5.2}$$

When $p_{e4} = p_{max4}$ then $A_4 = A_{max4}$ where p_{max4} is the effective pressure when valve undergoes full cracking, A_{max4} is maximum opening area of valve. Hence, Equations 5.1 and 5.2 are used to find values of k_3 and k_4. Two effective pressures p_{e3} and p_{e4} for two CBVs are calculated from regions marked 3 and 4 in Figure 5.2 and are calculated as:

$p_{e3} = p_A + p_b$ and $p_{e4} = p_B + p_a$ implies values of $p_{e3\_min}, p_{e3\_max}, p_{e4\_min}, p_{e4\_max}$ are 4.68 MPa (680 psi), 5.79 MPa(840) psi, 3.86 MPa(560 psi), 4.75 MPa (690 psi), respectively.

From the manufacturers' specifications, we know that each CBV valve has a minimum pressure setting of 1.37 MPa (200 psi) ($p_{min\_set\_3}$ and $p_{min\_set\_4}$) and total number of rotations (s_3 and s_4) in each CBV is five. Using equations 3.23 and 3.24 we have:

$p_{cr3} = p_{min\_set\_3} + s_3 \times p_{turn\_3} = 200 + 2 \times p_{turn\_3} = 200 + 480$ psi $= 4.68$ MPa

i.e. $p_{turn\_3} = 240$ psi (approx.) or 1.65 MPa

$p_{cr4} = p_{min\_set\_4} + s_4 \times p_{turn\_4} = 200 + 1.5 \times p_{turn\_4} = 200 + 360$ psi$= 3.86$MPa

i.e. $p_{turn\_4} = 240$ psi (approx.) or 1.65 MPa

where s_3 and s_4 denote number of rotations used in each CBV, p_{turn_3} and p_{turn_4} denote the pressure increase with each rotation, in each CBV.

We have $p_{e3\_min} = p_{cr3}$, $p_{e3\_max} = p_{max3}$, $p_{e4\_min} = p_{cr4}$, $p_{e4\_max} = p_{max4}$

implies p_{cr3} , p_{max3}, p_{cr4} , p_{max4} are 4.68 MPa (680 psi), 5.79 MPa(840 psi), 3.86MPa (560 psi), 4.75 MPa (690 psi) respectively.

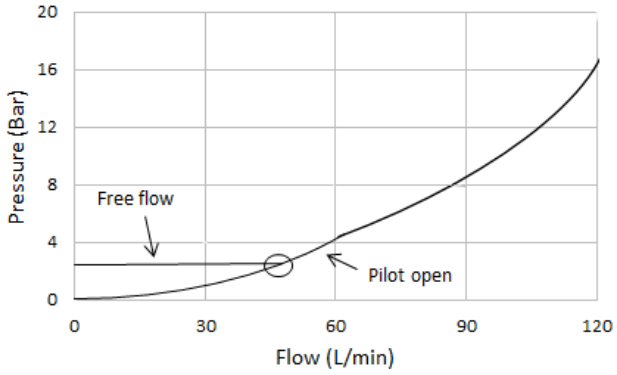

Figure 5.1 Pressure drop with flow graph for CBV [reproduced from catalogue www.sunhydraulics.com/model].

Also for area calculation of CBV, for linearized relationship around region encircled in Figure 5.1, from manufacturers specifications, $A_{max3} = A_{max4} = 38.7$ mm². Finally, the values of k_3 and k_4 obtained are 3.4878×10^{-11} and 4.296×10^{-11} respectively.

Similarly, for area calculation of POCV, $A_{max1} = A_{max2} = 44$ mm². Parameters like cracking pressures for pilot operated check valves are obtained from manufacturer which vary from a minimum of 0.3×10^{-5} Pa to a maximum of 7×10^{-5} Pa, where 2×10^{-5} Pa is used in circuits before optimization. Values of effective pressure when pilot operated check valves undergo full cracking is assumed to be a minimum of 0.75×10^{-5} Pa to a maximum of 17.5×10^{-5} Pa. For counterbalance valves cracking pressures vary from a minimum of 13.8×10^{-5} Pa to a maximum of 105×10^{-5} Pa based on experiments. Hence search space for parameters chosen in optimization is affected by types of valves available, data obtained from experimental tests and judgement. Search space for pilot ratios for POCVs and CBVs are chosen based on types of valves available in market and types of loading, while as cracking pressures and effective pressures are chosen based on experimental results and manufacturers data. The search space for values of coefficients relating flow area to effective pressure (k_1 and k_2) ; and areas of POCVs and CBVs are based on experimental results and on conservative judgement of trial and error. Values of search space chosen are shown in Table 5.1.

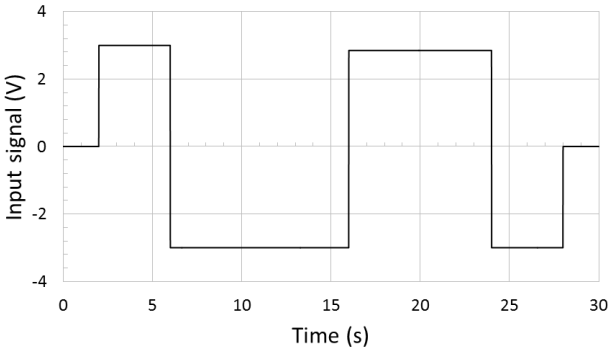
Input signal (V)
Time (s)

(a)

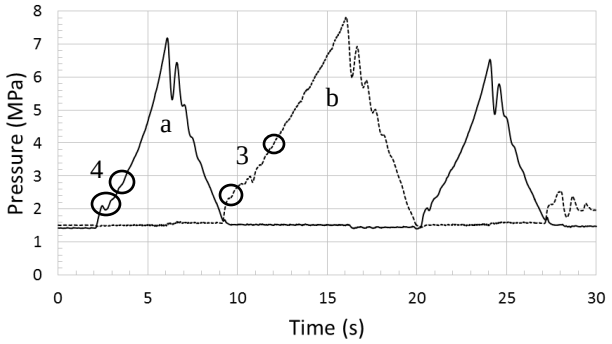
Pressure (MPa)
Time (s)
a
b
3
4

(b)

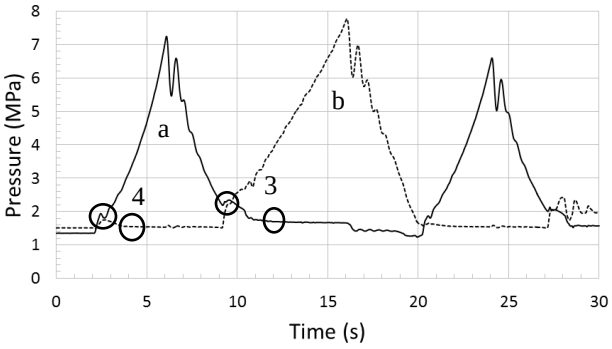
Pressure (MPa)
Time (s)
a
b
3
4

(c)

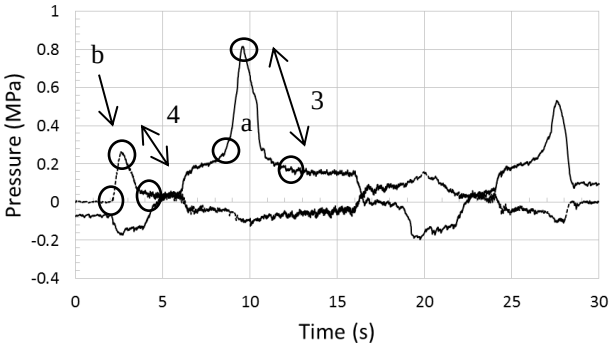

(d)

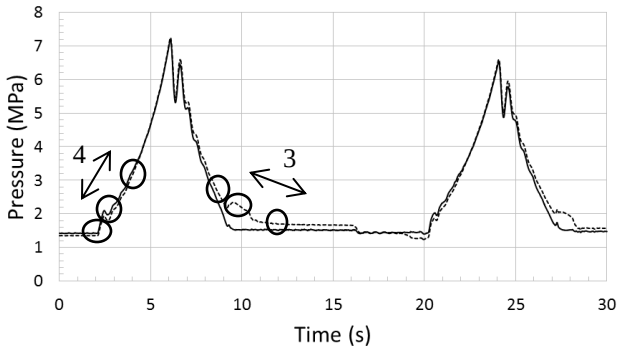

(e)

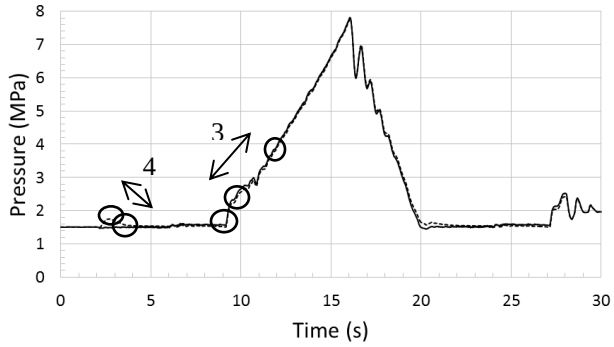

(f)

Figure 5.2 Step response of circuit at high load 368 kg (configuration 2): (a) control signal; (b) pressures at pump ports ‘a’(solid) and ‘b’ (dotted) in the configuration 1; (c) pressures at actuator ports ‘a’(solid) and ‘b’ (dotted) in the configuration 1; (d) pressure difference with time across CBV valves ‘a’ (solid) and ‘b’ side (dotted) of configuration 1; (e) pressures at pump port(solid) and actuator port(dotted) on A side of configuration 1; (f) pressures at pump port(solid) and actuator port(dotted) on B side of configuration 1.

Table 5.1. Search space chosen for two hydraulic circuits

	Parameters	Search space
	Configuration 1	
1.	K_{pilot1}	[1,5]
2.	K_{pilot2}	[1,5]
3.	p_{cr1}	$[0.3\times10^{5},7\times10^{5}]$
4.	p_{cr2}	$[0.3\times10^{5},7\times10^{5}]$
5.	p_{max1}	$[0.75\times10^{5},17.5\times10^{5}]$
6.	p_{max2}	$[0.75\times10^{5},17.5\times10^{5}]$
7.	A_{max1}	$[0.10\times10^{-4},0.44\times10^{-4}]$
8.	A_{max2}	$[0.10\times10^{-4},0.44\times10^{-4}]$
9.	k_1	$[2\times10^{-11},5\times10^{-10}]$
10.	k_2	$[2\times10^{-11},5\times10^{-10}]$
	Configuration 2	
1.	K_{pilot1}	[0.5,10]
2.	K_{pilot2}	[0.5,10]
3.	s_3	[0,5]
4.	s_4	[0,5]

5.3. Objective function and optimization algorithms:

In this research a maximum of 10 parameter optimisation is used to obtain optimal values of component parameters (optimal component sizing). Root mean square value of time derivatives of acceleration (jerk) is used as objective function. For hydraulic circuit configuration 1 we have:

$$f(j_{rms}, t)|\ (p_{cr1}, p_{max1}, K_{pilot1},\ A_{max1}, k_1, p_{cr2}, p_{max2}, K_{pilot2},\ A_{max2}, k_2) = j_{rms} \quad (5.3)$$

where j_{rms} represents root mean square value of jerk as shown:

$$j_{rms} = \left(\frac{(j_1)^2+(j_2)^2+(j_3)^2+\cdots(j_N)^2}{N} \right)^{1/2} \quad (5.4)$$

here j_1, j_2, j_3 ... j_N are the samples of first derivative of actuator acceleration. p_{cr1} *and* p_{cr2} denote cracking pressure of $POCV_A$ and $POCV_B$ respectively . p_{max1} and p_{max2} denote effective pressure when $POCV_A$ and $POCV_B$ undergo full cracking. K_{pilot1} and K_{pilot2} denote pilot ratio of $POCV_A$ and $POCV_B$. A_{max1} and A_{max2} denote maximum opening area of $POCV_A$ and $POCV_B$. k_1 and k_2 denote coefficient relating flow area to effective pressure on $POCV_A$ and $POCV_B$ respectively.

For hydraulic circuit configuration 2 we have:

$$f(j_{rms}, t)|\ (K_{pilot3}, s_3, K_{pilot4}, s_4) = j_{rms} \quad (5.5)$$

where K_{pilot3} and K_{pilot4} denotes pilot ratio of CBV_A and CBV_B respectively. s_3 and s_4 denotes number of rotations for CBV_A and CBV_B respectively. A total of 4 parameters are optimized for this configuration.

PSO (particle swarm optimization) and MNM algorithms are used for optimization. Particle swarm optimization is a stochastic algorithm which is population based. A vector, moves around the space where new parameters are tested. Number of particles tend to cluster together in optimal regions in search space chosen. First, the velocity or step size of the particle is used to define particle behaviour. This is followed by adding the velocity to its previous position [28, 29] as:

$$(v_{id})^{t+1} \leftarrow \alpha_x (v_{id})^t + W(0, \beta_x)(p_{id} - (x_{id})^t) + W(0, \beta_x)(p_{gd} - (x_{id})^t) \quad (5.6)$$

$$(x_{id})^{t+1} \leftarrow (x_{id})^t + (v_{id})^{t+1} \quad (5.7)$$

d is the dimension, where i is index of particle, x_i represents position of particle, v_{id} represents velocity of particle, p_i represents the best position found (i), g represents the index of best neighbor of i, α_x and β_x are constants, $W(0, \alpha_{id})$ is a uniform random number generator. PSO

algorithm compares the result to the best result obtained p_i and updates the vector with current position x_{id}. Each particle cycles around a region centered on a centroid of the previous bests p_i and p_g.

Modified NM algorithm is a globalised and bounded Nelder-Mead algorithm with deterministic restarts [21]. The Nelder-Mead algorithm uses *n+1* verticies x_{n1}, x_{n2}, ..., x_{nn+1} as initial simplex where 'n' denotes number of parameters to be optimized. Possible variants use reflection, expansion, contraction and shrinkage. It takes centroid of all points followed by computation of reflected point, expanded point and shrinkage. A variation of Nelder-Mead, known as Guin method helps to put bounds on optimal gain search by Nelder-Mead algorithm. A globalized Guin augmented variant of Nelder-Mead with deterministic restarts is what is known as Modified NM algorithm. First, a region of interest(*R*) is identified for optimal parameters search as [21]:

$$R = \begin{pmatrix} M_1 \\ M_2 \\ \cdot \\ . \\ M_3 \end{pmatrix} \tag{5.8}$$

where $M_1, M_2, \ldots, M_{2^n}$ represent matrices order 1× n and represent vertices of n-dimensional search space. Secondly, the number of restarts is defined. This is followed by first run, where initial simplex(S) is formed as [21]:

$$S = (X_c^T . J_{1,n+1})^T + \begin{pmatrix} 0 & 0 & 0 \ldots 0 & 0 \\ \beta_{1A} & 0 & 0 \ldots 0 & 0 \\ 0 & \beta_{2A} & 0 \ldots 0 & 0 \\ & & \vdots & \\ 0 & 0 & 0 \ldots 0 & \beta_{NA} \end{pmatrix} \tag{5.9}$$

where X_c represents the centroid of search space and J is a matrix consisting of ones with subscript showing its order where β_{iA} is given by [21]:

$$\beta_{iA} = \begin{cases} -\left(\frac{x_{imax}-x_{imin}}{\beta_B}\right) & i = 1 \\ \left(\frac{x_{imax}-x_{imin}}{\beta_B}\right) & i \in \{2, 3, 4, \dots, N\} \end{cases} \quad (5.10)$$

where x_{imax} and x_{imin} are bounds on ith parameter to be optimized and β_B denotes initial simplex size coefficient. Local minimizer X_0 found by each run is used for constructing initial simplex for succeeding runs. Local minimizer is projected onto 2^N points P within search space when centroid of search space is lying at origin and P is given by [21]:

$$P = (0.5R - 0.5(X_0^T . J_{1,2^N})^T \quad (5.11)$$

If it doesn't lie at origin, then search space is translationally moved to make centroid lie at origin, in order to avoid violation of bounds on parameter search by projected points. This results in new centroid in this case. Finally, local minimizer is projected onto 2^N points within moved search space for new P matrix of order $2^N \times$ n obtained as [21]:

$$\hat{P} = (0.5\hat{R} - 0.5(\hat{X}_0^T . J_{1,2^N})^T \quad (5.12)$$

Projected points are moved back to original search space as [21]:

$$P = \hat{P} - \left(\begin{pmatrix} d_1 \\ d_2 \\ \cdot \\ . \\ d_N \end{pmatrix} . J_{1,2^N} \right)^T \quad (5.13)$$

where d_1, d_2, …, d_N are distances between centroid and origin long respective axes of n-dimensional search space. This is followed by evaluation of objective function on all these points where one is designated as P_0 which is used for construction of initial simplex for succeeding run based on certain criteria and using linearly growing memory vector. This helps algorithm to avoid getting stuck in the local minimizer. To make initial simplex respect bounds for all succeeding runs β_{iA} is given by [21]:

$$\beta_{iA} = \begin{cases} -\left(\frac{x_{imax}-x_{imin}}{\beta_B}\right) & P_0 \text{ exceeds } X_c \text{ in } i\text{th dimension} \\ \left(\frac{x_{imax}-x_{imin}}{\beta_B}\right) & X_c \text{ equals or exceeds } P_0 \text{ in } i\text{th dimension} \end{cases} \quad (5.14)$$

where P_0 is selected as the one having minimum value of objective function amongst all projected points, which are not elements of existing memory vector. The optimization will continue until minimum found is less than or equal to desired minimum or it selects the best local minimum found so far as global minimum or in case we reach the limit of executed restarts.

5.4. Proposed Optimization Criteria

The objective is to get a smooth (jerk free) actuator motion in two hydraulic circuit configurations (1 and 2) discussed in previous sections. Optimization algorithms are tested on a special multistep polynomial input designed, based on the concept used in [15]. The proposed optimization criterion for configuration 1 is divided into few steps. First, pilot ratios or cracking pressures of POCVs are optimized (two parameter optimization). Next, the number of parameters to be optimized is increased to four. Finally, the number of parameters to be optimized is increased to ten for obtaining better performance.

Configuration 2 is tested using MNM algorithm only. First, the pilot ratios are optimized, followed by optimization of cracking pressures of CBV valves. Next, four parameter optimization is used for optimizing both pilot ratios and cracking pressures of CBV valves simultaneously. Next, experimental tests are performed to verify simulation results. Finally, one more experiment is performed using a step input to check the performance of the system for configuration 2, comparing results before and after optimization.

Before optimization, configuration 1 uses a pilot ratio of 3 for both POCVs. In case of configuration 2 before optimization, pilot ratio of 1 is used for both CBVs and cracking pressures are set by increasing number of rotations in CBV valves, where a maximum of 5 rotations can be set on each valve. CBV_A and CBV_B are set at 2 and 1.5 rotations respectively.

5.4.1 Configuration 1

Pilot ratios are optimized using both PSO and MNM [8] algorithms. To start with, two tests are performed where search space: [1-3] is chosen for optimizing pilot ratio in case of high and low loads respectively uses MNM algorithm. The values of objective functions obtained via optimization are 189.2 and 97.18, respectively. Next, two more tests are performed where same search space: [1-3] is chosen and values of objective functions obtained via optimization are 191.25 and 109, respectively. Number of iterations for first two cases using MNM algorithm are 1937 and 2510, respectively. For next two tests where PSO algorithm was used, the iterations took approximately thrice (75 minutes) as much time as taken by MNM algorithm (25 minutes). Hence, MNM algorithm proves to be faster and results of objective functions are comparable with ones obtained from PSO algorithm.

Next using MNM algorithm, two tests where search space: [1-5] is chosen for optimizing pilot ratio, in case of high and low loads respectively is analyzed. The values of objective functions obtained via optimization are 144.53 and 92.94, respectively. Hence changing the pilot ratio from search space [1-3] to [1-5] under various loading conditions, gives us smaller value of objective function, hence smoother actuator motion (performance). Hence, search space for pilot ratio is chosen as [1-5] for next tests. Next optimization of cracking pressure of POCV valves are analyzed. Two tests where search space: [0.3-7] bar is chosen for optimizing cracking pressure in case of high load and low load respectively. The values of objective functions obtained via optimization are 123.00 and 88.75, respectively. Hence values of objective function are reduced further and hence improving the system performance. Next, both pilot ratios and cracking pressures are optimised simultaniuosly, at high load, resulting in better system performance as compared to previous cases (objective function valued at 113.3). However, undesirable regions for velocity (and pressures) could not be completely removed, as some overlapping of areas of POCVs is still seen. Hence, ten parameter optimisation is used next, to completely remove overlapping of areas of POCVs. Ten

parameter optimisation includes optimization of cracking pressure, effective pressure (when valve undergoes full valve cracking), pilot ratio, maximum opening area of valve and coefficient (relating flow area to effective pressure), under various high and low loading conditions (Figure 5.7 and 5.8). The values of objective functions obtained via optimization for these two tests are 88.86 and 79.11, respectively. Hence ten parameter optimization results in smoother motion (least jerky) and removal of undesirable regions in velocity (and pressures). Furthermore, area overlapping of POCVs is not seen in these two cases. Optimized results from high load can be used for low lows in this case as well. Finally, a step input is also used to compare the performance using system parameters before and after optimization(Figure 4.10 and 4.11, results of 10 parameter optimization were used).

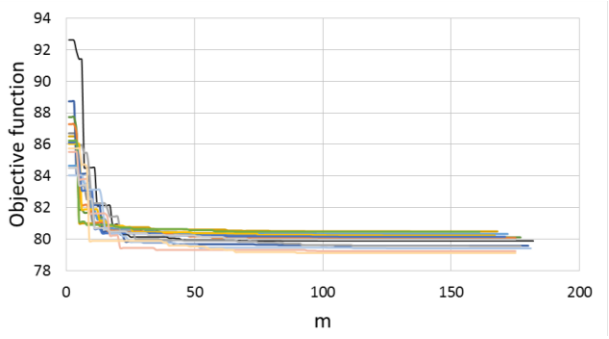

(a)

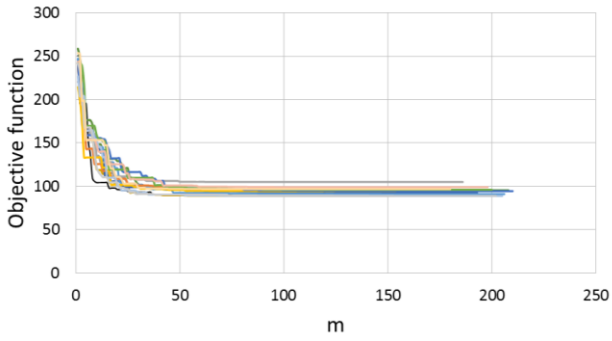

(b)

Figure 5.3 Objective function with iterations at various restarts (configuration 1): (a) Zero kg mass attached, low load (p_{cr1} = 2.38e5 *Pa*, p_{cr2} = 4.89e5 *Pa*, p_{max1} = 10.69e5 *Pa*, p_{max2} = 6.71e5 *Pa*, K_{pilot1}= 3.81, K_{pilot2} = 4.39, A_{max1} = 0.34e-4 m^2, A_{max2} = 0. 19e-4 m^2, k_1= 2.94e-10, k_2= 3.03e-10); (b) 245 kg mass attached, high load (p_{cr1} = 0.39e5 *Pa*, p_{cr2} = 0.31e5 *Pa*, p_{max1} = 9.32e5 *Pa*, p_{max2} = 5.69e5 *Pa*, K_{pilot1}= 4.6, K_{pilot2} = 4.2, A_{max1} = 0.31e-4 m^2, A_{max2} = 0. 27e-4 m^2, k_1= 3.42e-10, k_2= 3.35e-10).

Figure 5.3 shows how the objective functions converge for both low and high loads. 'm' represents the final number of iterations used to reach minimum valve in each restart for MNM algorithm. It should be noted that a total of 15 restarts were used. Optimized values of parameters are shown in Table 5.2.

Table 5.2. Optimized values of parameters (configuration 1)

	Parameters	High load	Low load
1.	K_{pilot1}	4.6	3.81
2.	K_{pilot2}	4.2	4.39
3.	p_{cr1}	0.39×10^{5}	2.38×10^{5}
4.	p_{cr2}	0.31×10^{5}	4.89×10^{5}
5.	p_{max1}	9.32×10^{5}	10.69×10^{5}
6.	p_{max2}	5.69×10^{5}	6.71×10^{5}
7.	A_{max1}	0.31×10^{-4}	0.34×10^{-4}
8.	A_{max2}	0.27×10^{-4}	0.19×10^{-4}
9.	k_1	3.42×10^{-10}	2.94×10^{-10}
10.	k_2	3.35×10^{-10}	3.03×10^{-10}

5.4.2 Configuration 2

In case of CBV (configuration 2), first pilot ratios are optimized. Two tests where search space: [0.5-10] and [0.5-3] are chosen for optimizing pilot ratios in case of high load are analyzed. The values of objective functions obtained via optimization for are 105 and 104.34, respectively. Hence smaller search space of [0.5-3] for pilot ratio is chosen for all cases in configuration 2, as the values of objective function in both these cases are approximately same, hence result in similar performance. Next, for set of tests, only cracking pressures (hence number of rotations in CBV) are optimized. This is followed by tests where cracking pressures and pilot ratios are simutaneously optimised, which result in smoother motion(least jerky), hence better performance.

To begin with, the search space was chosen from [0-5] rotations for high load, where cracking pressures (hence number of rotations in CBV) are optimized. The value of objective functions obtained via optimization for this case is 100.9, hence better system performance. But in case of low loads, same search space cannot be chosen, as zero rotations in CBV search space means least resistance to flow, as such bias force(due to difference in area across single-rod actuator and charge pressure[11]) will dominate the system. Hence a search space of [1.5-5] is chosen for low and high loads respectively. The values of objective functions obtained via optimization are 107 and 106.68, respectively. The optimal number of rotations [CBV_A CBV_B] obtained for cases are [1.5 1.75] and [2.01 1.5]. Hence for high load, optimized results prove that the CBV design used before optimization i.e. [2 1.5] is already an optimal setting at high loads. Note that this design can be used at both high and low loads.

Next, the optimal CBV valve design obtained is [1.5 1.75] which means CBV_B is set at higher cracking than CBV_A. This can be attributed to the existence of bias force (due to charge pressure dominance and difference in area across single-rod actuator) and

dominating friction at low loads, resulting in an increase in optimized cracking (or number of rotations of CBV) CBV_B value . This increase in cracking pressure of CBV_B valve at low load was confirmed by one more test, with search space [1.75 5] where optimal values of [1.75 2] are obtained after optimization.

But if this lower cracking in search space is increased beyond 1.75 rotations at low load, then optimized design again results in CBV_A being set higher than CBV_B (which is similar to CBV design as in high load). This implies that charge pressure dominates at low loads, when CBVs are set below 1.75 rotations (or below this threshold cracking pressure).

Lastly, two tests, where cracking pressures and pilot ratios are simutaneously optimised for high and low loads is performed. Values of objective functions obtained are 100.1 and 93.49, respectively. Hence resulting in improved performance when compared to previous cases discussed for configuration 2.

For experimental verification of results, some optimized configurations are tested using standard multipolynomial input and step inputs, where results before (parametric values:[2 1.5] rotations and pilot ratio [1 1]) and after optimization (optimized parameters from different cases) are compared.

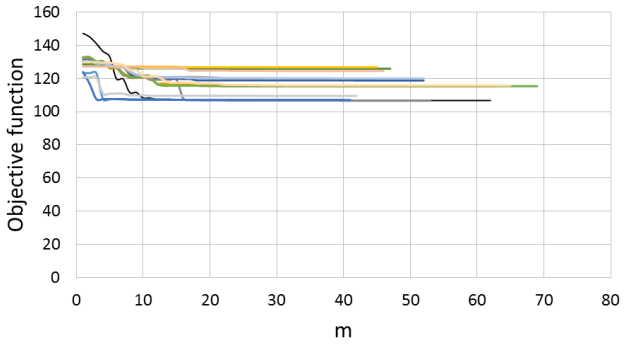

(a)

Figure 5.4 Objective function with iterations at various restarts (configuration 2) for optimized values [2.01, 1.53].

Figure 5.4 shows how the objective function converges. 'm' represents the final number of iterations used to reach minimum valve in each restart for MNM algorithm. A total of 15 restarts were used as in case of configuration 1. Optimized values of parameters are shown in Table 5.3.

Table 5.3. Optimized values of parameters (configuration 2)

	Parameters	Optimal values
1.	K_{pilot1}	1
2.	K_{pilot2}	1
3.	s_3	2.01
4.	s_4	1.53

5.5. Results

Simulation and experimental tests were performed with special multistep polynomial [21] and step inputs under variable loading conditions. Results before and after optimizations of parameters are shown and compared. First, results for configuration 1 are discussed, followed by results of configuration 2.

5.5.1 Configuration 1

For configuration 1, results before and after optimization using high load and multistep polynomial input are shown below:

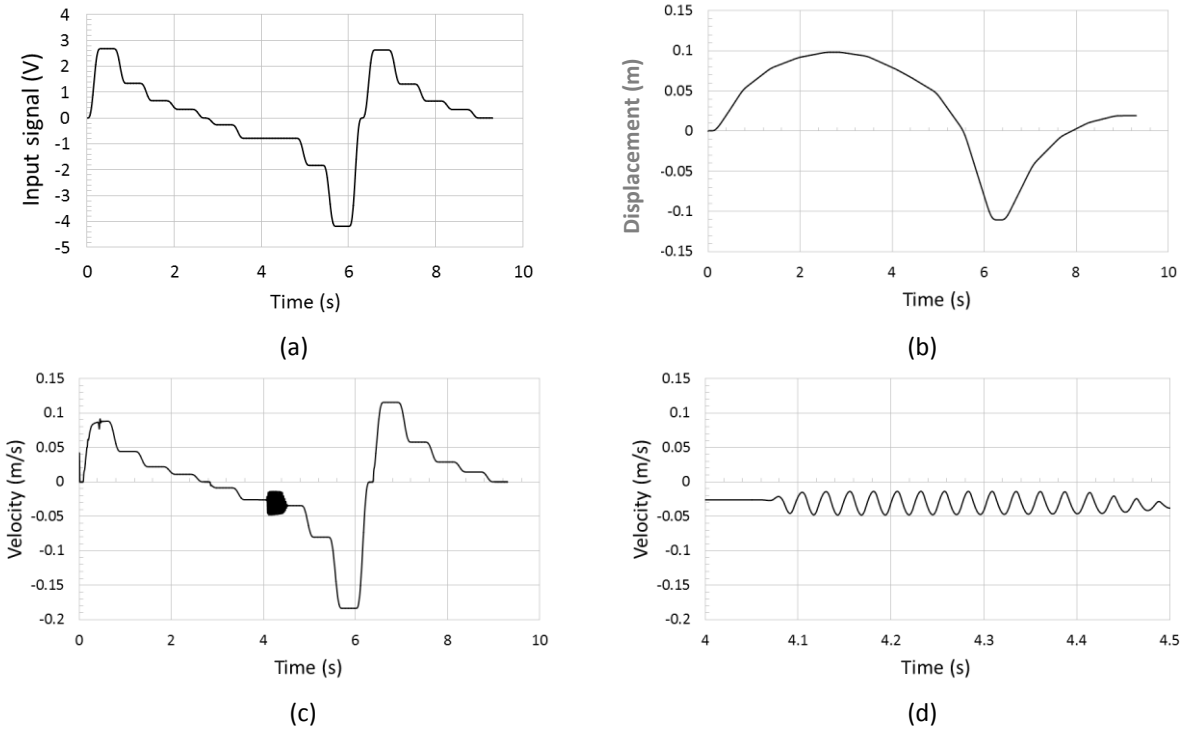

Figure 5.5 Response of multistep polynomial input (configuration 1) before optimization , mass 245 kg attached (pilot ratio of 3 for both sides): (a) control signal (V); (b) actuator displacement (m); (c) actuator velocity; (d) zoomed in a region of actuator velocity.

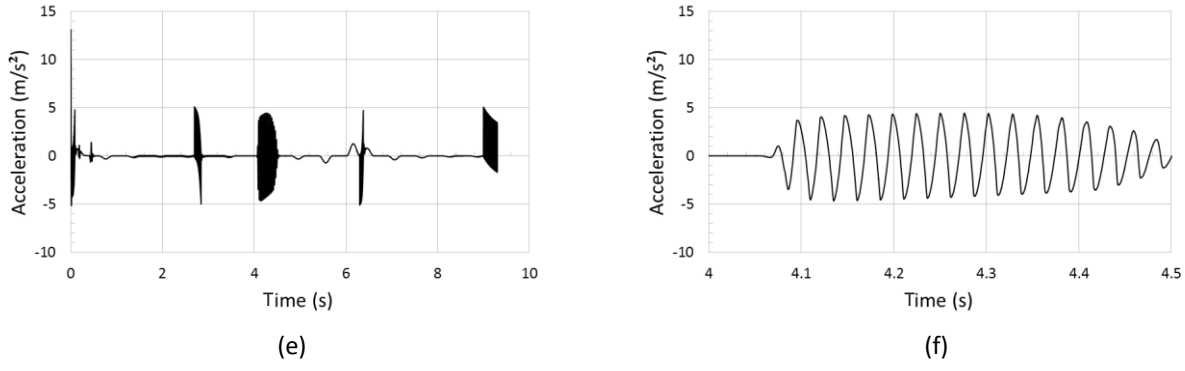

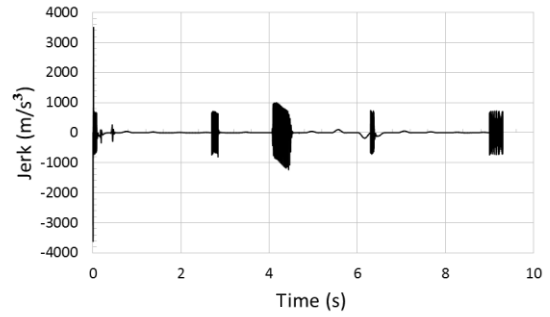

(g)

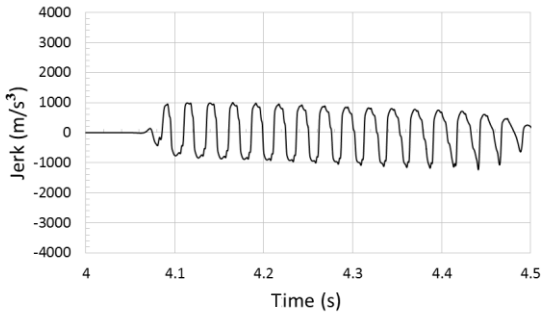

(h)

Figure 5.5(cont.): (e) Actuator acceleration; (f) zoomed in a region of actuator acceleration; (g) actuator jerk; (h) zoomed in a region of actuator jerk.

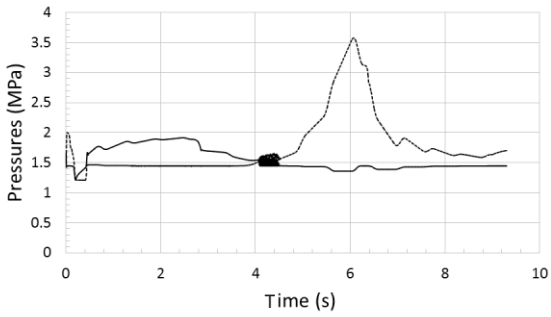

(i)

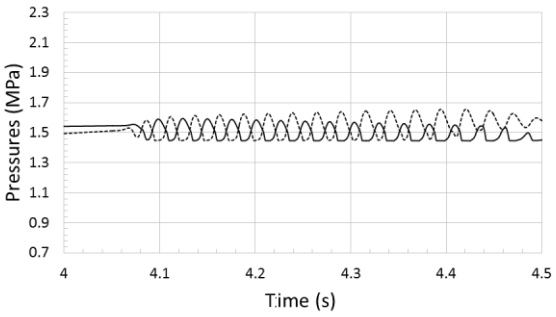

(j)

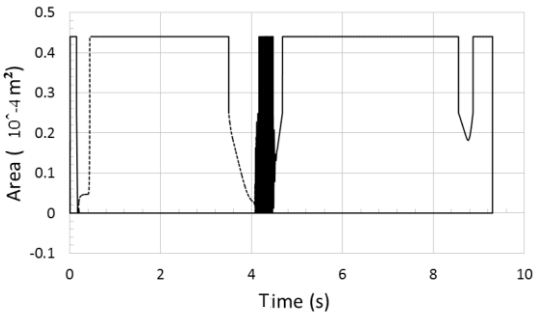

(k)

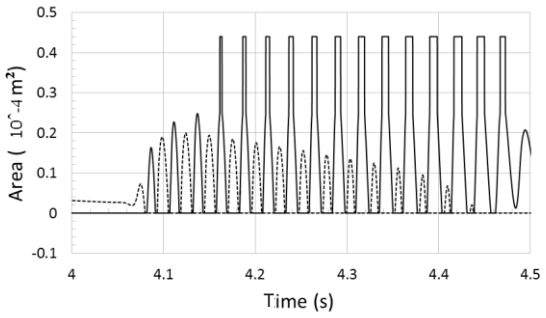

(l)

Figure 5.5(cont.): (i) Pump pressures for side ‘a’(solid) and side ‘b’ (dotted); (j) zoomed in a region of pump pressures; (k) areas of POCV side ‘a’(solid) and side ‘b’ (dotted); (l) zoomed in a region of Areas of POCV.

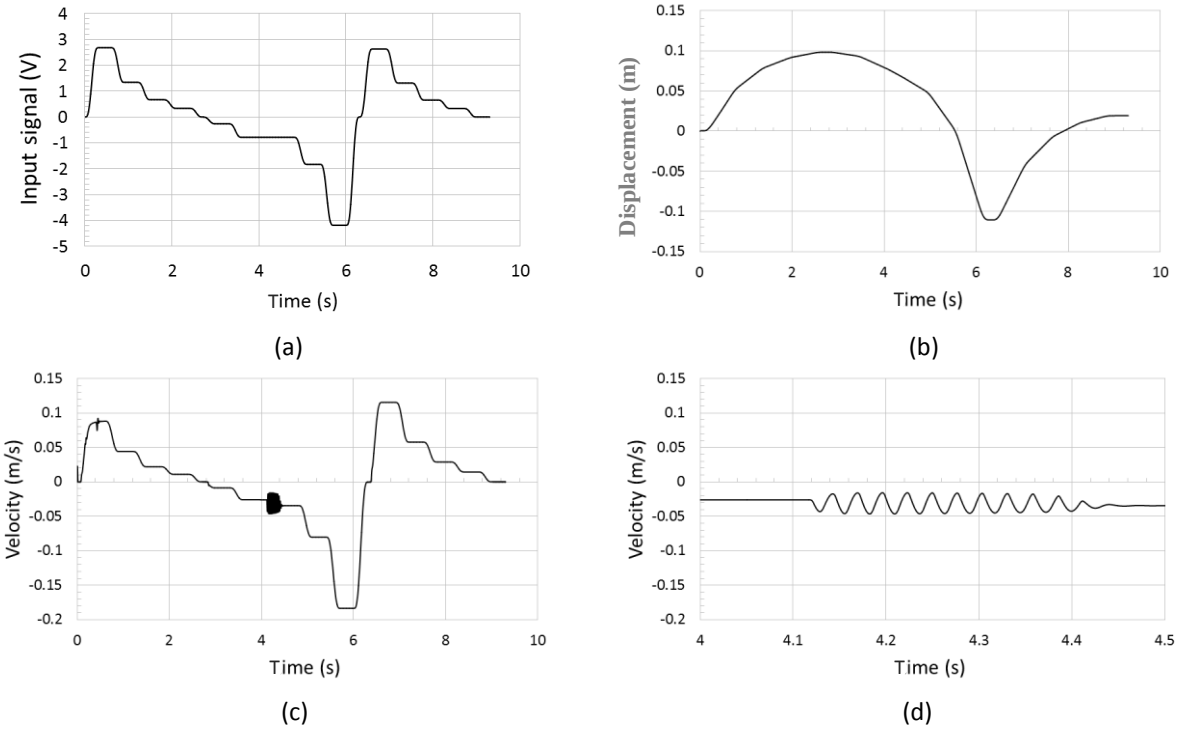

Figure 5.6 Response of multistep polynomial input (configuration 1) after optimization , mass 245 kg attached (pilot ratio 4.99 and 3.65): (a) control signal (V); (b) actuator displacement (m); (c) actuator velocity; (d) zoomed in a region of actuator velocity.

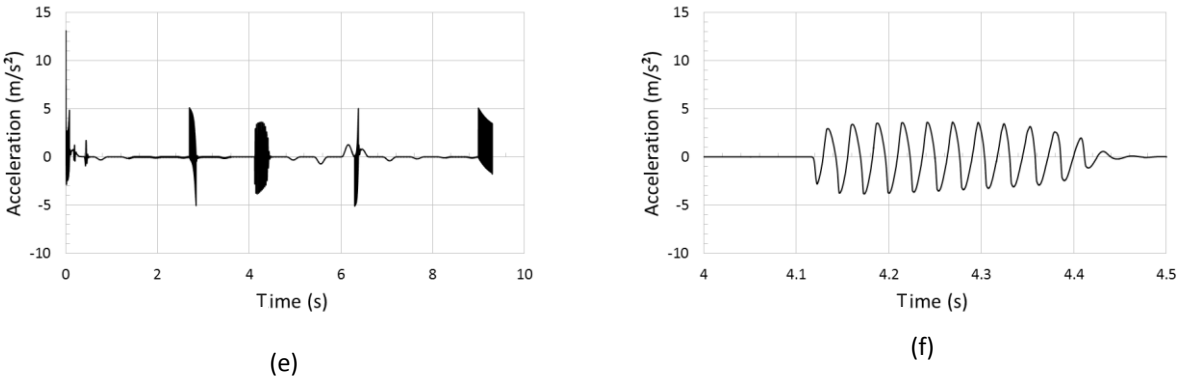

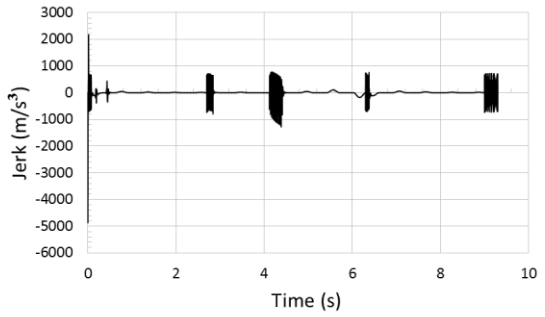

(g)

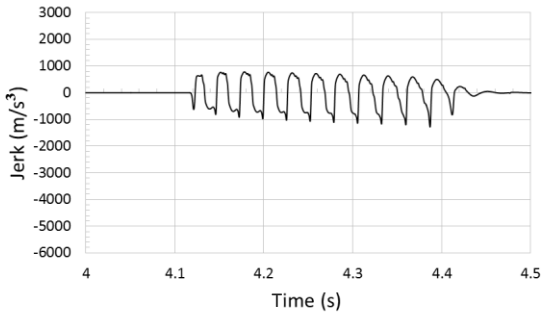

(h)

Figure 5.6(cont.): (e) Actuator acceleration; (f) zoomed in a region of actuator acceleration; (g) actuator jerk; (h) zoomed in a region of actuator jerk.

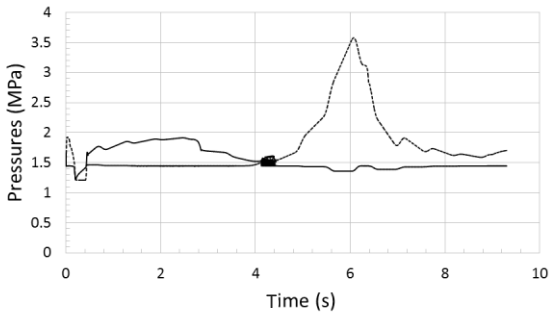

(i)

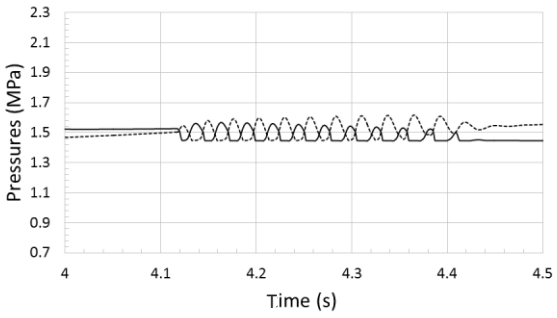

(j)

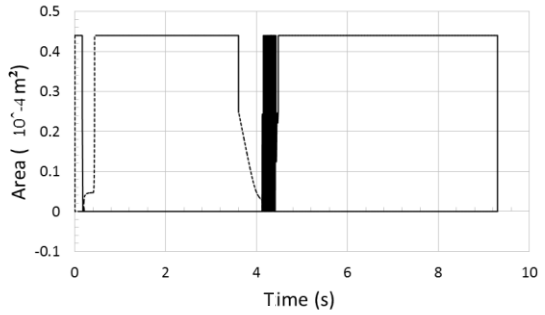

(k)

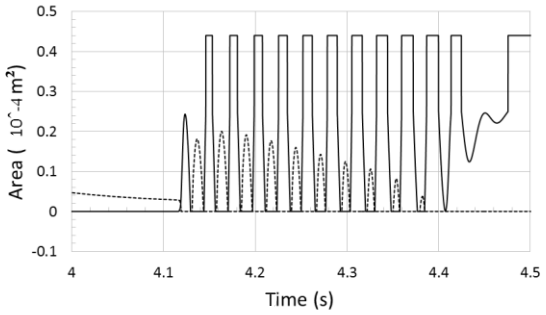

(l)

Figure 5.6.(cont.)**:** (i) Pump pressures for side 'a'(solid) and side 'b' (dotted); (j) zoomed in a region of pump pressures; (k) areas of POCV side 'a'(solid) and side 'b' (dotted); (l) zoomed in a region of areas of POCV.

After comparing results before and after optimization for high loads (Figures 5.5d and 5.6d), it is seen that the velocity is improved after using the optimized parameters i.e. the number of oscillations decrease from 17 to 10. The pressure vibrations are reduced significantly, which reduces the area overlapping of two POCV valves, resulting in lower value of objective function, hence better performance.

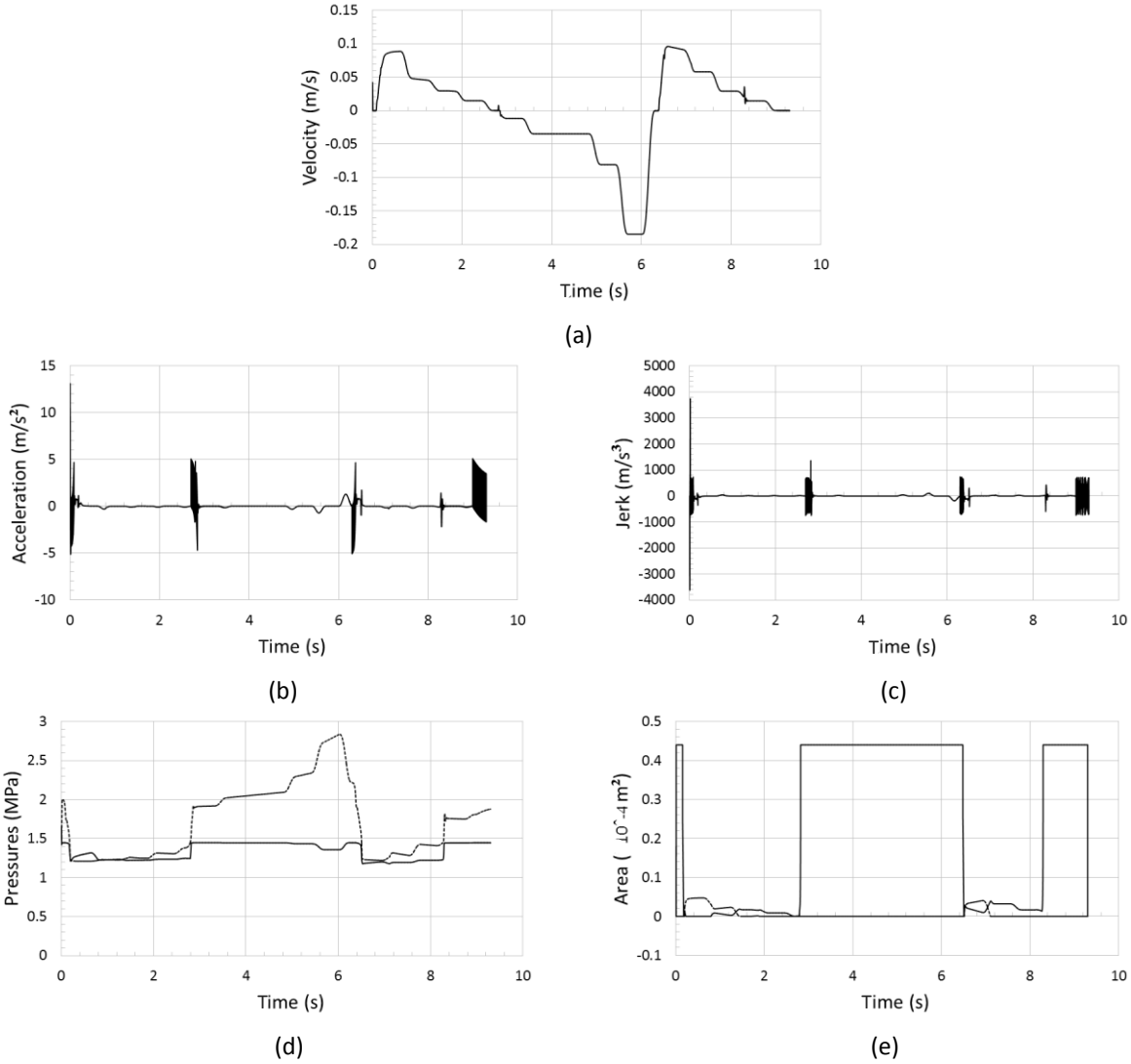

Figure 5.7 Response of multistep polynomial input (configuration 1) before optimization , mass 41 kg (pilot ratio of 3 for both sides): (a) actuator velocity; (b) actuator acceleration; (c) actuator jerk; (d) pump pressures for side 'a'(solid) and side 'b' (dotted); (e) areas of POCV side 'a'(solid) and side 'b' (dotted).

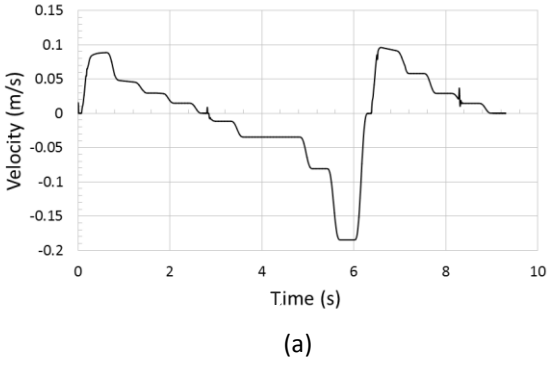

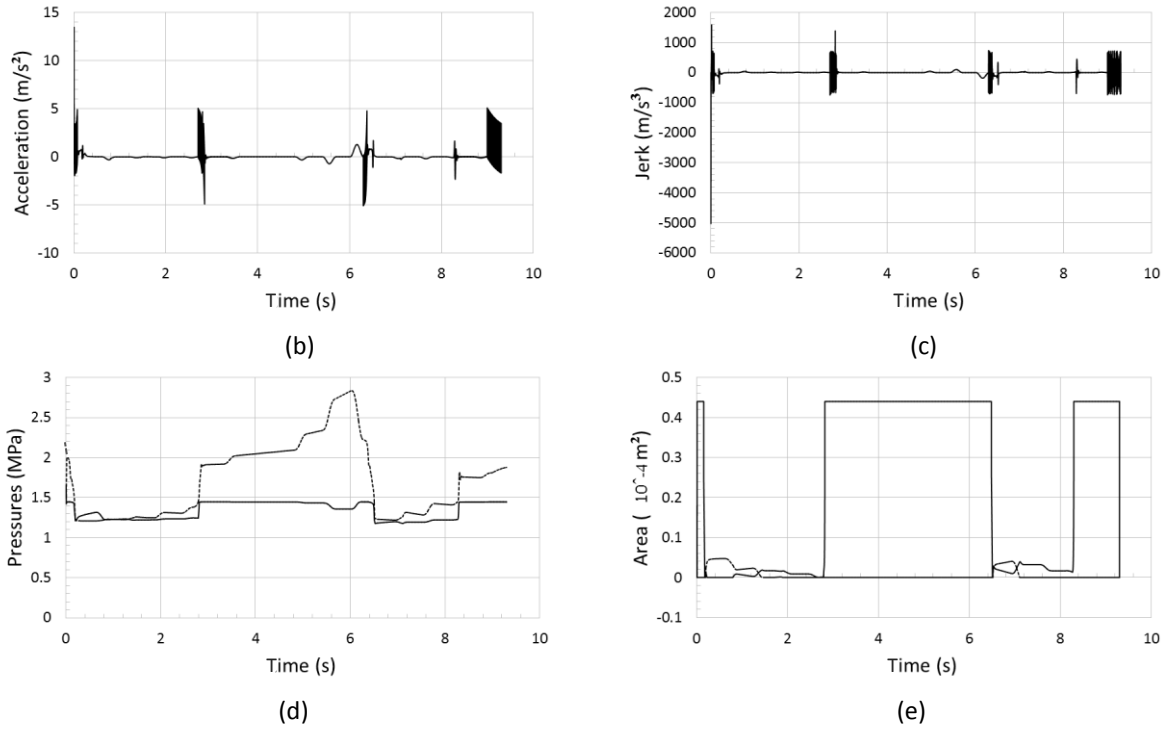

Figure 5.8**:** Response of multistep polynomial input (configuration 1) after optimization , mass 41 kg attached (pilot ratio 3.42 and 1.52): (a) actuator velocity; (b) actuator acceleration; (c) actuator jerk; (d) pump pressures for side 'a' (solid) and side 'b' (dotted); (e) areas of POCV side 'a'(solid) and side 'b' (dotted) .

Comparing the results before and after optimization at low load (Figures 5.7a and 5.8a), we see that there is slight improvement in performance after optimal values of parameters are used under low load.

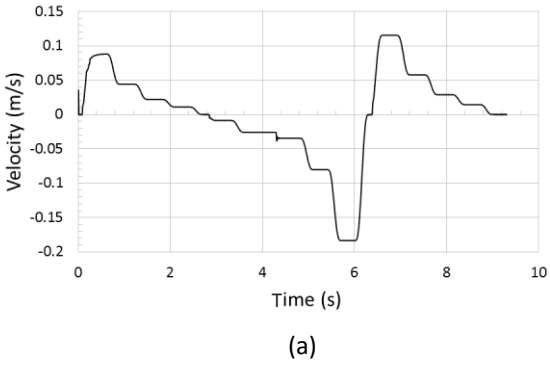

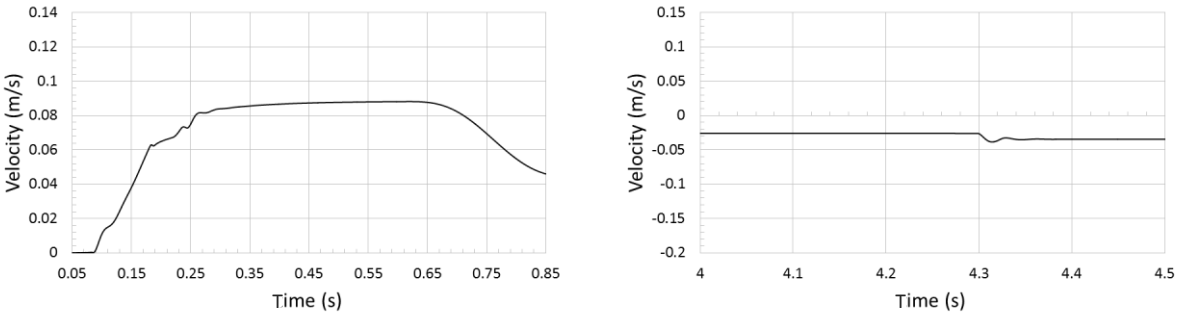

Figure 5.9**:** Response of multistep polynomial input (configuration 1) after optimization , mass 245 kg attached (p_{cr1} = 0.39e5 Pa, p_{cr2} = 0.31e5 Pa, p_{max1} = 9.32e5 Pa, p_{max2} = 5.69e5 Pa, K_{pilot1}= 4.6, K_{pilot2} = 4.2, A_{max1} = 0.31e-4 m^2, A_{max2} = 0. 27e-4 m^2, k_1= 3.42e-10, k_2= 3.35e-10): (a) actuator velocity; (b) zoomed in a region of actuator velocity; (c) zoomed in a region of actuator velocity.

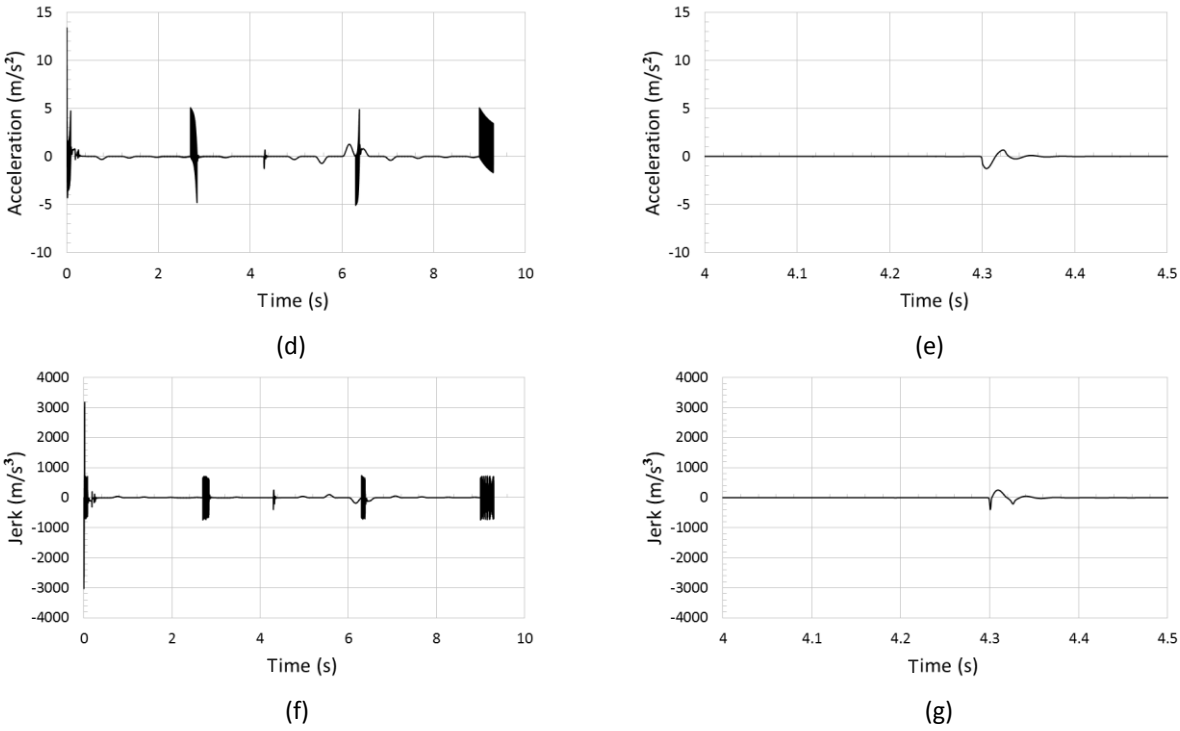

Figure 5.9(cont.) (d) Actuator acceleration; (e) zoomed in a region of actuator acceleration; (f) actuator jerk; (g) zoomed in a region of actuator jerk.

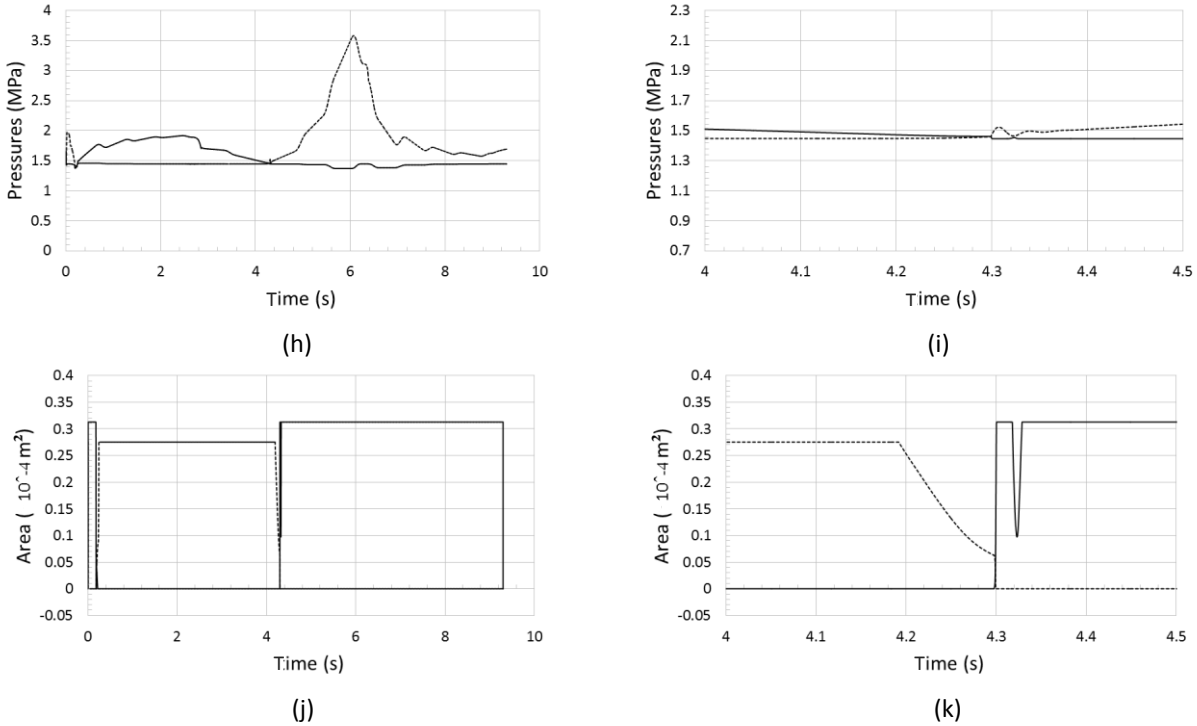

Figure 5.9(cont.) (h) Pump pressures for side ‘a’(solid) and side ‘b’ (dotted); (i) zoomed in a region of pump pressures; (j) areas of POCV side ‘a’(solid) and side ‘b’ (dotted); (k) zoomed in a region of Areas of POCV.

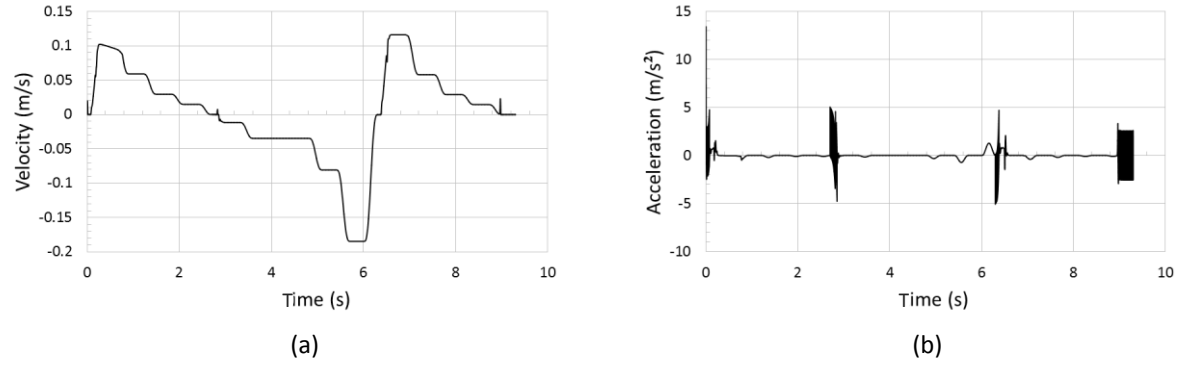

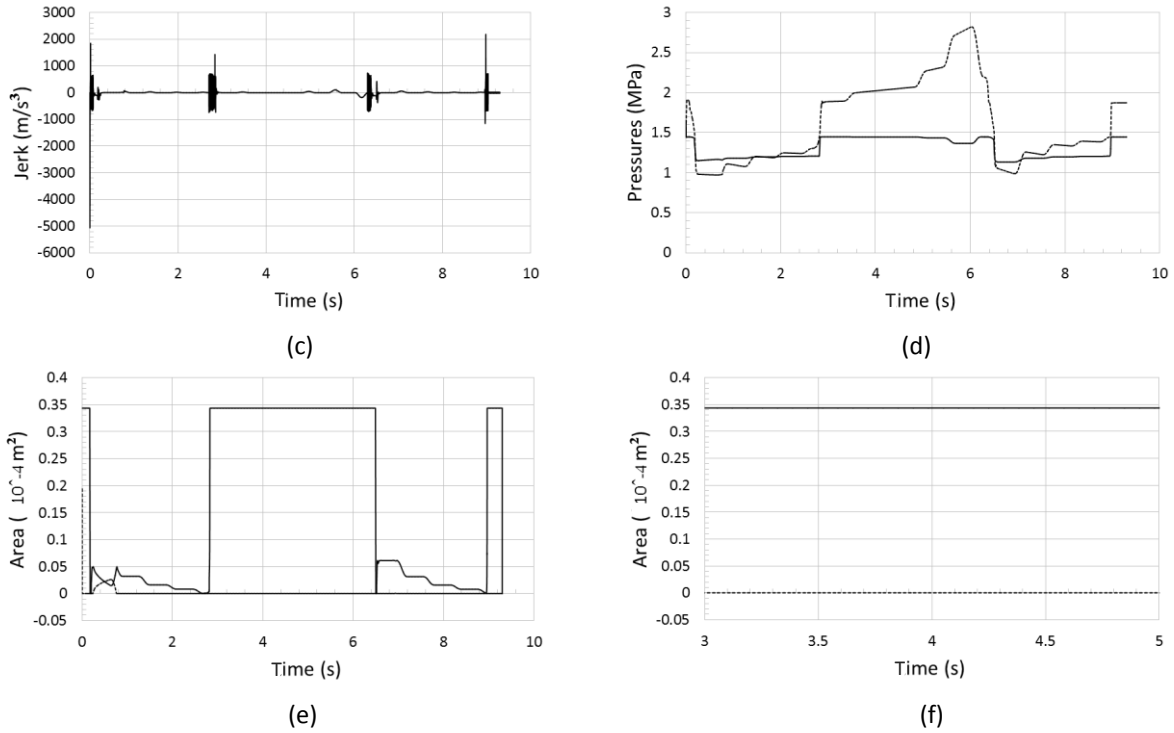

Figure 5.10**:** Response of multistep polynomial input (configuration 1) after optimization , mass 41 kg attached (p_{cr1} = 2.38e5 *Pa*, p_{cr2} = 4.89e5 *Pa*, p_{max1} = 10.69e5 *Pa*, p_{max2} = 6.71e5 *Pa*, K_{pilot1}= 3.81, K_{pilot2} = 4.39, A_{max1} = 0.34e-4 m^2, A_{max2} = 0. 19e-4 m^2, k_1= 2.94e-10, k_2= 3.03e-10): (a) actuator velocity; (b) actuator acceleration; (c) actuator jerk; (d) pump pressures for side 'a'(solid) and side 'b' (dotted); (e) areas of POCV side 'a'(solid) and side 'b' (dotted); (f) zoomed in a region of Areas of POCV.

In Figure 5.9a, 5.9i and 5.9k, for high load, no undesirable regions of pressures or area overlapping was seen and hence most improved performance when compared with other results at high loads (5.5c, 5.5j and 5.5l). Value of objective function obtained in this case is 88.86. Similarly, the performance in Figure 5.10 is also improved having least value of objective function (79.1179).

After using a multistep polynomial input, a step input is used to test the performance before and after optimization (high load optimized results will be used for comparison) as follows:

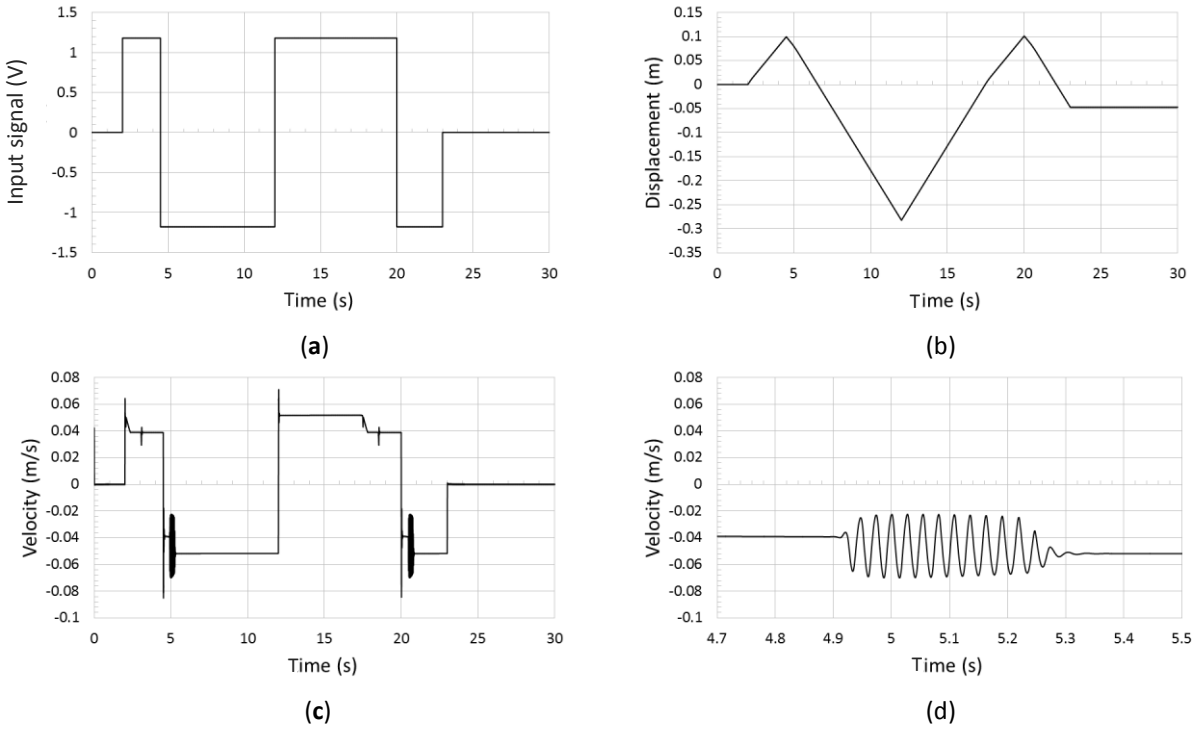

Figure 5.11 Response of alternating step input (configuration 1) before optimization, mass 245 kg (pilot ratio of 3 for both sides): (a) control signal (V); (b) actuator displacement(m); (c) actuator velocity; (d) zoomed in a region of actuator velocity.

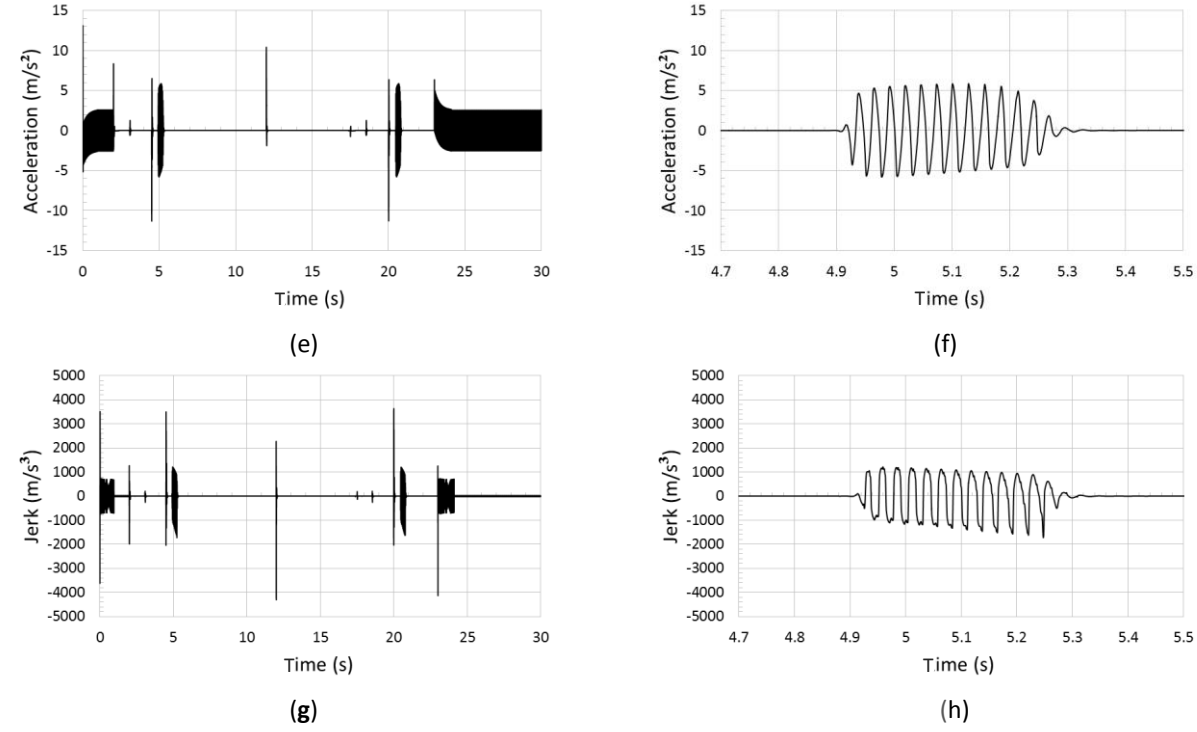

Figure 5.11(cont.): (e) Actuator acceleration; (f) zoomed in a region of actuator acceleration; (g) actuator jerk; (h) zoomed in a region of actuator jerk.

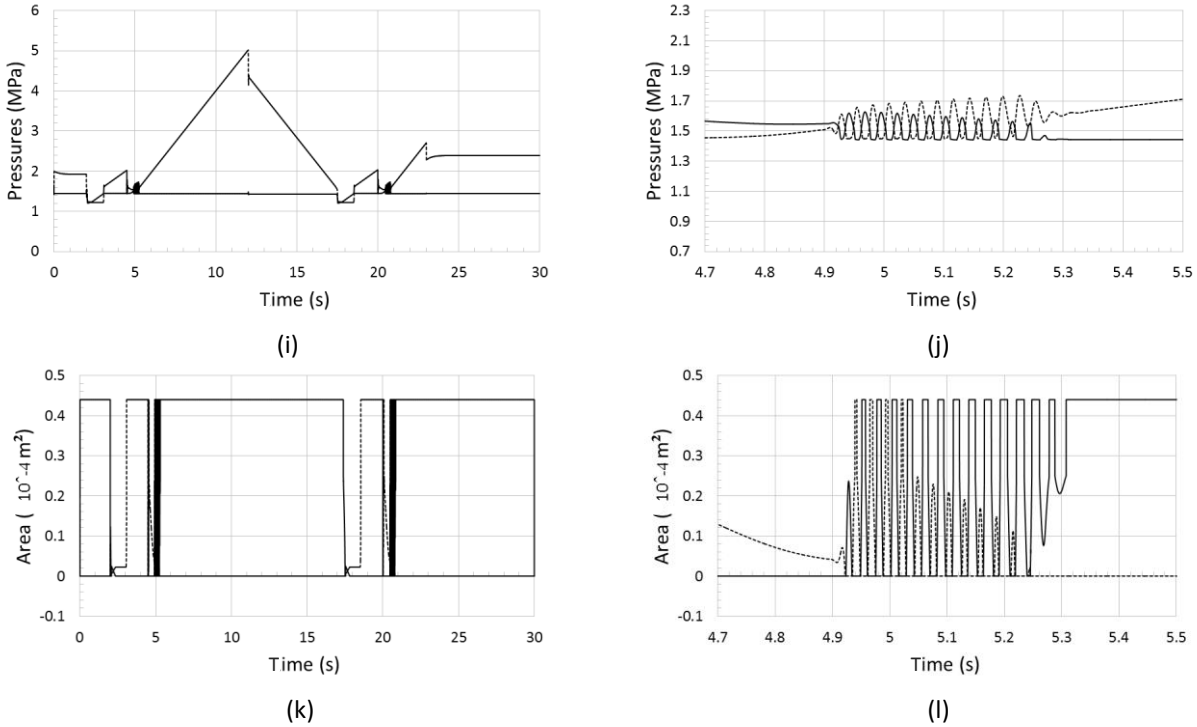

Figure 5.11(cont.): (i) Pump pressures for side 'a'(solid) and side 'b' (dotted); (j) zoomed in a region of pump pressures; (k) areas of POCV side 'a'(solid) and side 'b' (dotted); (l) zoomed in a region of Areas of POCV.

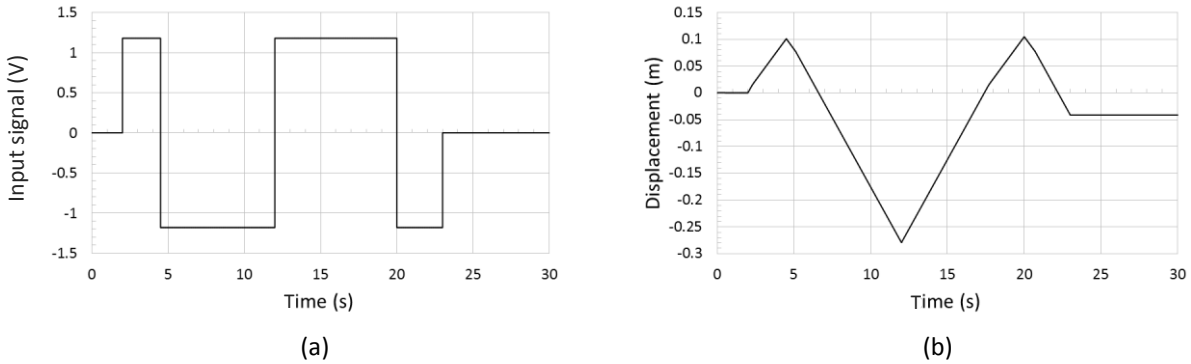

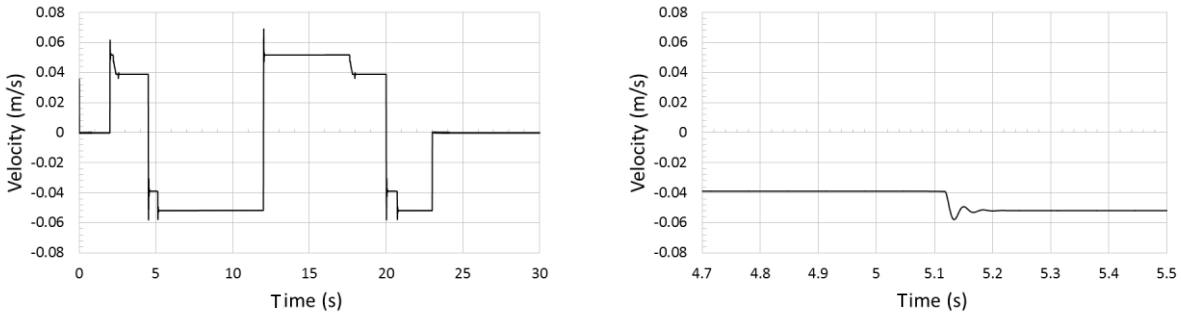

Figure 5.12 Response of alternating step input (configuration 1) after using optimized parameters, mass 245 kg attached (p_{cr1} = 0.39e5 *Pa*, p_{cr2} = 0.31e5 *Pa*, p_{max1} = 9.32e5 *Pa*, p_{max2} = 5.69e5 *Pa*, K_{pilot1}= 4.6, K_{pilot2} = 4.2, A_{max1} = 0.31e-4 m^2, A_{max2} = 0. 27e-4 m^2, k_1= 3.42e-10, k_2= 3.35e-10): (a) control signal (V); (b)actuator displacement (m) ; (c) actuator velocity; (d) zoomed in a region of actuator velocity.

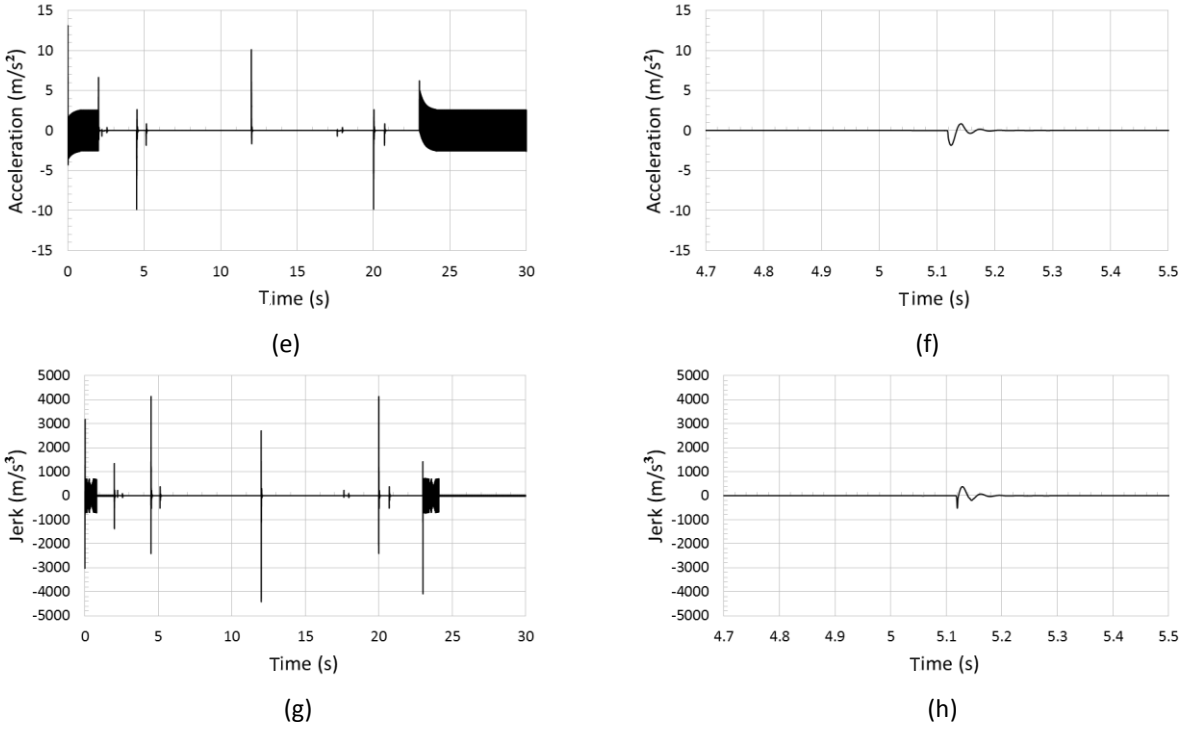

Figure 5.12(cont): (e) Actuator acceleration; (f) zoomed in a region of actuator acceleration; (g) actuator jerk; (h) zoomed in a region of actuator jerk.

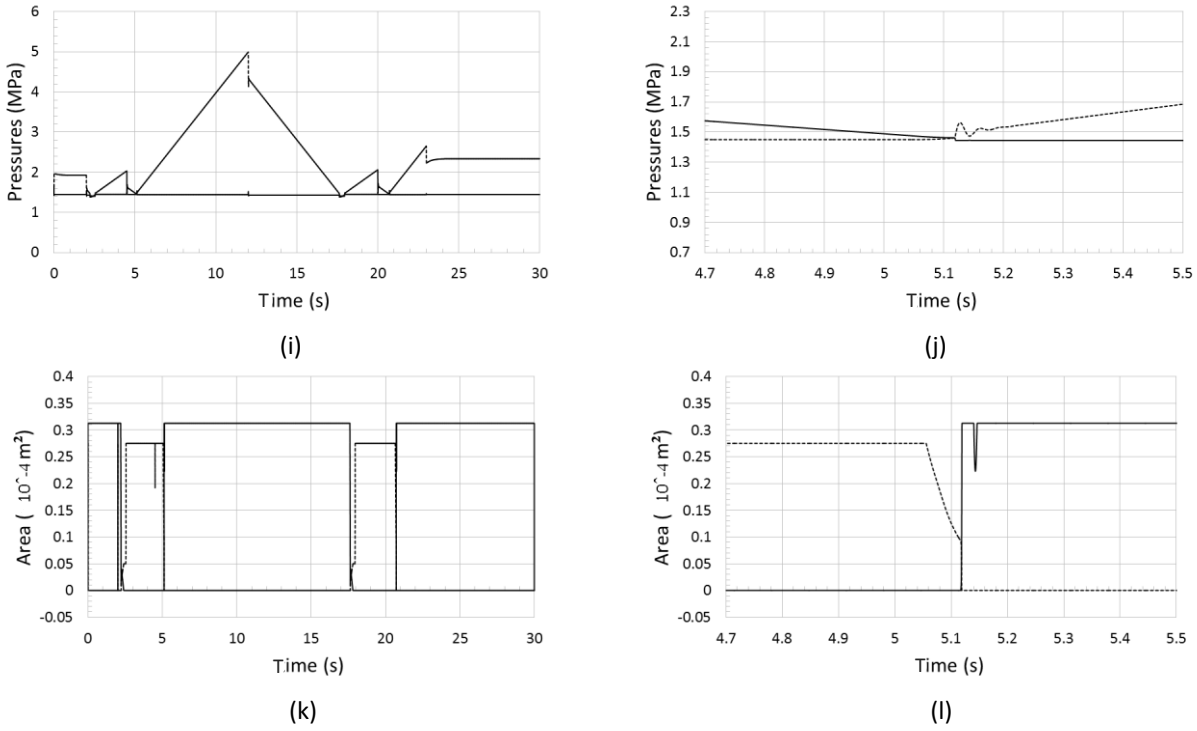

Figure 5.12(cotd): (i) Pump pressures for side 'a'(solid) and side 'b' (dotted); (j) zoomed in a region of pump pressures; (k) areas of POCV side 'a'(solid) and side 'b' (dotted); (l) zoomed in a region of Areas of POCV.

In Figures 5.11 and 5.12 with a step input at high load, the optimized results are much better as compared to results without optimization. In optimized configuration, pressure vibrations are eliminated; area overlapping removed, and better performance with least jerk as compared to results before optimization.

5.5.2 Configuration 2:

For configuration 2, using multistep polynomial input, results before and after optimization are shown, for high load, as follows:

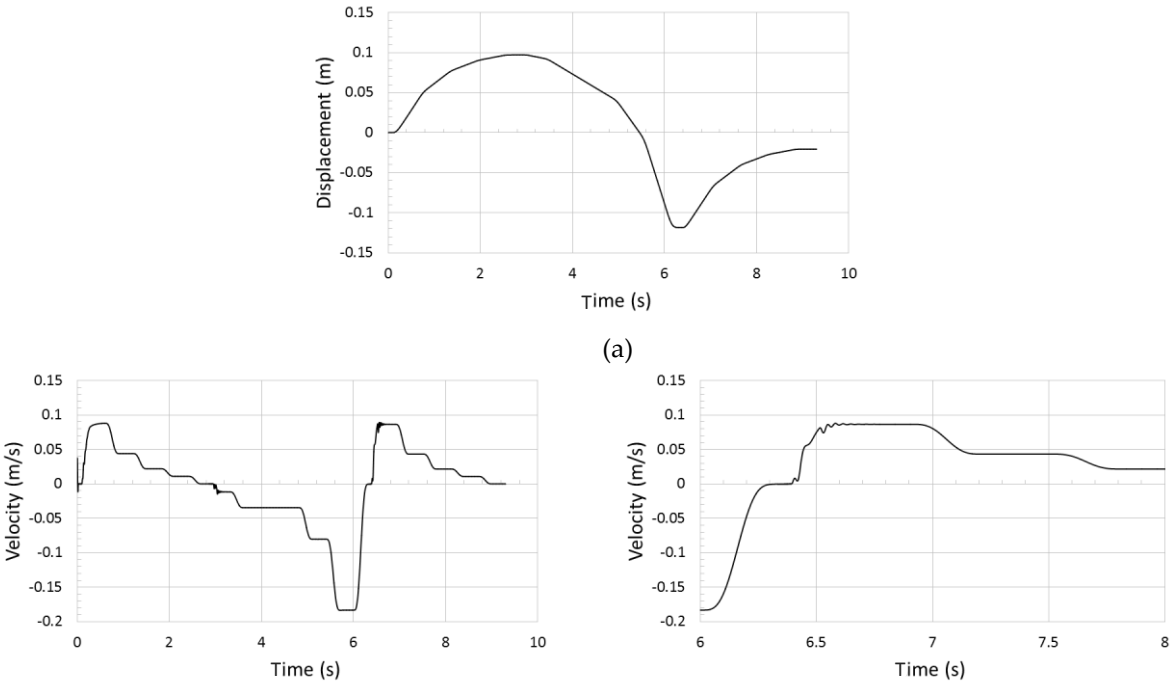

Figure 5.13 Response of multistep polynomial input (configuration 2) before optimization, mass 245 kg attached: (a) actuator displacement (m); (b) actuator velocity; (c) zoomed in a region of actuator velocity.

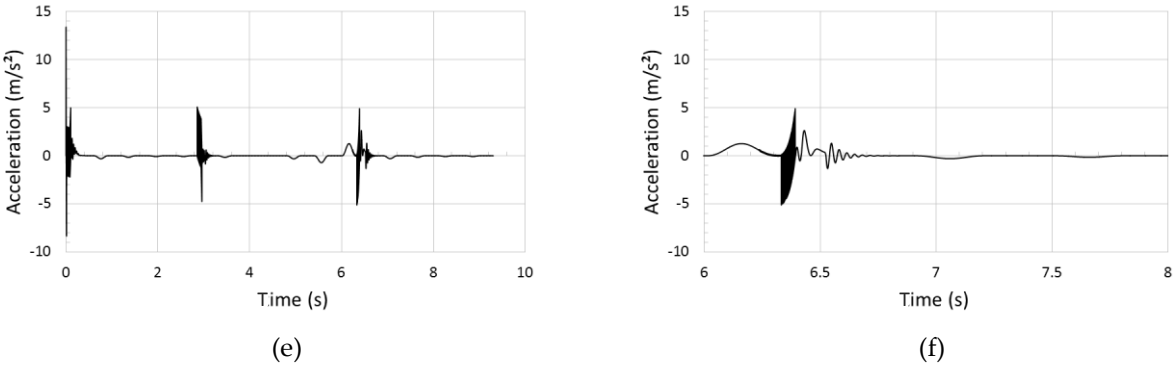

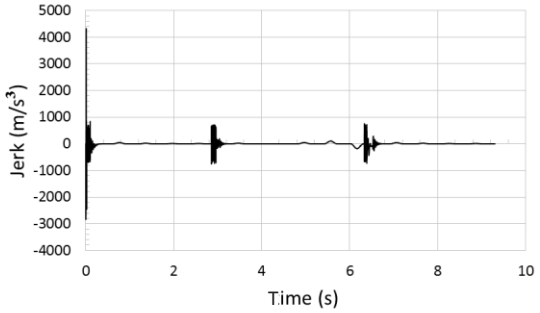

(g)

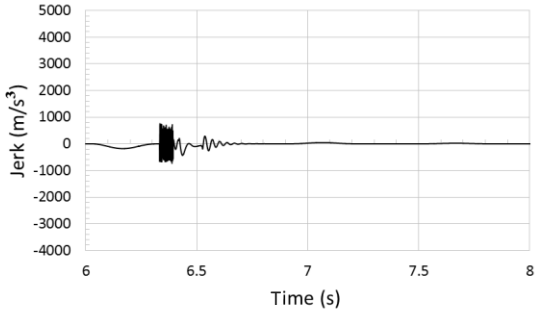

(h)

Figure 5.13(cont.): (e) Actuator acceleration; (f) zoomed in a region of actuator acceleration; (g) actuator jerk; (h) zoomed in a region of actuator jerk .

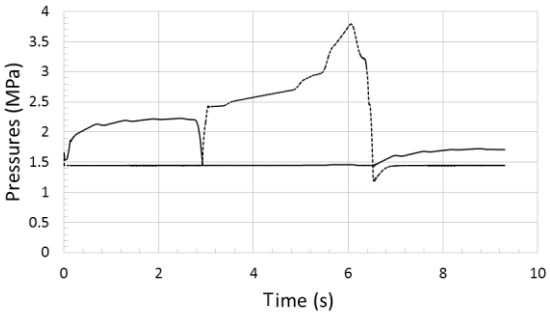

(i)

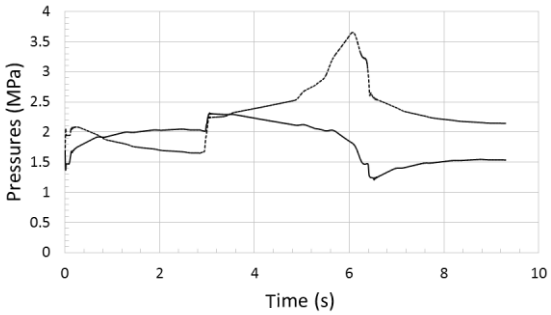

(j)

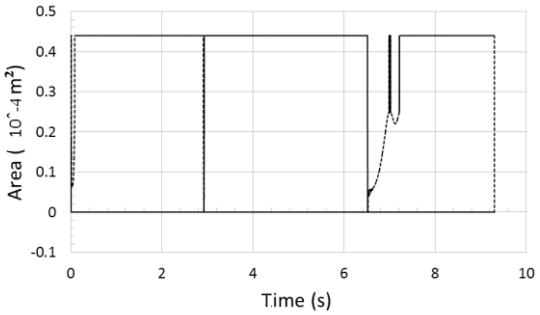

(k)

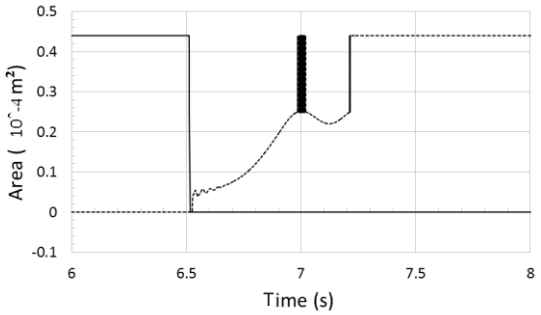

(l)

Figure 5.13(cont.) : (i) Pump pressures for side ‘a’(solid) and side ‘b’ (dotted); (j) zoomed in a region of pump pressures; (k) areas of POCV for side ‘a’(solid) and side ‘b’ (dotted); (l) zoomed in a region of Areas of POCV.

In Figure 5.13, at high load, performance of system is affected due to variations in velocity

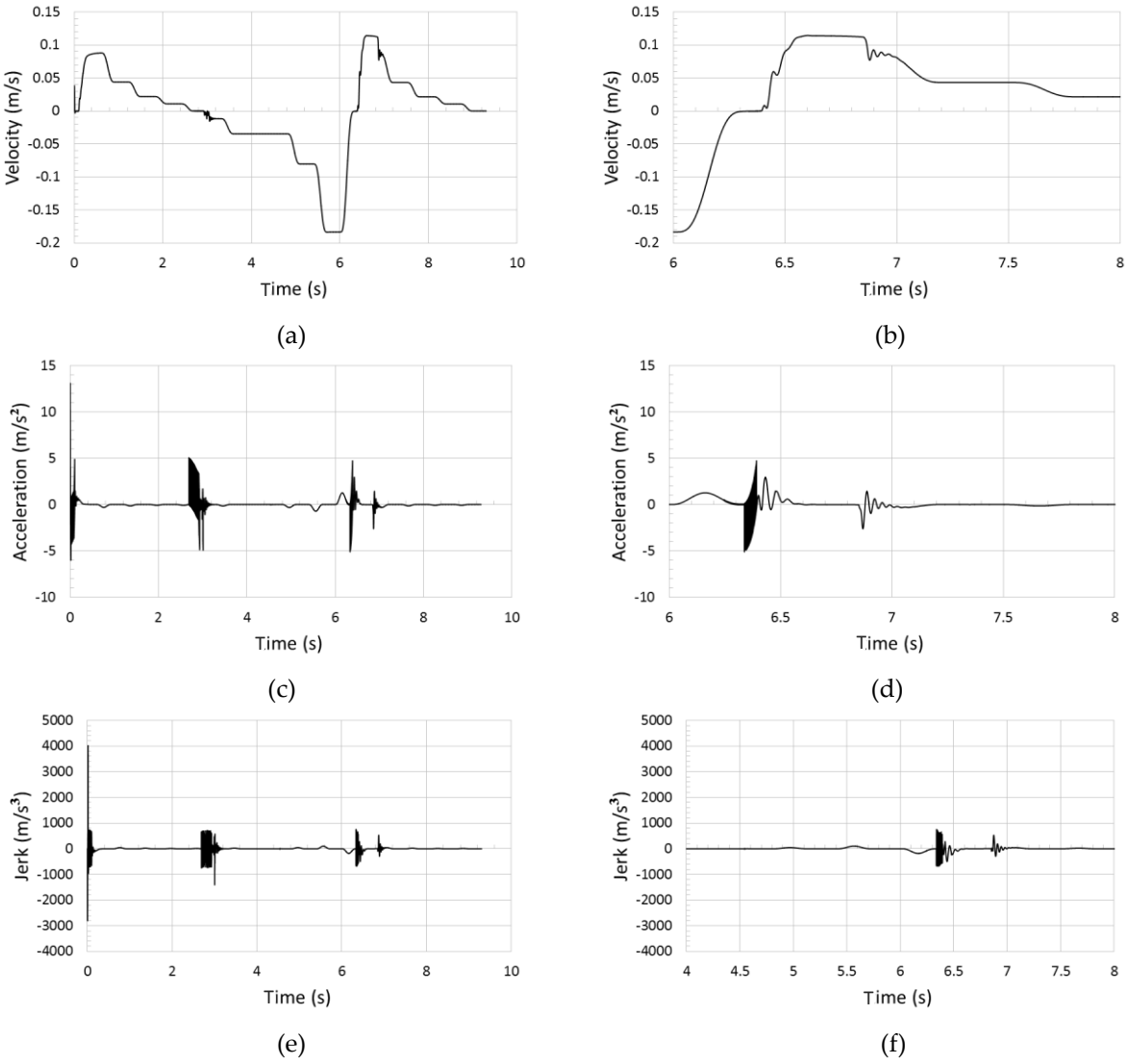

Figure 5.14**:** Response of multistep polynomial input (configuration 2) after using optimized parameters, mass 245 kg attached (s_3 = 2.07, $s_4 = 0.99$, K_{pilot3} = 1.04, K_{pilot4} = 0.80): (a) actuator velocity; (b) zoomed in a region of actuator velocity; (c) actuator acceleration; (d) zoomed in a region of actuator acceleration; (e) actuator jerk; (f) zoomed in a region of actuator jerk.

Figure 5.14 shows that performance is better (as value of objective function is better), at high load. For low loads, performance of configuration 2 before and after optimization is shown as:

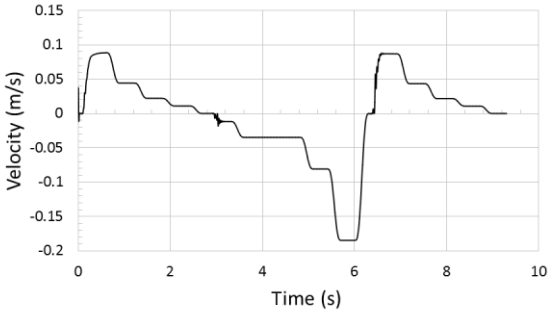

(a)

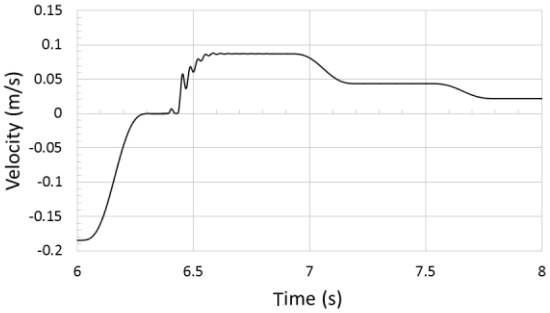

(b)

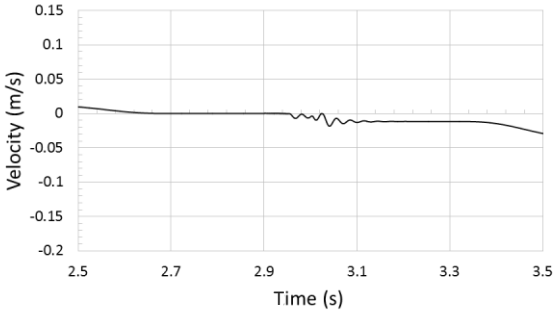

(c)

Figure 5.15 Response of multistep polynomial input (configuration 2) before optimization, mass 41 kg attached: (a) actuator velocity; (b) zoomed in a region of actuator velocity; (c) zoomed in a region of actuator velocity.

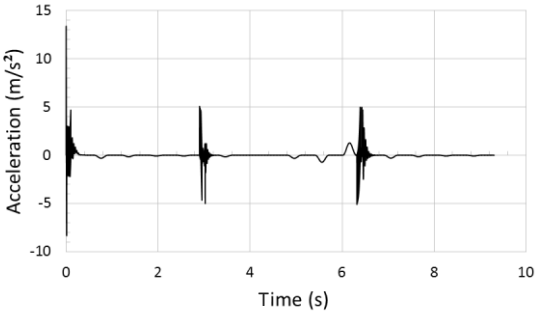

(d)

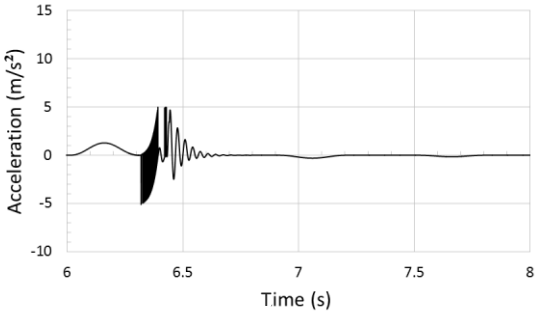

(e)

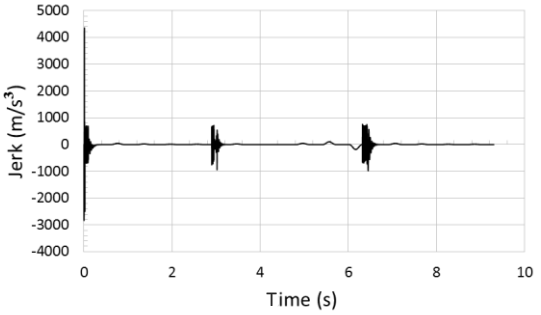

(f)

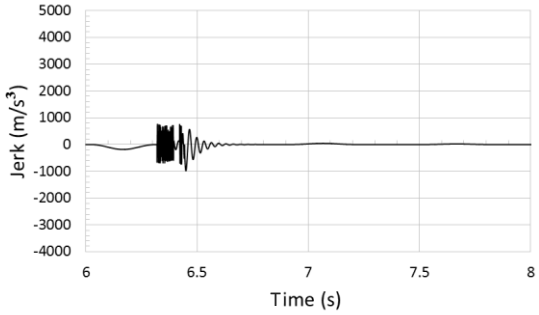

(g)

Figure 5.15(cont.): (d) Actuator acceleration; (e) zoomed in a region of actuator acceleration; (f) actuator jerk; (g) zoomed in a region of actuator jerk.

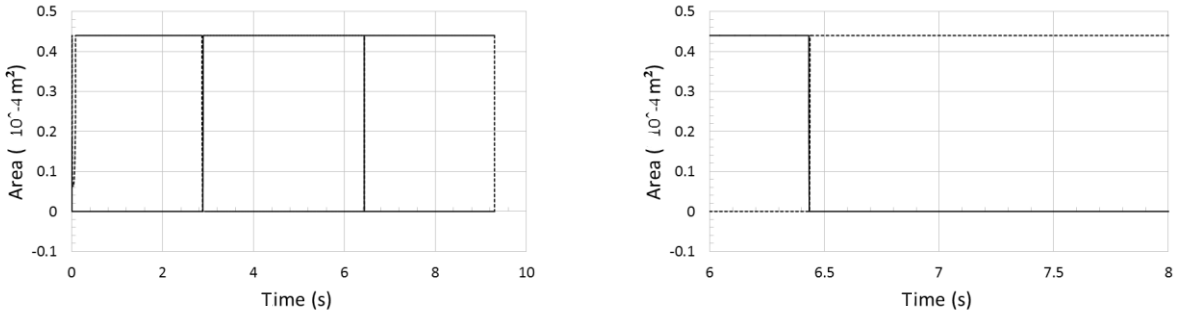

(h)

(i)

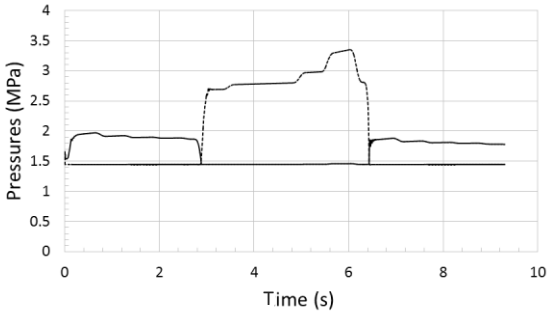

(j)

Figure 5.15(cont.): (h) Areas of POCV side 'a'(solid) and side 'b' (dotted); (i) zoomed in a region of Areas of POCV; (j) pump pressures for side 'a'(solid) and side 'b' (dotted).

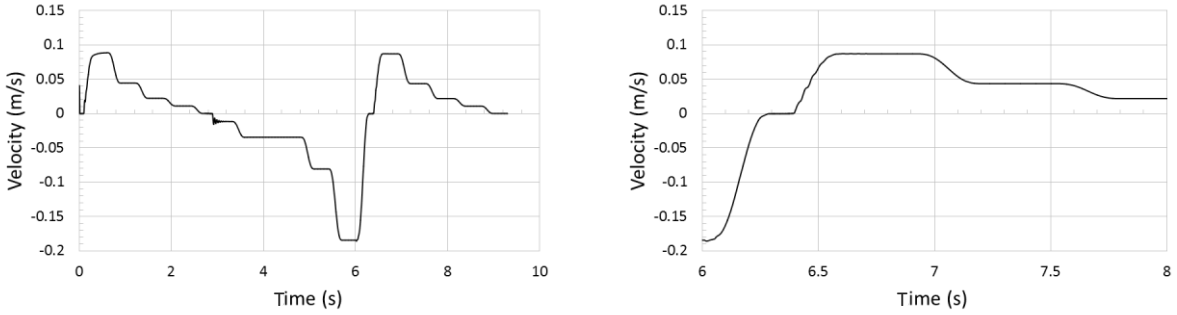

(a)

(b)

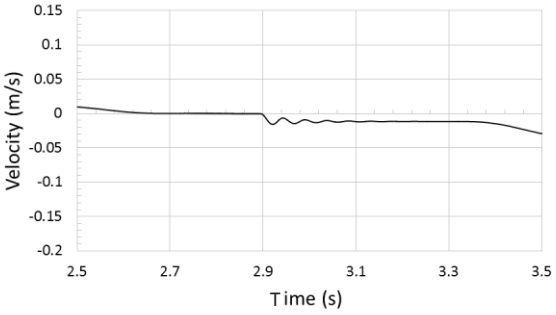

(c)

Figure 5.16**:** Response of multistep polynomial input (configuration 2) after optimization, mass 41 kg attached (s_3 = 1.5, s_4 = 1.2, K_{pilot3} = 1.9, K_{pilot4} = 1.02): (a) actuator velocity; (b) zoomed in a region of actuator velocity; (c) zoomed in a region of actuator velocity.

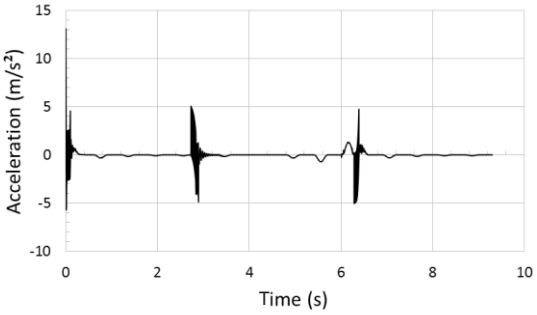

(d)

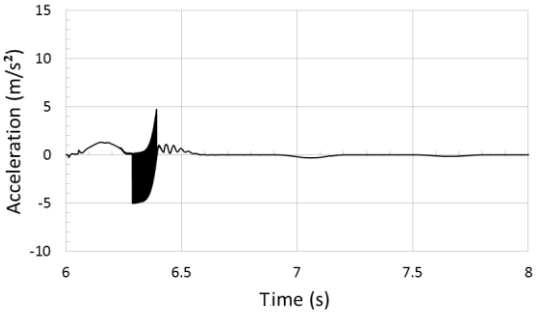

(e)

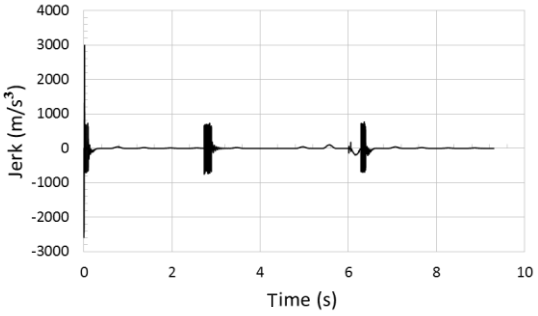

(f)

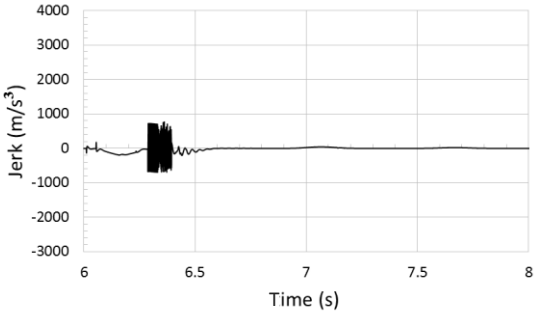

(g)

Figure5.16 (cont.): (d) Actuator acceleration; (e) zoomed in a region of actuator acceleration; (f) actuator jerk; (g) zoomed in a region of actuator jerk.

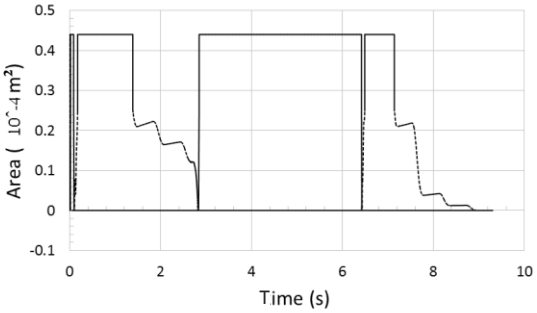

(h)

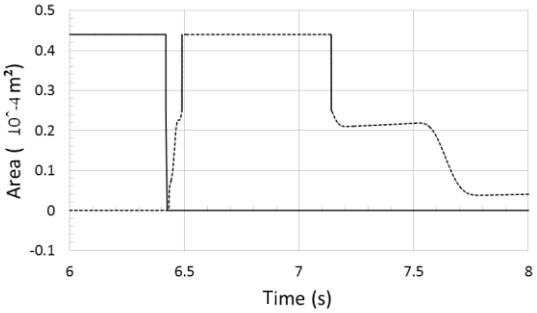

(i)

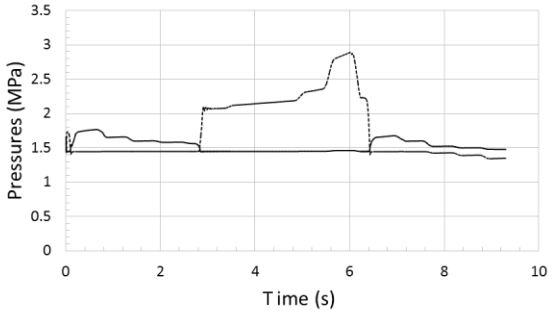

(j)

Figure 5.16 (cont.): (h) Areas of POCV side 'a'(solid) and side 'b' (dotted); (i) zoomed in a region of Areas of POCV; (j) pump pressures for side 'a'(solid) and side 'b' (dotted).

By comparing the results before and after optimization for low loads (Figures 5.15 and 5.16), the performance is improved after using optimal parameters as undesirable velocity regions are reduced resulting in better performance.

5.5.3 Experimental evaluation:

The experimental results are performed on configuration 2 only (as valves for implementation of optimal values were available for configuration 2 only), using both multistep polynomial and step inputs. Results before and after optimisation at high load with multistep polynomial are shown below:

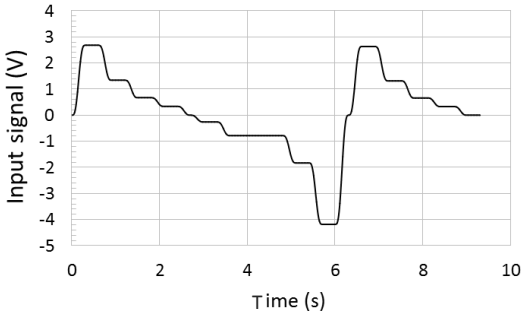

(a)

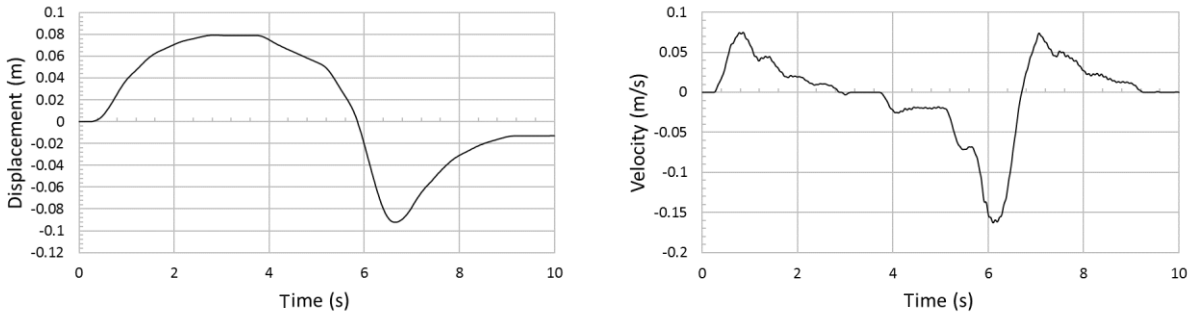

(b) (c)

Figure 5.18 Response of multistep polynomial input (configuration 2) before optimization, mass 245 kg (s_3 = 2, s_4 = 1.5): (a) control signal (V); (b) actuator displacement (m); (c) actuator velocity.

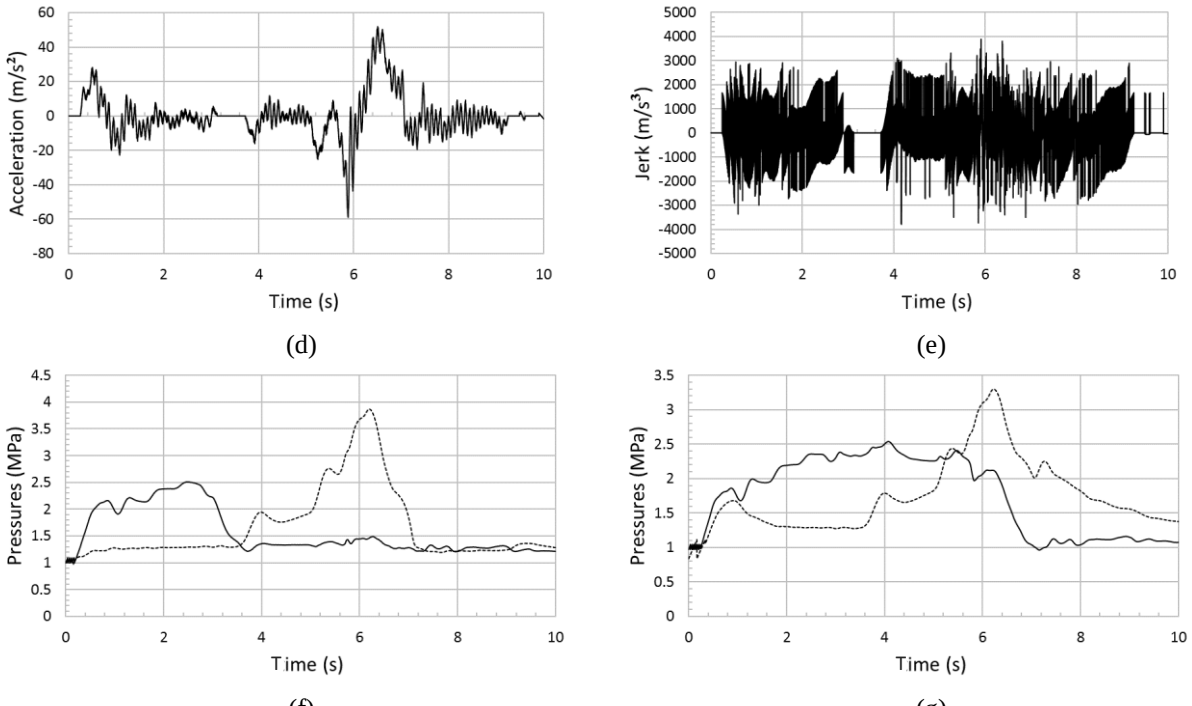

(d) (e)

(f) (g)

Figure 5.17(cont.): (d) Actuator acceleration; (e) actuator jerk (f)pump pressures for side 'a'(solid) and side 'b' (dotted); (g) actuator pressures for side 'a'(solid) and side 'b' (dotted).

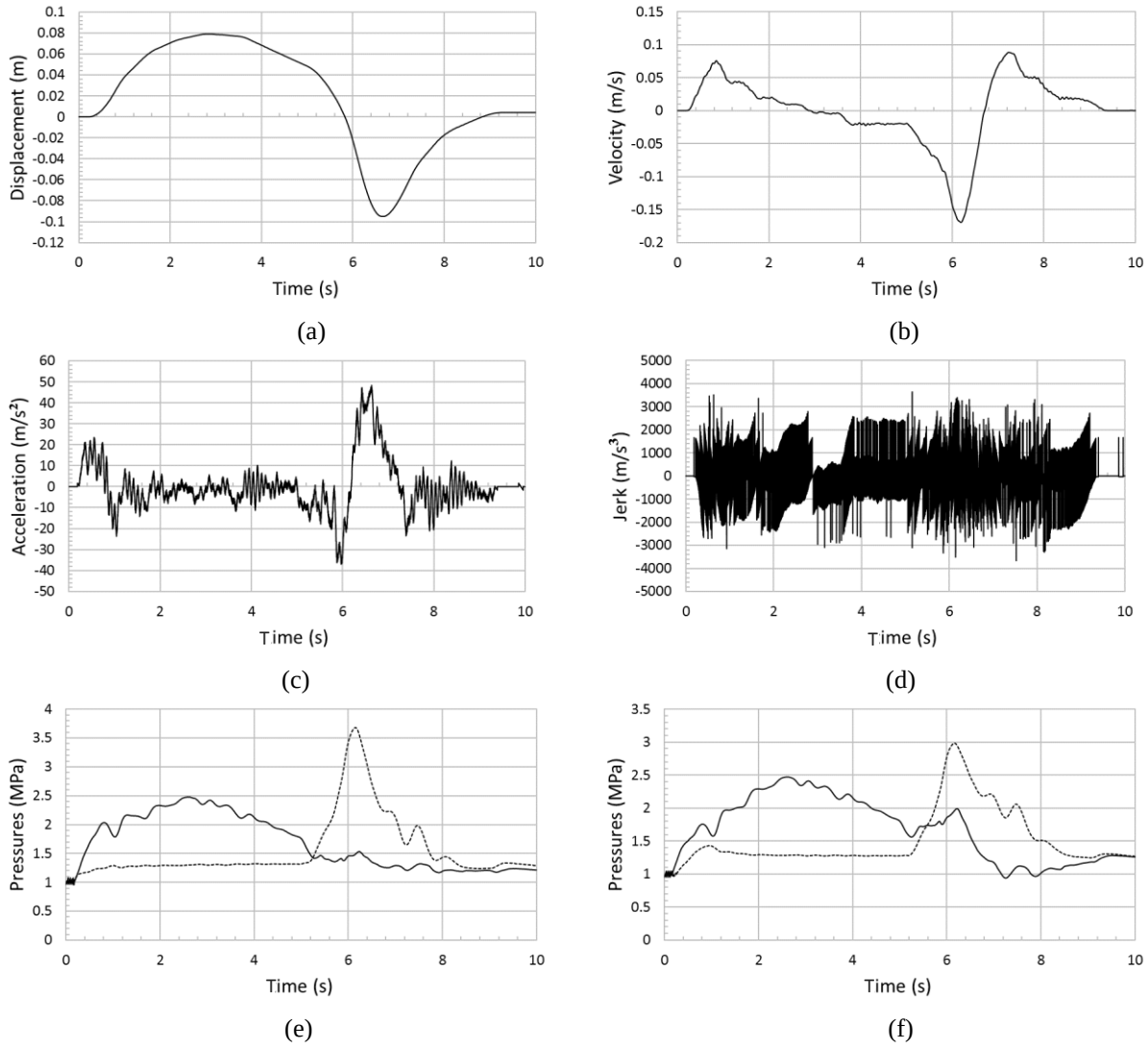

Figure 5.19 Response of multistep polynomial input (configuration 2) after optimization, mass 245 kg attached (s_3 = 1.44, $s_4 = 1.22$): (a) actuator displacement; (b) actuator velocity; (c) actuator acceleration; (d) actuator jerk; (e) pump pressures for side 'a'(solid) and side 'b' (dotted); (f) actuator pressures for side 'a'(solid) and side 'b' (dotted).

The experimental results at high load (Figure 5.17 and 5.18), with multistep polynomial input, before and after optimization are equivalent in terms of rms values of jerk as in table 5.1. Also, we have [$s_3 = 2$ and $s_4 = 1.5$] in optimal configuration, which is same as design of configuration 2 before optimization. This implies that the counterbalance valves setting is already set to optimal values, but there is less scope of improvement in this case (as its already close to optimal values) where [1.5 5] search space is used for high loads in configuration 2.

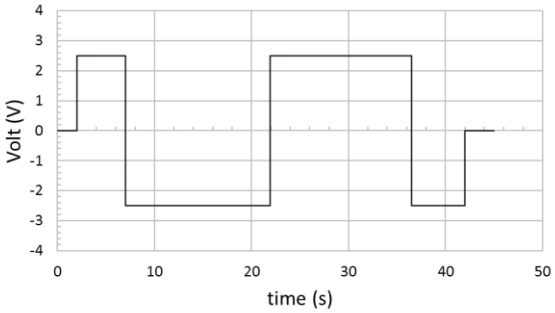

(a)

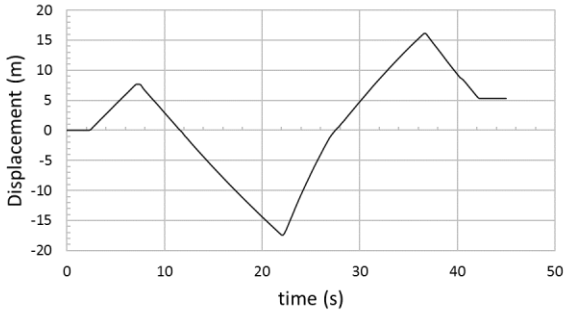

(b)

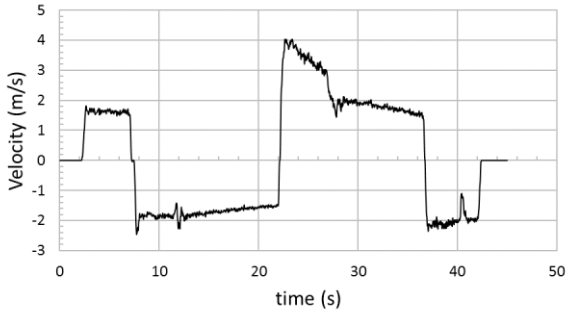

(c)

Figure 5.20 Response of alternating step input (configuration 2) before optimization, mass 245 kg attached: (a) control signal (V); (b) actuator displacement (m); (c) actuator velocity.

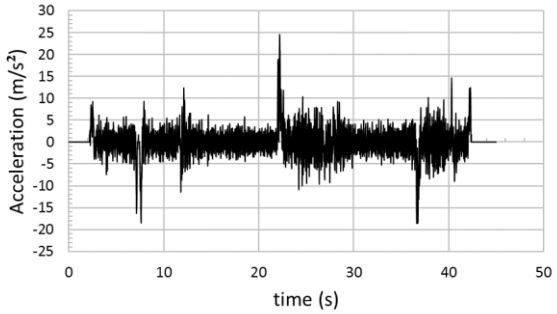

(d)

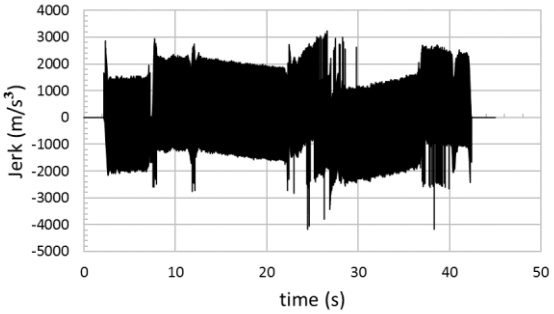

(e)

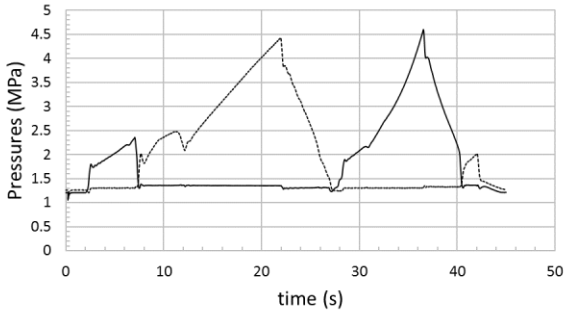

(f)

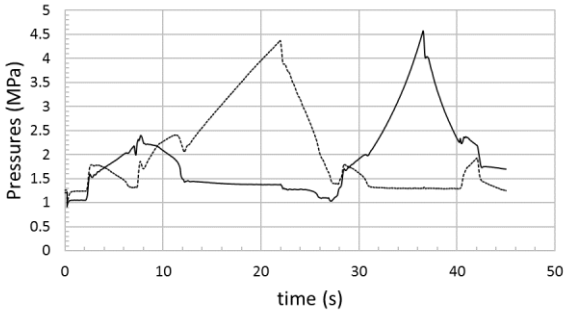

(g)

Figure 5.19 (cont.): (d) Actuator acceleration; (e) actuator jerk (f)pump pressures for side 'a'(solid) and side 'b' (dotted); (g) actuator pressures for side 'a'(solid) and side 'b' (dotted).

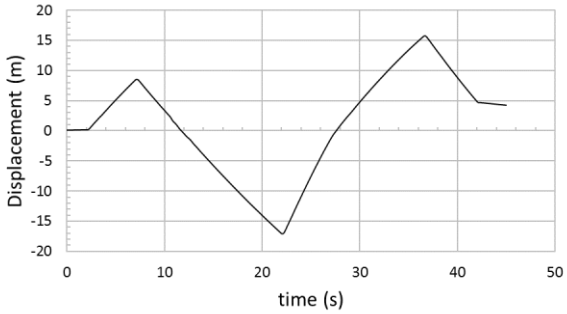

(a)

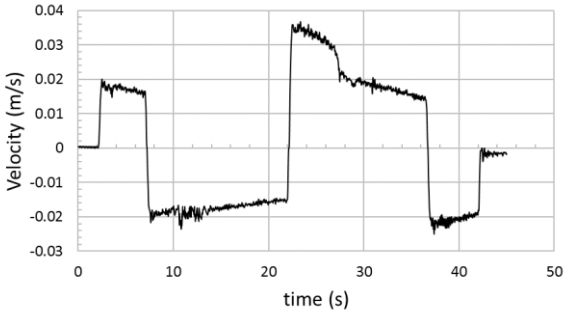

(b)

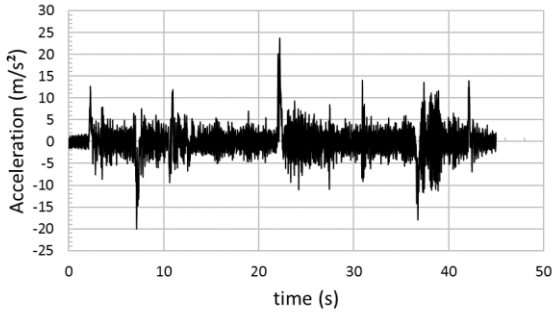

(c)

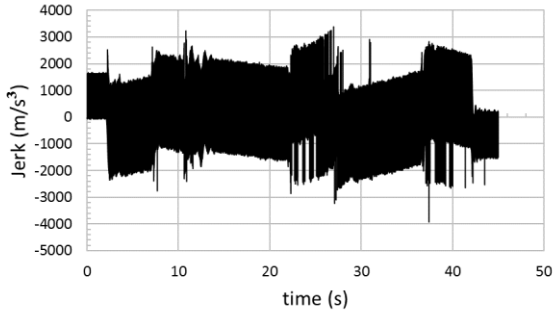

(d)

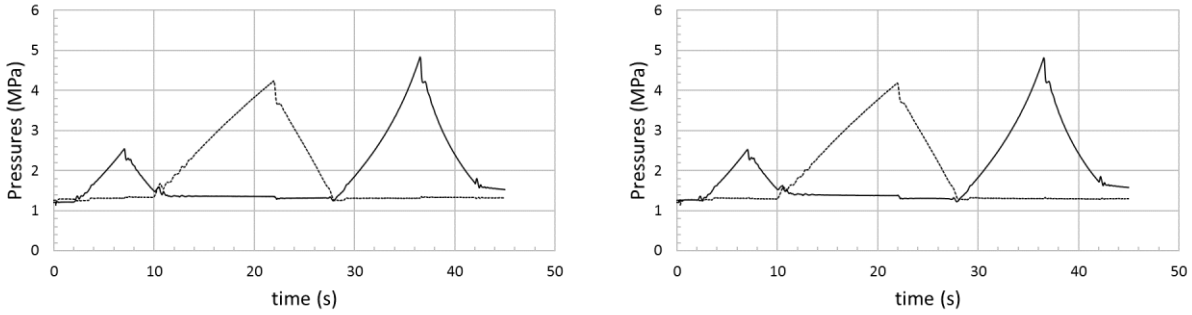

(e) (f)

Figure 5.21 Response of alternating step input (configuration 2) after optimization, mass 245 kg attached (s_3 = 1.44, s_4 = 1.22): (a) actuator displacement (m); (b) actuator velocity; (c) actuator acceleration; (d) actuator jerk; (e) pump pressures for side 'a'(solid) and side 'b' (dotted) (f) actuator pressures for side 'a'(solid) and side 'b' (dotted).

For square input, at high load (Figure 5.20), the performance of optimized design is much better as compared to results before optimization (Figure 5.19). Furthermore, in table 5.1, we see that rms value of jerk for optimized design is lower. It should be noted that at zero input, results of are more jerky as compared to results before optimization, which is attributed to the fact that only 1.43 rotations are used for $\mathrm{CBV_A}$, while as, 2 rotations are used for $\mathrm{CBV_A}$ before optimization (implies more resistance on $\mathrm{CBV_A}$used before optimization resulting in less jerk at zero input).

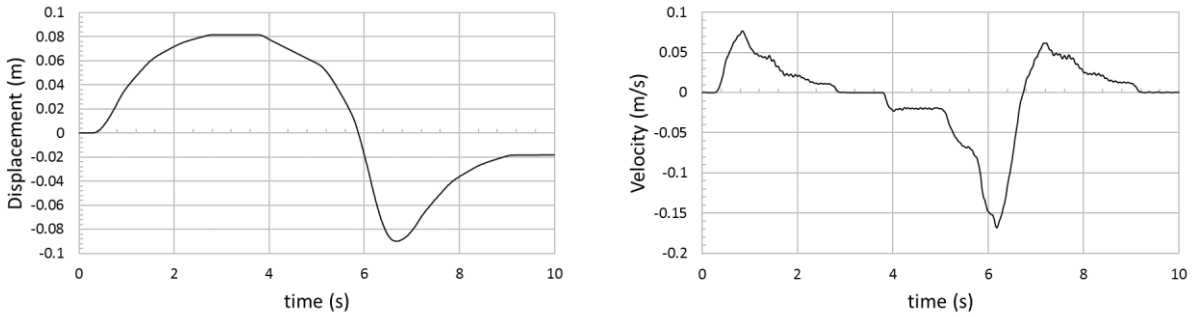

(a) (b)

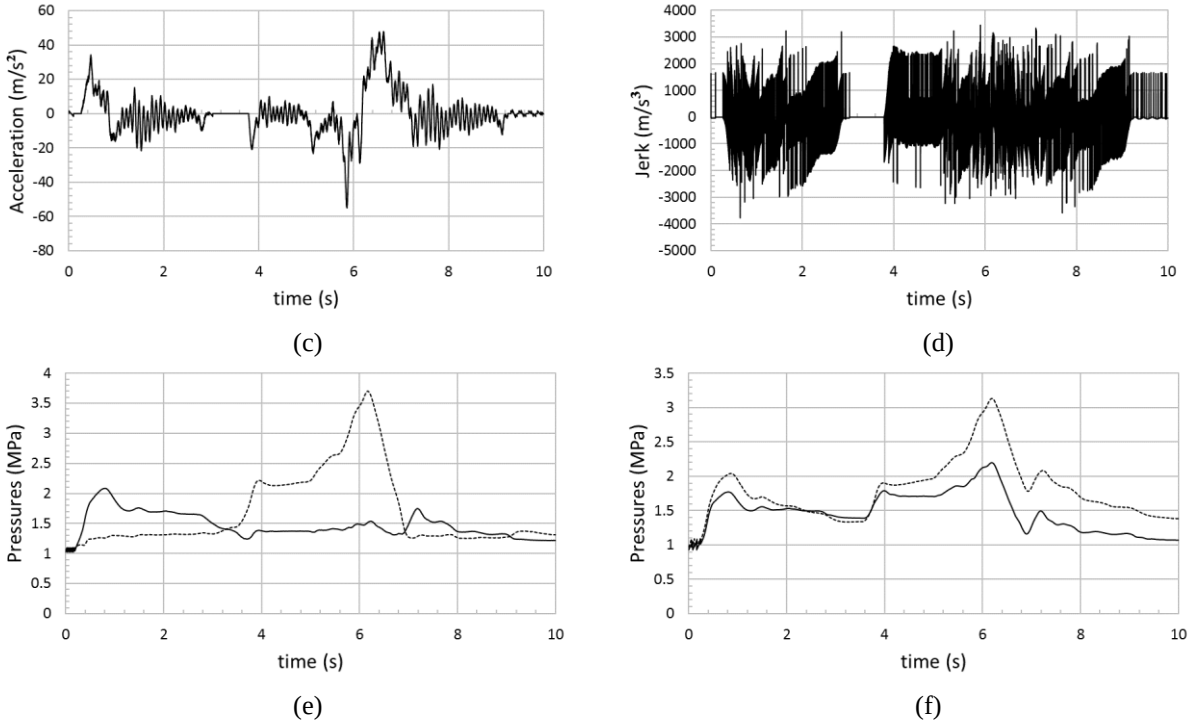

(c) (d)

(e) (f)

Figure 5.22 Response of multistep polynomial input (configuration 2) before optimization , mass 41 kg, attached: (a) actuator displacement (m); (b) actuator velocity; (c) actuator acceleration; (d) actuator jerk; (e)pump pressures for side 'a'(solid) and side 'b' (dotted); (f) actuator pressures for side 'a'(solid) and side 'b' (dotted).

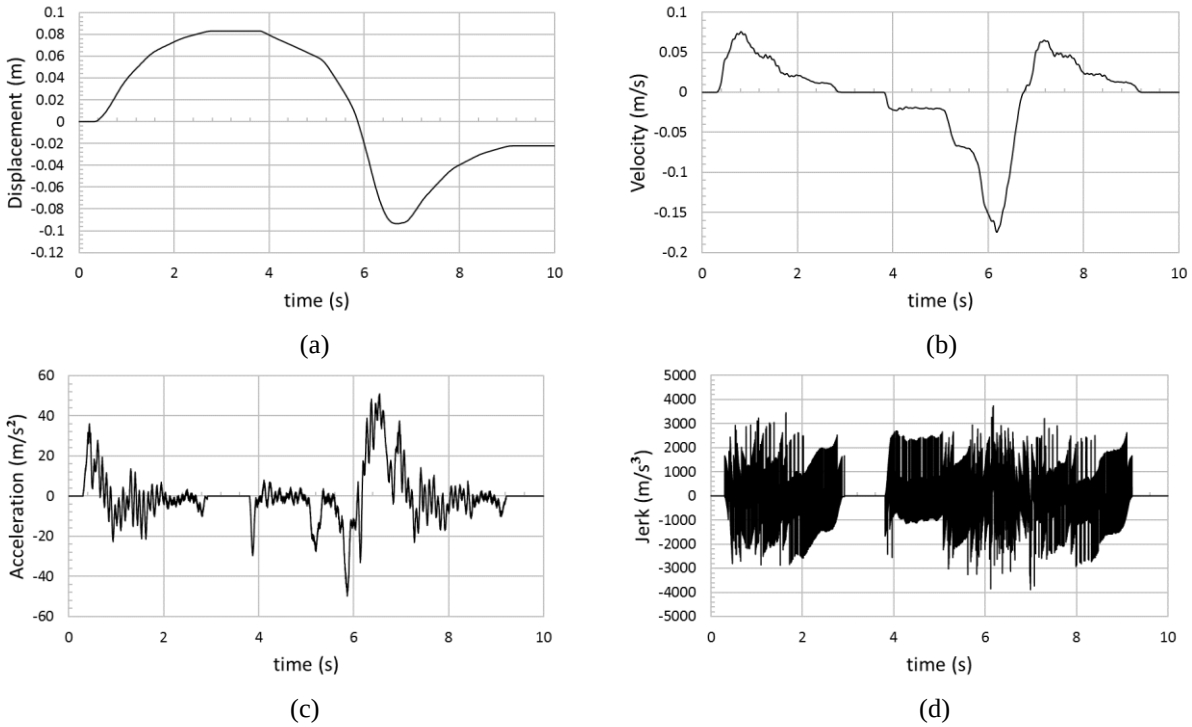

(a) (b)

(c) (d)

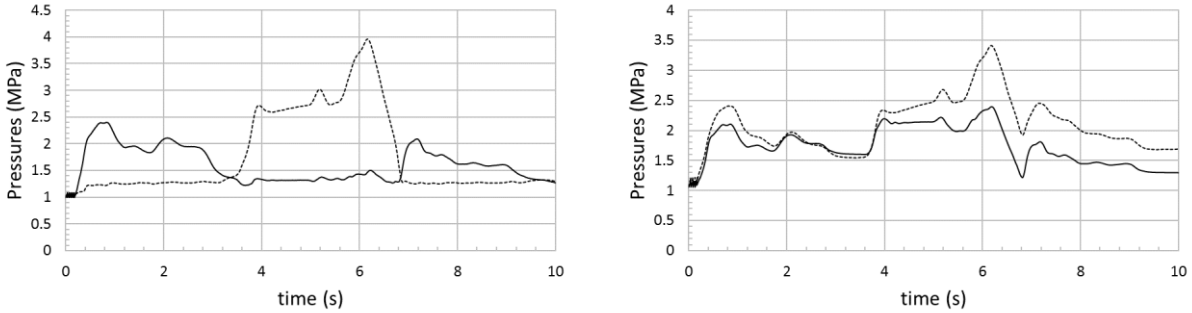

(e) (f)

Figure 5.23 Response of multistep polynomial input (configuration 2) after optimization , mass 41 kg (s_3 = 2.31, s_4 = 1.79): (a) actuator displacement (m); (b) actuator velocity; (c) actuator acceleration; (d) actuator jerk; (e) pump pressures for side 'a'(solid) and side 'b' (dotted); (f) actuator pressures for side 'a'(solid) and side 'b' (dotted).

The experimental results shown for low load (Figure 5.21 and 5.22), with multistep polynomial input, before and after optimization show that rms values of jerk is less in case of optimized design (table 5.1). Performance (velocity) is better (smoother) as compared to non-optimal parametric configuration.

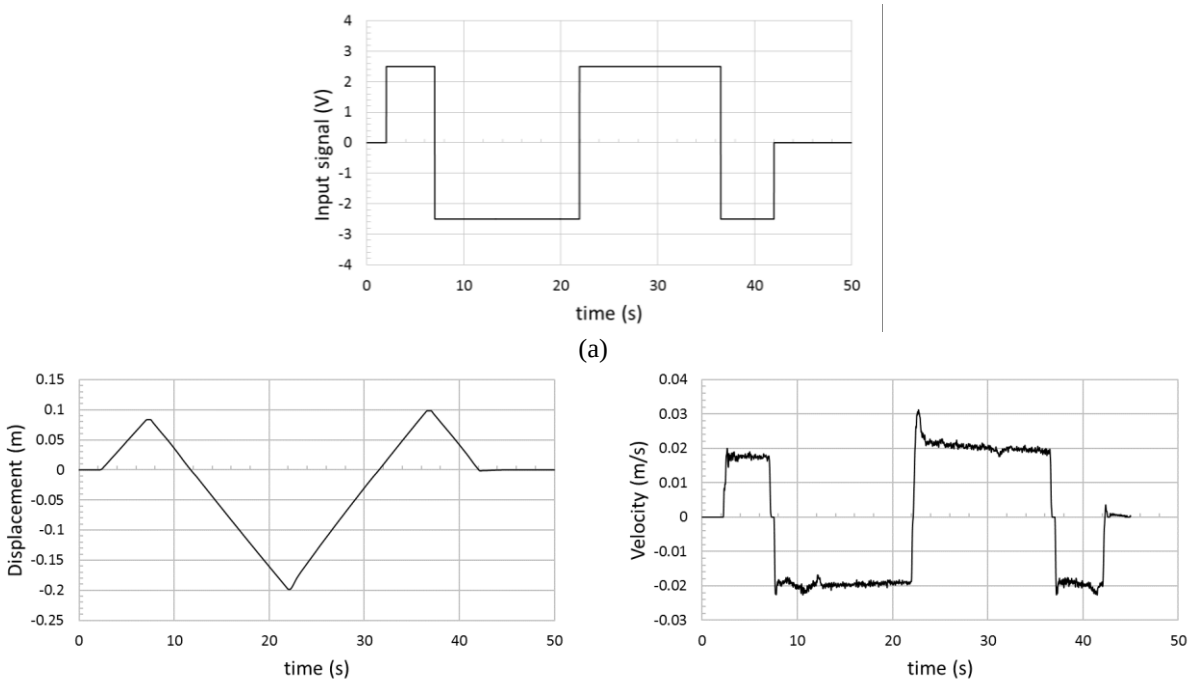

(a)

(b) (c)

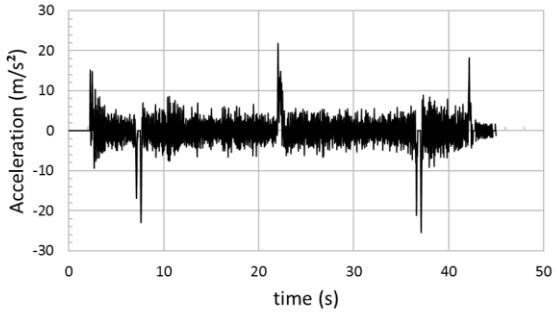

(d)

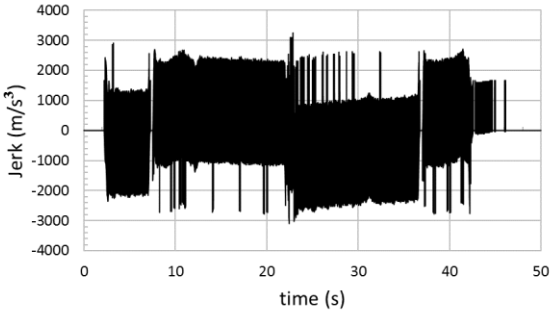

(e)

Figure 5.24 Response of alternating step input (configuration 2) before optimization , mass 41 kg attached: (a) control signal (V); (b) actuator displacement (m); (c) actuator velocity; (d) actuator acceleration; (e) actuator.

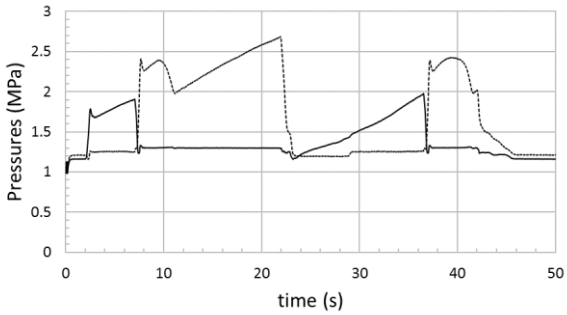

(f)

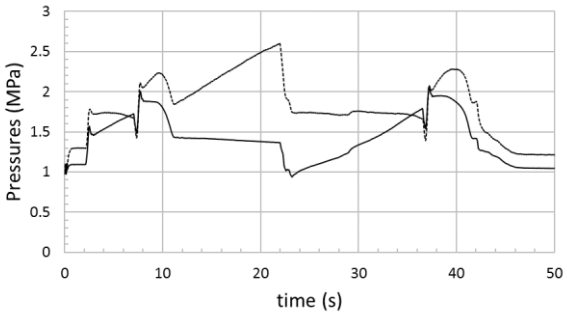

(g)

Figure 5.23(cont.): (f) Pump pressures for side 'a'(solid) and side 'b' (dotted); (g) actuator pressures for side 'a'(solid) and side 'b' (dotted).

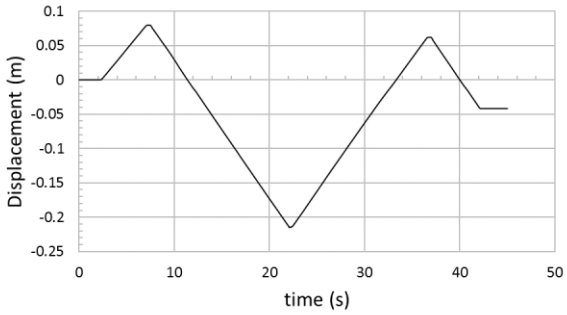

(a)

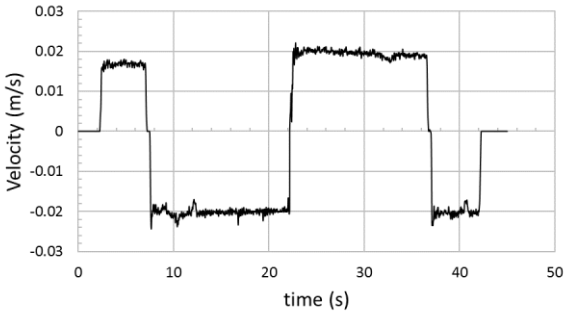

(b)

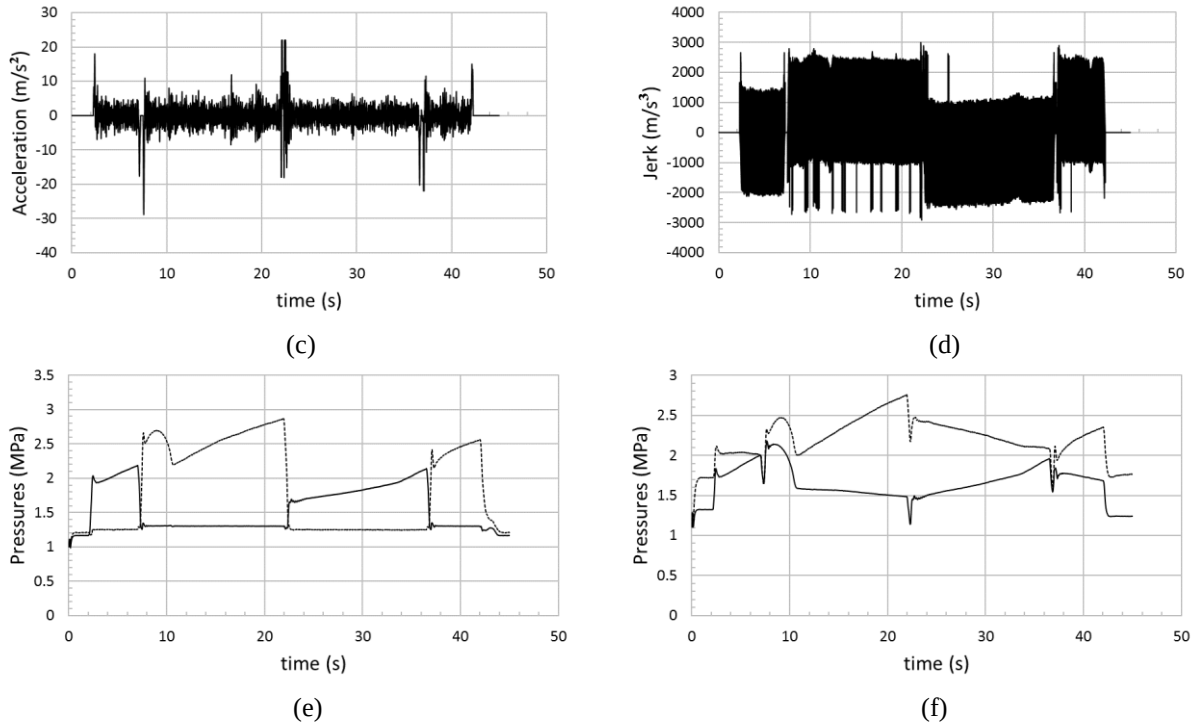

Figure 5.25 Response of alternating step input (configuration 2) after optimization, mass 41 kg attached (s_3 = 2.31, s_4 = 1.79): (a)actuator displacement (m); (b) actuator velocity; (c) actuator acceleration; (d) actuator jerk; (e) pump pressures for side 'a'(solid) and side 'b' (dotted); (f) actuator pressures for side 'a'(solid) and side 'b' (dotted).

Table 5.4. Experimental root mean square values of jerk under various loading conditions and input types

Load (kg)	Type of input	Case	value of objective function (rms jerk)
245	Multistep Polynomial Input	After optimization	1022.34
245	Multistep Polynomial Input	Before optimization	1021.11
245	Square Input	After optimization	1047.42
245	Square Input	Before optimization	1066.68
41	Multistep Polynomial Input	After optimization	1000.52
41	Multistep Polynomial Input	Before optimization	1003.27
41	Square Input	After optimization	1025.31
41	Square Input	Before optimization	1023.95

For square input, at low load (Figure 5.23 and 5.24), the performance of optimized design is much better where assistive velocity peak is eliminated in extension (Figure 5.23 c and 5.24 b), which will result in least control effort in closed loop for such cases. The results of rms

values of objective function are equivalent before and after optimization as shown in table 5.4. The experimental results obtained using multistep polynomial at high load show that rms value of objective function before (1021.11) and after (1022.34) optimization are equivalent, while as if step input is used then optimized design shows better performance(table 5.4). Rms values of objective function before and after optimization in case of step input are 1066.68 and 1047.42, respectively. At low loads for step input, the rms values of objective function are equivalent before (1023.95) and after (1025.31) optimization. For multistep polynomial input, the results at low loads before (1003.27) and after (1000.52) optimization show slight improvement.

Simulation results in both configurations show improved performance after optimization. The performance is significantly improved in case of configuration 1 where overlapping of areas (hence overlapping of pressures) is not seen after optimization. In case of configuration 2 no overlapping of areas is seen before optimization, hence scope of improvement is relatively less (as compared to configuration 1) as seen in simulation. Experimental tests were only performed on configuration 2 (as optimal values could be implemented on configuration 2 only), where performance improvement is seen while optimized configuration design is used.

5.6. Summary

For initial component selection, system parameters to be optimized are identified. An optimization criterion was proposed for both configurations. Cracking pressures of valves and their maximum opening areas are discussed. Proposed criteria for choosing an optimal hydraulic circuit configuration is proposed. In configuration 1, ten parameter optimization is chosen in order to optimize the system performance. cracking pressure, effective pressure (when valve undergoes full valve cracking), pilot ratio, maximum opening area of valve and coefficient (relating flow area to effective pressure) are chosen in this case. In configuration 2, four parameter optimization is chosen where pilot ratio and cracking pressures are used for optimization.

Simulation results of two hydraulic configurations were discussed. Results before and after optimization are compared. A multistep polynomial input and a step input are used. In case of configuration 1, results before optimization show overlapping of areas of piloted operated check valves, hence affecting velocity and pressures (on both sides of configuration 1). Simulation results after optimization show removal of overlapping of areas and hence better performance. In case of configuration 2, we see slight improvement in results (relatively compared to configuration 1) after optimization i.e. there is less scope of improvement in performance, as no area overlapping occurs in configuration 2. Experimental tests are performed on configuration 2. Experimental results before and after optimization are compared. Results show that optimization improves the performance of configuration 2.

Chapter 6

Controller Design

6.1. Concept of Quantitative feedback theory

The main focus of this research is to design a simple-to-implement Quantitative feedback theory (QFT) velocity controller. QFT design technique guarantees robust performance and stability within a specific range of input-outputs for the system. QFT control technique is employed here to control the actuator velocity. In QFT design technique, a family of frequency responses of uncertain plant is required. QFT technique uses a graphical representation of design criteria for entire range of uncertainties. Figure 6.1, shows an overview of concept of 2-DOF QFT technique where P(s,γ), C(s) and F(s) denote uncertain plant, controller and prefilter respectively. QFT controller design technique has been used to design robust velocity controllers for two hydraulic circuit configurations (configuration 1 and 2). Two controllers are tested in simulation followed by experiments. In configuration 2 the designed controller is tested experimentally, using optimized and non-optimized configuration 2 configurations.

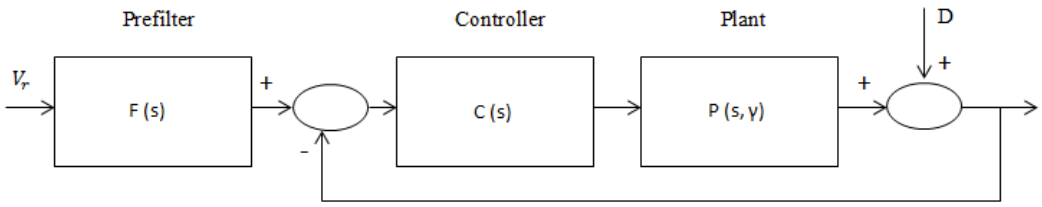

Figure 6.1Two degree-of-freedom QFT control system

In QFT design technique, a controller C(s) and a prefilter F(s) must be designed in order to meet the performance criteria. The performance specifications are chosen by the designer. A trade-off between performance specifications and controller complexity are important.

At each frequency, the frequency response set for the entire range of parametric uncertainties, say P(s,γ) is called a template. These templates are used to generate QFT bounds, which specify desired performance criteria. Steps for designing a controller and desired performance criteria chosen are discussed in section 6.2.5 in more detail. In order to design controllers for each hydraulic configuration, a family of transfer functions is required, based on set of uncertainties obtained from system identification. In order to obtain a set of linear transfer functions CIFER (comprehensive identification from frequency responses) technique is used.

6.2. Design of QFT Controller for hydraulic circuit with configuration 1

For hydraulic circuit with configuration 1, P(s,α), C1(s) and F1(s) denote uncertain plant, controller and prefilter respectively. C1(s) and a prefilter F1(s) is designed in order to meet the performance criteria. At each frequency, the frequency response set for the entire range of parametric uncertainties, P(s,α), is a template for configuration 1. Equations governing this hydraulic configuration of interest are discussed below.

We have following equations representing system dynamics for configuration 1

$$\dot{x}_p = v_p \tag{6.1}$$

$$\dot{v}_p = \frac{(p_A A_a - p_B A_b) - F_f - F_L)}{m} \tag{6.2}$$

$$\dot{p_A} = \frac{K_{oil}(Q_A - A_a v_p)}{V_a + A_a x_p} \tag{6.3}$$

$$\dot{p_B} = \frac{K_{oil}(-Q_B + A_b v_p)}{V_b - A_b x_p} \tag{6.4}$$

where Q_a, Q_b,Q_A , Q_B , represent flows at two pump ports and at two actuator ports respectively (fig 3.1). If 'α_r' denotes the area ratio where α_r=A_b/A_a, x_1 is displacement of piston (x_p), x_2 is velocity(v_p),x_3 is pressure on left port of actuator (p_A), x_4 is the pressure on the right port of actuator (p_B), F_L is the load force and F_f denotes friction then equation 6.2 can be rewritten as:

$$\dot{x_2} = \frac{(x_3 A_a - \alpha_r x_4 A_a) - F_f - F_L)}{m} \tag{6.5}$$

Q_A and Q_B are related as:

$$Q_B = \alpha_r Q_A \tag{6.6}$$

Flow at two ports of the pump is given by $Q_{pmp} = Q_a = Q_b$ = n V_d β_p where n is the pump speed, V_d is pump displacement volume and β_p is the normalized pump displacement. Then variable displacement hydraulic pump can be represented by:

$$\tau_p \dot{\beta_p} + \beta_p = k_{p1}\, v_e \tag{6.7}$$

where τ_p and k_{p1} represent the time constant and gain of pump, respectively. v_e denotes input voltage. Assuming $(V_a + A_a x_1)/K_{oil} \approx (V_b - A_b x_1)/K_{oil} \approx (V_a + V_b)/2K_{oil} = C_H$ (6.71)

with actuator operating close to mid position, where C_H denotes hydraulic compliance and $F_L = k_L \times x_1$ we get (equation 6.1-6.71) :

$$sX_2(s) = 1/m[(\{\frac{A_a}{sC_H}\}\{\frac{nV_d\, k_{p1}}{1+\tau_p s}\}V_e(s) - A_a X_2(s)) - (\{\frac{\alpha_r A_a}{sC_H}\}\{\frac{-\alpha_r nV_d\, k_{p1}}{1+\tau_p s}\}V_e(s)$$

$$- A_b X_2(s)) - (k_L X_1) - (f_v X_2)]$$

where s is the Laplace operator. Rearranging the equation and assuming a linear relationship between input voltage (v_e) and flow output (Q_{pmp}) of the pump i.e. $Q_{pmp} = k_{pmp} \times v_e$ where k_{pmp} represents the coefficient relating pump flow and voltage, the expression for transfer function becomes:

$$\frac{X_2(s)}{V_e(s)} = \frac{A_a nV_d\, k_{pmp}(1 + \alpha_r{}^2)}{s^2 C_H M_{eq} + sC_H f_v + A_a{}^2 + \alpha_r A_a A_b + C_H k_L} \tag{6.8}$$

$$\frac{X_2(s)}{V_e(s)} = \frac{d_{06}}{d_{01}s^2 + d_{02}s + d_{03}} \tag{6.81}$$

where $d_{06} = A_a nV_d\, k_{pmp}(1 + \alpha_r{}^2)$, $d_{01} = C_H M_{eq}$, $d_{02} = C_H f_v$, $d_{03} = A_a{}^2 + \alpha_r A_a A_b + C_H k_L$

6.2.1 System identification for family of linear transfer functions

In order to get more accurate transfer function where unmodelled uncertainties due to various loading conditions, velocities, or due to linearization process of non-linear system, are taken into account, a more practical procedure is required. A family of transfer functions at various loads and velocities is obtained. For this purpose system identification technique i.e. obtaining frequency responses from measured data called CIFER (comprehensive identification from frequency responses) is used. Here a frequency sweep signal is given as input to the system. Then a best fit transfer function is obtained. A special type of chirp signal is designed which is used for system excitation.

A chirp signal is constructed as follows:

$$\delta_{sweep} = H_3 \, sin[\int_0^t \omega\,(t)dt] \tag{6.10}$$

Where H_3 is the amplitude of the chirp signal and usually should fade in and out. Since system parameters may change with frequency, hence single frequency test is not accurate enough for system identification. Hence sweeping over a wide range of frequencies is required where frequency $\omega(t)$ is denoted by:

$$\omega(t) = \omega_{min} + H_2 \left(e^{\frac{H_1 t}{T_{max}}} - 1 \right) (\omega_{max} - \omega_{min}) \tag{6.11}$$

Where ω_{min} and ω_{max} are the maximum and minimum frequencies. This frequency range is determined by application[30]. ω_{min} is chosen such that the actuator doesn`t reach its limits. It should be noted that ω_{max} should be greater than natural frequency of the system; ω is ω_{max} at t=T_{max} where T_{max} denotes sweep record length. T_{max} is chosen to be at least equal to $8\pi/\omega_{min}$. ω_{min} and ω_{max} were chosen as 0.376 rad$/s$ and 18.85 rad$/s$ respectively. T_{max} = 70 s; H_1 = 4; H_2 =$1/(e^{H_1} - 1)$; with 25% fading in, and 33% fading out. A low-pass prefilter with cut-off frequency of ω_{max} is used to supress high frequency content in excitation; as white noise equal to 10% of amplitude is added to sweep signal in order to enrich its spectral content.

CIFER uses advanced form of FFT algorithm which uses Chirp-Z transform and composite optimal window techniques, resulting in better quality frequency responses as compared to standard FFT(Tischler and Remple, 2012). Since it is directly applied to experimental data, it results in a more accurate frequency response representation of real system, hence used in this research.

Uncertainties were introduced by varying load and performing experiments at zero load, 122 kg, 245 kg and 368 kg. Velocity variations were introduced by using various inputs with a maximum of 1.18 V, 2.68 V and 4.18V. Three types of symmetrical chirp signals were used for system excitation. A fourth type of chirp signal, an unsymmetrical chirp signal was also used to include and analyse more uncertainties incorporated due to the area differential problem associated in single-rod systems, with a maximum of 2.68 V on one side and -2.28 V on other side (uncertainties found were within the range of uncertainties found using symmetric chirp signals). Figure 6.2 shows three types of symmetrical input chirp excitation signal used. The system is excited using these different chirp inputs in order to incorporate uncertainties at various loads and velocities, and hence to identify range of model parameters more accurately. It also ensures that uncertainties due to unmodelled phenomena or during linearization of nonlinear systems are also incorporated into the system parameters, since experimental data is directly used for system identification to get the best fit transfer function. Identified transfer function is fitted with measured frequency response from 0.37 rad/s to 7.5 rad/s. Finally, a QFT controller is designed based of this family of transfer functions obtained for configuration 1.

Figure 6.2 shows a symmetrical input chirp excitation signal with a maximum value of 2.68 V used. Displacement, velocity responses obtained for circuit configuration 1 are shown for 122 kg load attached.

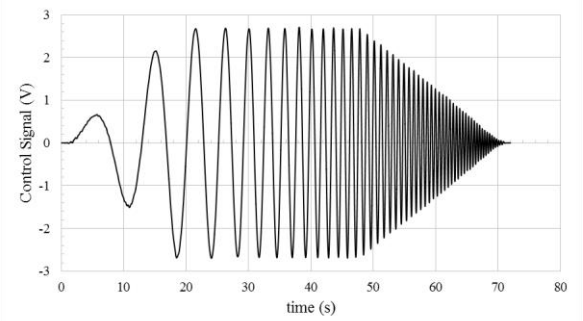

(a)

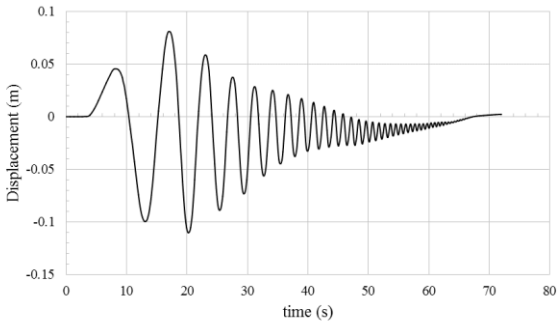

(b)

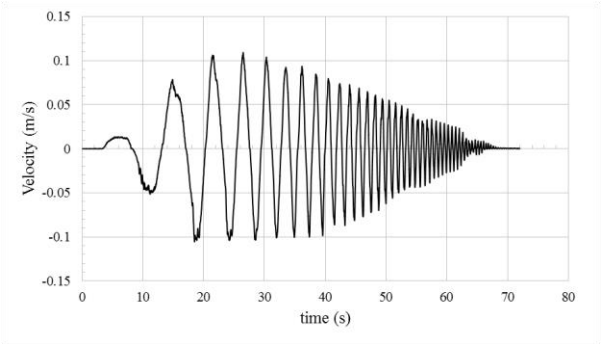

(c)

Figure 6.2 System response for input chirp excitation signal with a maximum of 2.68 V and 122 kg mass attached (configuration 1): (a) input chirp excitation signal with a maximum of 2.68 V; (b) displacement of actuator; (c) velocity of actuator.

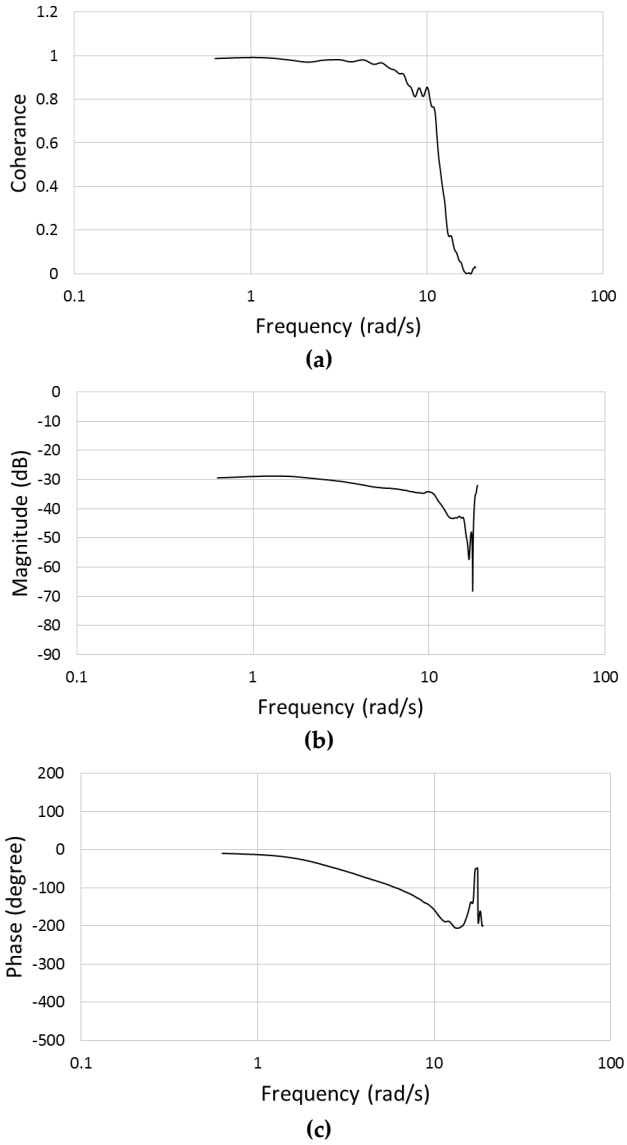

Figure 6.3 System identification results from CIFER for input chirp excitation signal with a maximum of 2.68 V and 122 kg mass attached (configuration 1): (a) coherence; (b) magnitude; (c) phase.

Magnitude, phase and coherence obtained via system identification using CIFER are shown in Figure 6.3. Coherence function denotes linearity and hence accuracy of measured frequency response. A value of 1 means completely linear system. Due to various nonlinearities in the system, noise in output signal and poor signal-to-noise ratio (SNR), this value can be reduced [31]. Frequency range with coherence more than 0.6 is considered acceptable. Figure 6.3 (a) shows that coherence is very less at and beyond 10 rad/s. Acceptable coherence value up to 7.5

rad/s is chosen. Figure 6.4 shows identified transfer function fitted with measured frequency response for circuit configuration 1.

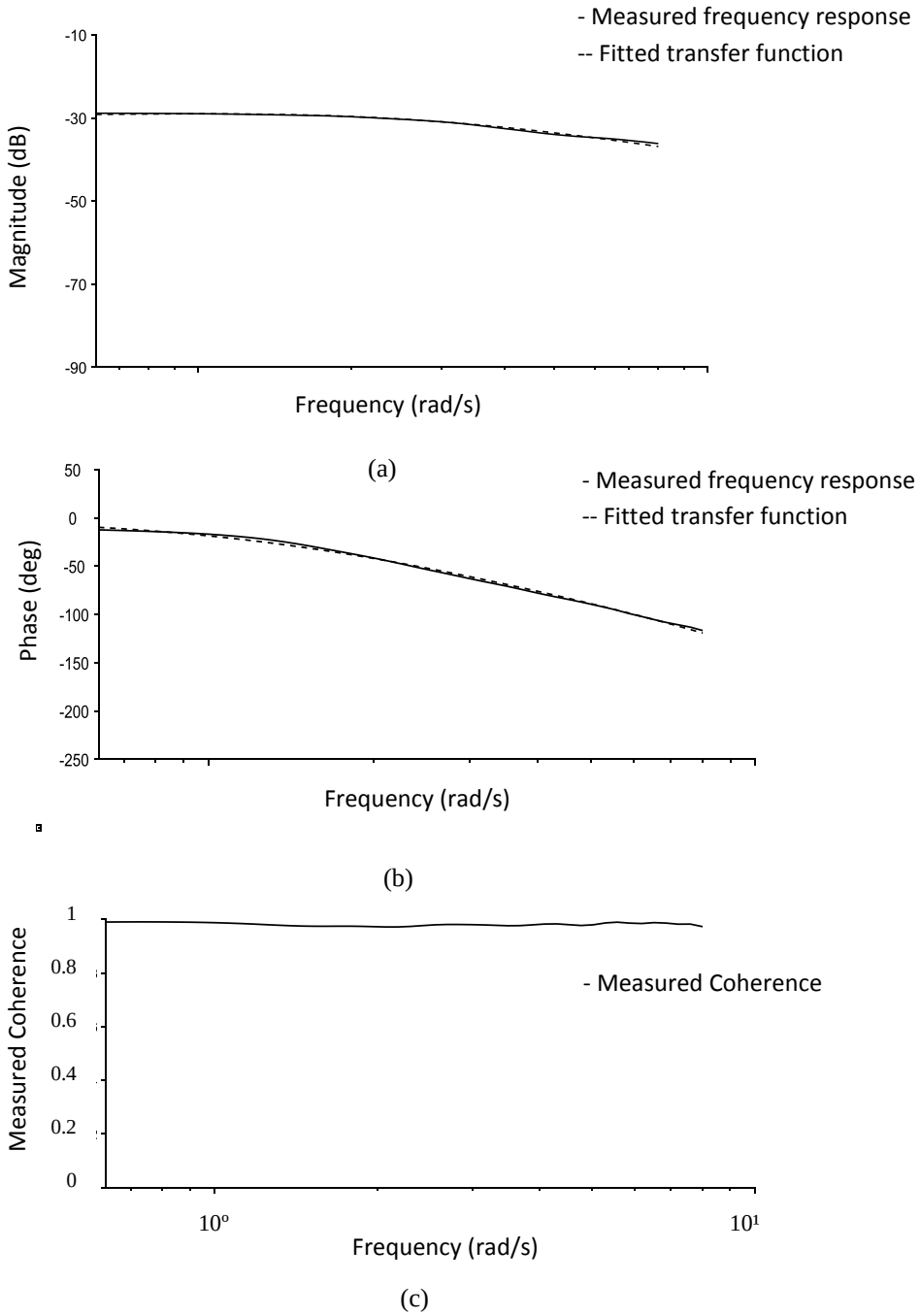

Figure 6.4 Comparision between experimental result and results obtained from system identification from CIFER for configuration 1:(a) magnitude; (b) phase; (c) measured coherence.

Figure 6.5 and 6.6 shows other two more input chirp excitation signals used with a maximum value of 1.18 V and 4.18 V.

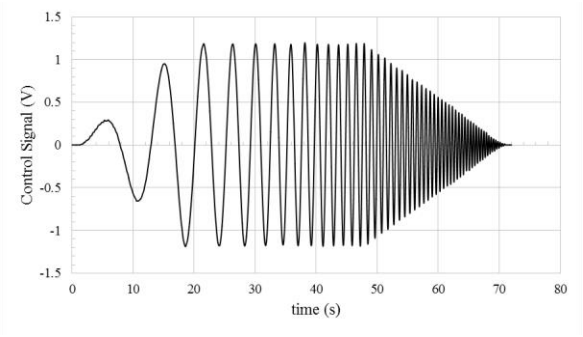

Figure 6.6 Input chirp excitation signal with a maximum of 1.18 V.

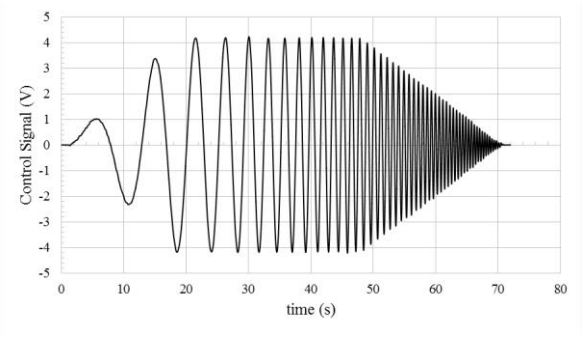

Figure 6.7 Input chirp excitation signal with a maximum of 4.18 V.

Figure 6.7 shows system response for zero load and low velocity. With increase in frequency and time, actuator displacement becomes more positive, hence more extension as compared to retraction in a single-rod system due to bias force at zero load. A non-zero velocity can also be seen at the beginning, since cylinder continues to extend even at zero input given to system at zero load. At very low frequency the actuator extends and retracts, but at high frequency the actuator moves only in one direction as it is unable to retract due to bias force.

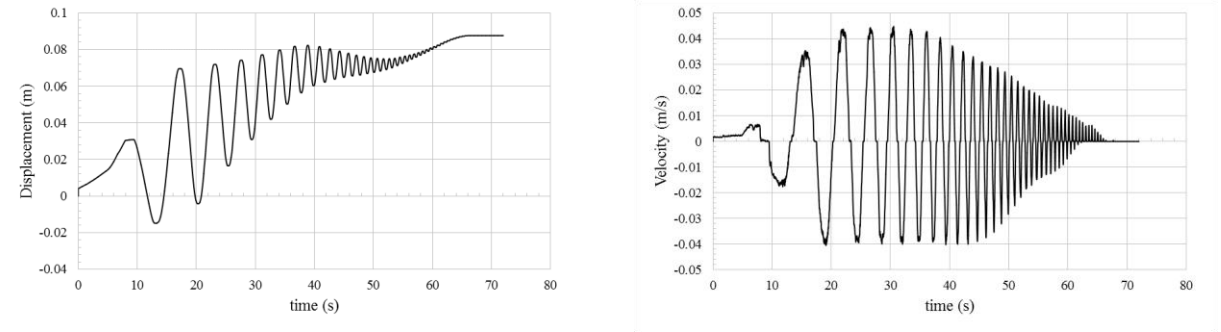

(a) **(b)**

Figure 6.8 Input chirp excitation signal with a maximum of 1.18 V and zero mass attached used (configuration 1): (a) displacement of actuator; (b) velocity of actuator.

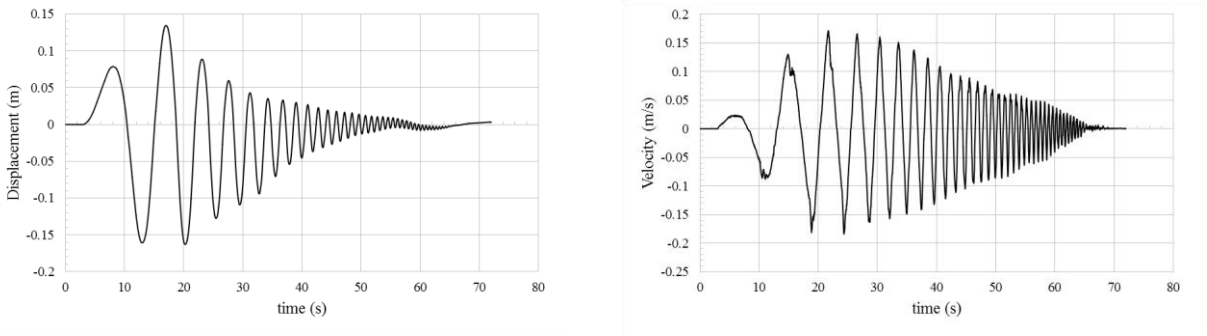

(a) **(b)**

Figure 6.9 Input chirp excitation signal with a maximum of 4.18 V and 245 kg mass attached (configuration 1): (a) displacement of actuator; (b) velocity of actuator.

Figure 6.8 shows system response for 245 kg load and high velocity. With increase in frequency and time, actuator displacement is relatively symmetrical due to increase in both load and velocity which reduces dominating bias force (due to charge pressure and area difference) and friction at low load and low velocity.

Magnitude, phase and coherance results obtained for configuration 1 at various loads and velocities are shown in Figure 6.9

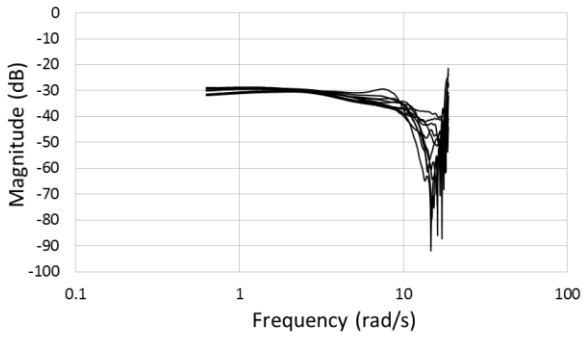

(a)

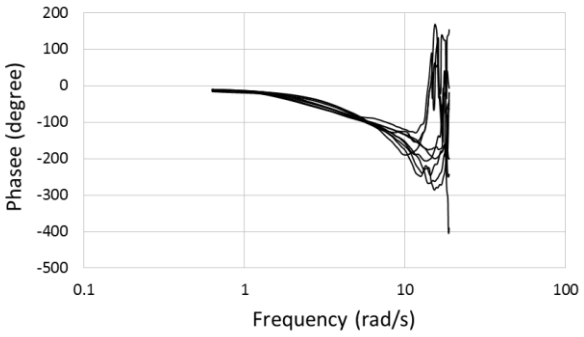

(b)

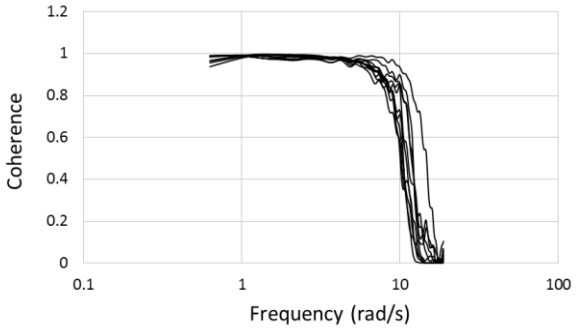

(c)

Figure 6.10 Results from CIFER system identification for configuration 1 at different loads and velocities: (a) magnitude; (b) phase; (c) coherence.

The identified model parameters denoting a family of trasfer functions for circuit confugration 1 are shown in table 6.1. This constitutes the best fitted transfer function obtained from CIFER by taking uncertainties (α) at various loads and velocities into account, in case of configuration 1 for transfer function (TF1) used:

$$\frac{X_2(s)}{V_e(s)} = \frac{e_{05}s + e_{06}}{e_{01}s^2 + e_{02}s + e_{03}} \tag{6.12}$$

where e_{05}, e_{06}, e_{01}, e_{02} and e_{03} are constants obtained via system identification.

Table 6.1. Range of parameters of transfer function of configuration 1(TF1) for external mass attached 0 kg, 122 kg, 245 kg, 368 kg and voltage input signals of 1.18 V, 2.68 V and 4.18 V

e_{05}	e_{06}	e_{01}	e_{02}	e_{03}
0.11748-0.41138	**0.0014723-1.2564**	**1**	**3.56 -14.39**	**0.3638- 47.45**

Based on these uncertainties, a QFT controller for configuration 1 is designed.

6.2.2 Verification of results

Based on system identification a family of transfer functions is obtained for configuration 1(uncertainities for configuration 1 are listed in table 6.1).The transfer functions obtained was verified by comparing the results with experiment tests for this configuration. A chirp signal was used as an input exitation in the transfer function obtained from cifer and results were compared with experimental tests obtained for configuration 1(Figure 6.10).

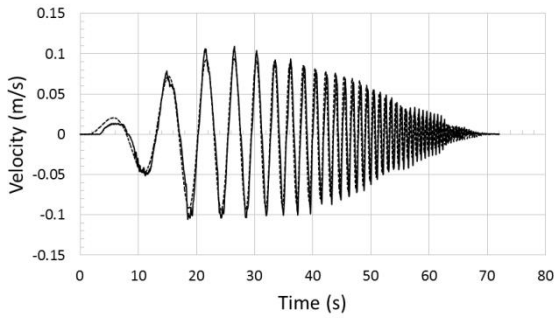

Figure 6.11 Experimental (dotted) and simulation (solid) results shown for configuration 1.

6.2.3 Family of transfer functions

In order to test open loop performances of configuration 1 in both directions, three square input signals (1.18 V, 2.68 V and 4.18 V) were tested on family of transfer functions obtained. Results for configuration 1 are shown in Figures 6.11.

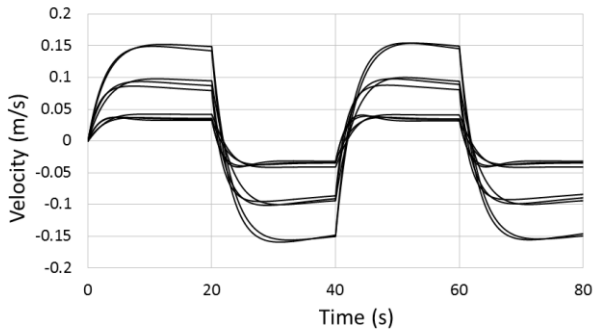

Figure 6.12 Open loop response for family of transfer functions obtained from cifer for configuration 1.

6.2.4 Bode plots and step response

Frequency and time responses for configuration 1 is shown in Figures 6.12 -6.13 as follows:

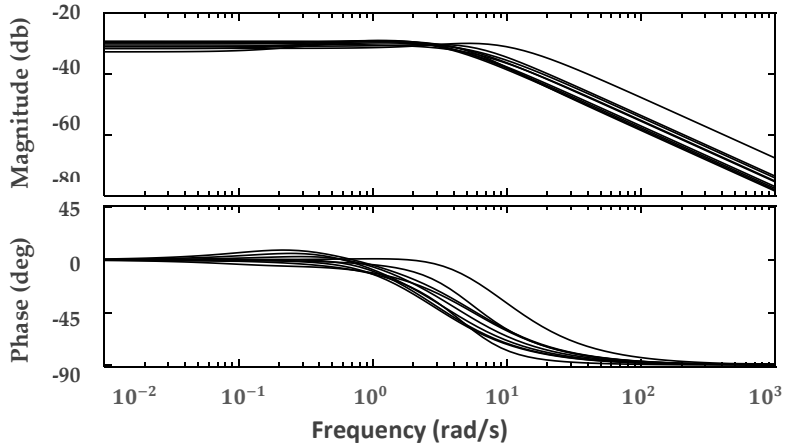

Figure 6.13 Frequency responses of uncertain plant considering variable velocity and uncertain load variations in configuration 1.

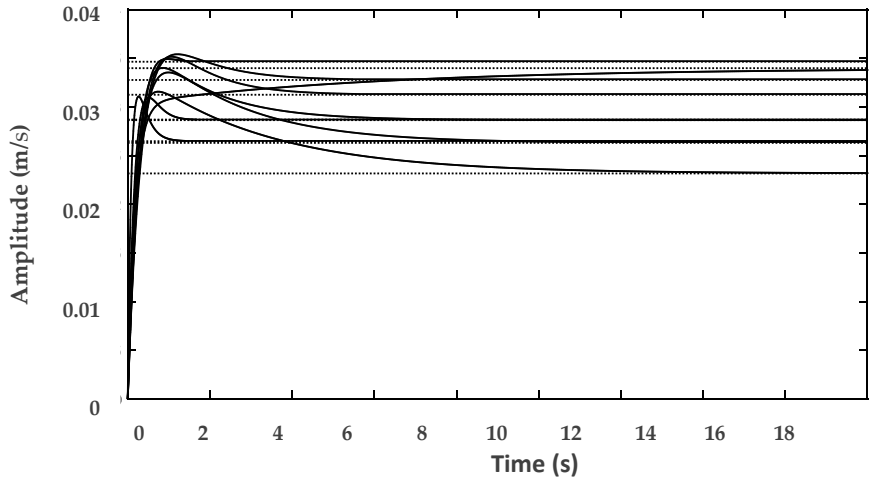

Figure 6.14 Open loop step response for uncertain plant in configuration 1.

6.2.5 Controller Design 1 (Procedure)

In this section main focus of the research is to design a simple controller and then test it on configuration 1. QFT (quantitative feedback theory) control technique is used for designing velocity controller for this hydraulic configuration. QFT is a controller design technique in frequency domain used to develop a robust controller based on plant uncertainties. Robust QFT velocity controller is designed which is verified via simulations and experiments.

The 2-DOF QFT feedback control system is presented in fig 6.1. In QFT design technique, in order to meet performance criteria a controller and a prefilter must be designed where performance specifications are chosen by the designer. For circuit configuration 1, a 2-DOF QFT controller consists of P(s,α), C1(s) and F1(s) denote uncertain plant, controller and prefilter respectively. In table 6.1 parametric range of uncertainties of transfer function considering variations in load and velocities are shown. At each frequency, the frequency response set for the entire range of parametric uncertainties, say $P(s,\alpha)$ is called a template, where $\alpha = [D_{10}, D_{11}, D_{12}, D_{13}, D_{14}]$ represents uncertain parameters as shown in Figure 6.14. Plant templates are to be plotted for a selected range of frequencies on Nichols chart, which are used for computation of QFT bounds later (Figure 6.16).

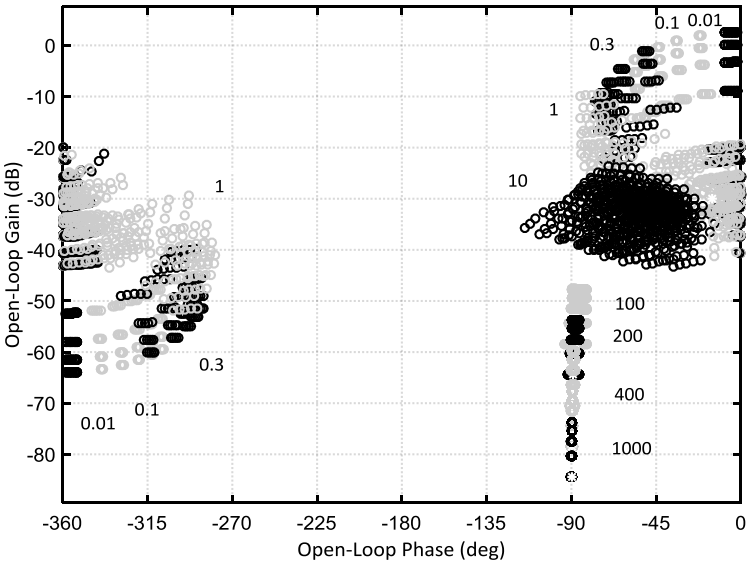

Figure 6.15 Plant templates at selected frequencies for configuration 1.

Next step is to choose performance specifications which should be met by closed-loop system. By using QFT technique we actually convert closed loop magnitude specifications into magnitude and phase constraints on nominal loop transfer function, C1(s) P(s,α), on Nichols chart. Two specifications used, are discussed below:

Robust stability specifications: The peak magnitude of closed loop frequency responses is constrained:

$$\left| \frac{C_1(j\omega)P(j\omega,\alpha)}{1+C_1(j\omega)P(j\omega,\alpha)} \right| \leq 1.6 \text{ where } \omega \in [0\ \infty] \tag{6.13}$$

Tracking specifications: The closed loop reference tracking performance is restricted using tracking criteria:

$$\text{T1 (j}\omega,\alpha) = \text{F1 (j}\omega) \frac{C_1(j\omega)P(j\omega,\alpha)}{1+C_1(j\omega)P(j\omega,\alpha)} \tag{6.14}$$

$$T_{L1}(j\omega) \leq \left| \frac{C_1(j\omega)P(j\omega,\alpha)}{1+C_1(j\omega)P(j\omega,\alpha)} \right| \leq T_{U1}(j\omega) \tag{6.15}$$

Where T_{L1} and T_{U1} are lower and upper bounds and are defined by designer. The upper bound has been constructed to have a maximum of 2% overshoot and 2% settling time of 0.737 sec. Lower bound has no overshoot and 2% settling time of 1.06 sec.

$$T_{L1}(s) = \frac{1}{1/30s^2+10.95/30s+1} \tag{6.16}$$

$$T_{U1}(s) = \frac{1}{(1/15s+1)(1/3s+1)(1/4s+1)(1/5s+1)(1/60s+1)(1/20000s+1)} \tag{6.17}$$

Step responses of T_{L1} and T_{U1} are plotted in Figure 6.15. After tracking and stability bounds are established, the resulting combined bounds at each selected frequency are plotted in Figure 6.16

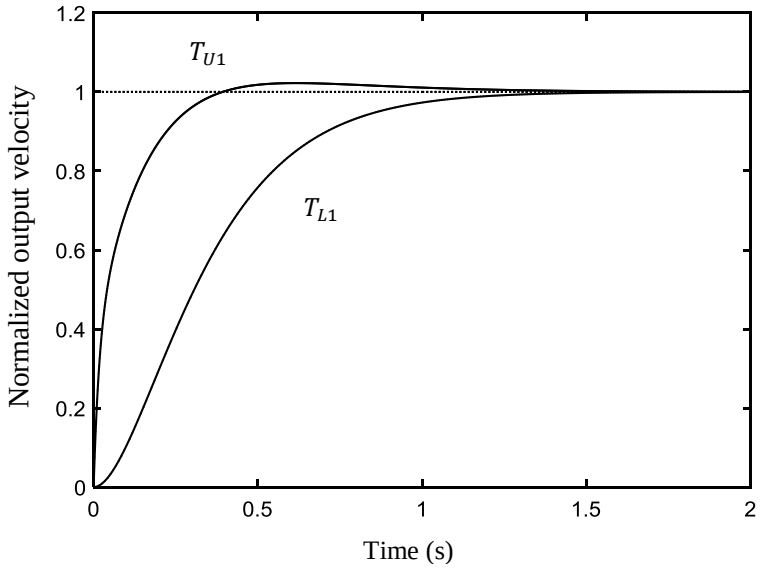

Figure 6.16 Time responses of tracking bounds.

Lastly, controller and prefilter is designed. A nominal plant $P(j\omega, \alpha_0)$, is chosen such that it satisfies the QFT bounds $B_1(\omega)$ at each frequency. The process of shaping the nominal loop transmission function $L_{10}(j\omega, \alpha_0) = C_1(j\omega)\, P(j\omega, \alpha_0)$ is done by adding zeros and poles to the controller, C_1 (s), is known as loop shaping, where a tradeoff between controller complexity and performance is achieved. It is shaped such that it lies on or above the corresponding open

bounds and it does not enter the closed bounds at each frequency. The uncompensated and compensated nominal loop transmission functions are shown in Figure 6.17 and 6.18. A prefilter is then designed to put the closed loop frequency responses in the desired tracking envelope (Figure 6.19 and 6.20). Controller and prefilter designed, are as:

$$C_1\,(s) = \frac{530467(1/19s+1)(1/2.967s+1)}{(1/414s+1)(1/0.0828s+1)} \tag{6.18}$$

$$F_1\,(s) = \frac{0.032019(s+128)(s+51.87)}{(s+5.324)(s+39.93)} \tag{6.19}$$

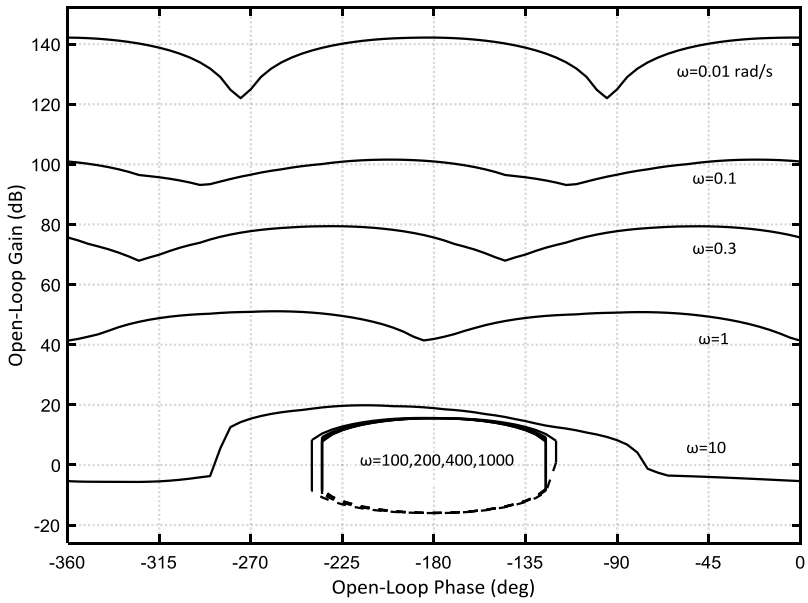

Figure 6.17 QFT combined bounds for selected design frequencies (rad/s).

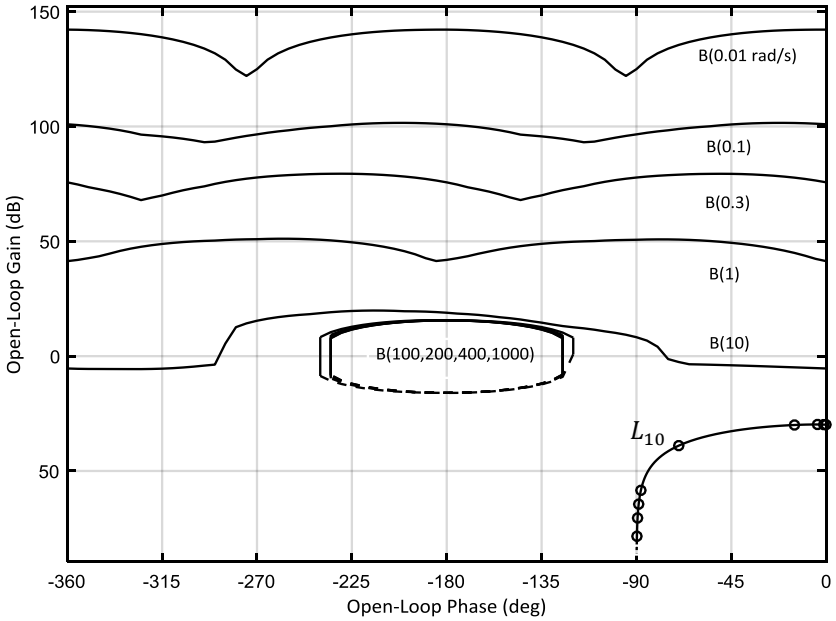

Figure 6.18 QFT bounds and nominal loop transmission function without controller.

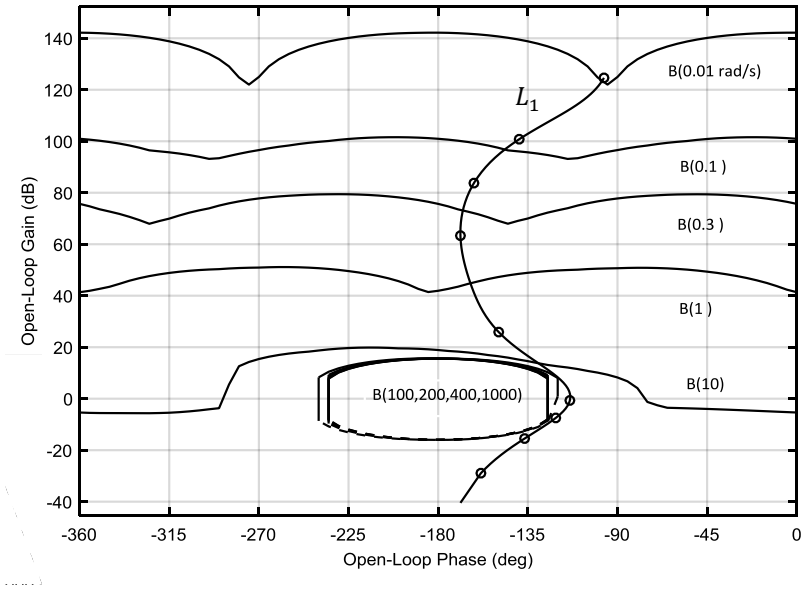

Figure 6.19 QFT bounds and nominal loop transmission function with QFT controller.

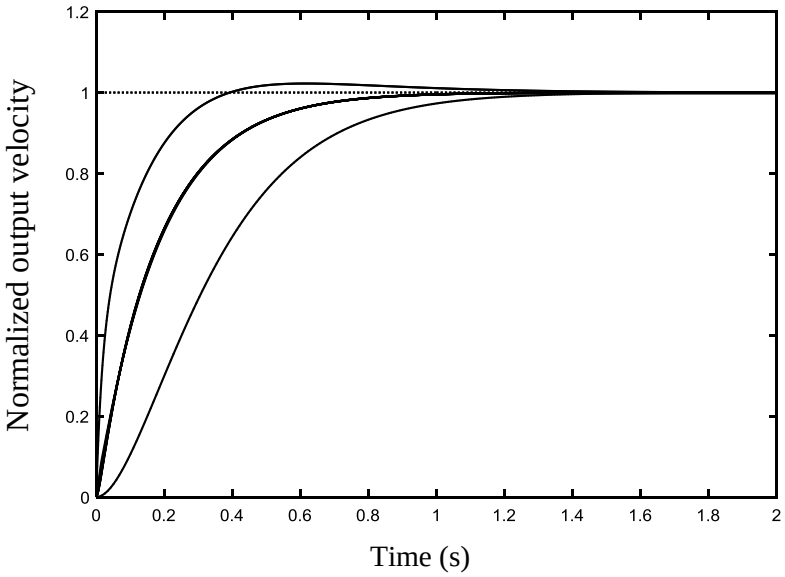

Figure 6.20 Step responses using QFT controller and prefilter for entire range of parametric uncertainties in case of configuration 1.

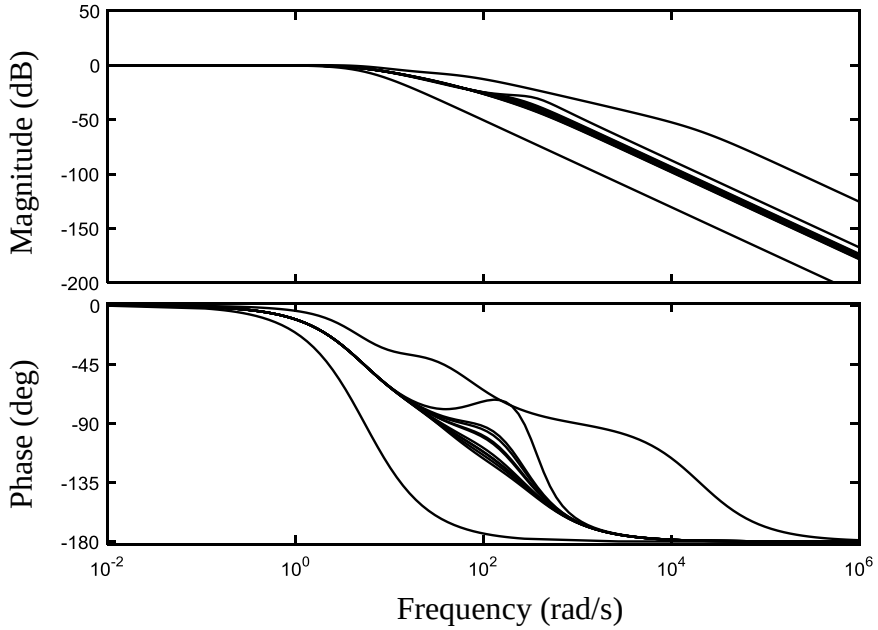

Figure 6.21 corresponding frequency responses of closed loop system using controller and prefilter for entire range of parametric uncertainties for configuration 1.

6.3. Simulation results

In case of configuration 1, simulation results show that at certain loads the configuration is controllable, though the problems arise at higher loads at this velocity. Closed loop performance for zero kg mass attached has been shown in Figure 6.21. For all loads tested, the performance has been shown in Figure 6.22, where problems due to switching of POCVs and opening of check valves are clearly seen. Figures 6.23 and 6.24 show closed loop system performance for higher velocity.

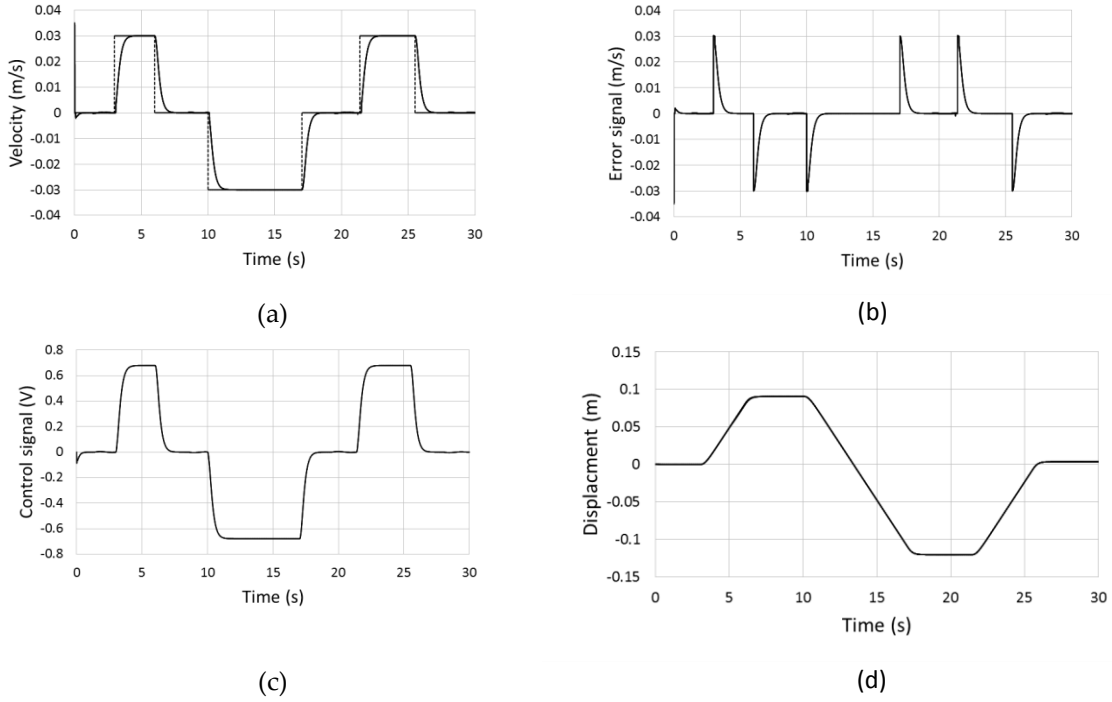

Figure 6.22 Closed loop simulation results for configuration 1 for zero kg mass attached, reference velocity of 0.03 m/s: (a) desired velocity (dotted) and actual response (solid) (m/s); (b) error signals (m/s); (c) control signals (V); (d) displacements of actuator (m).

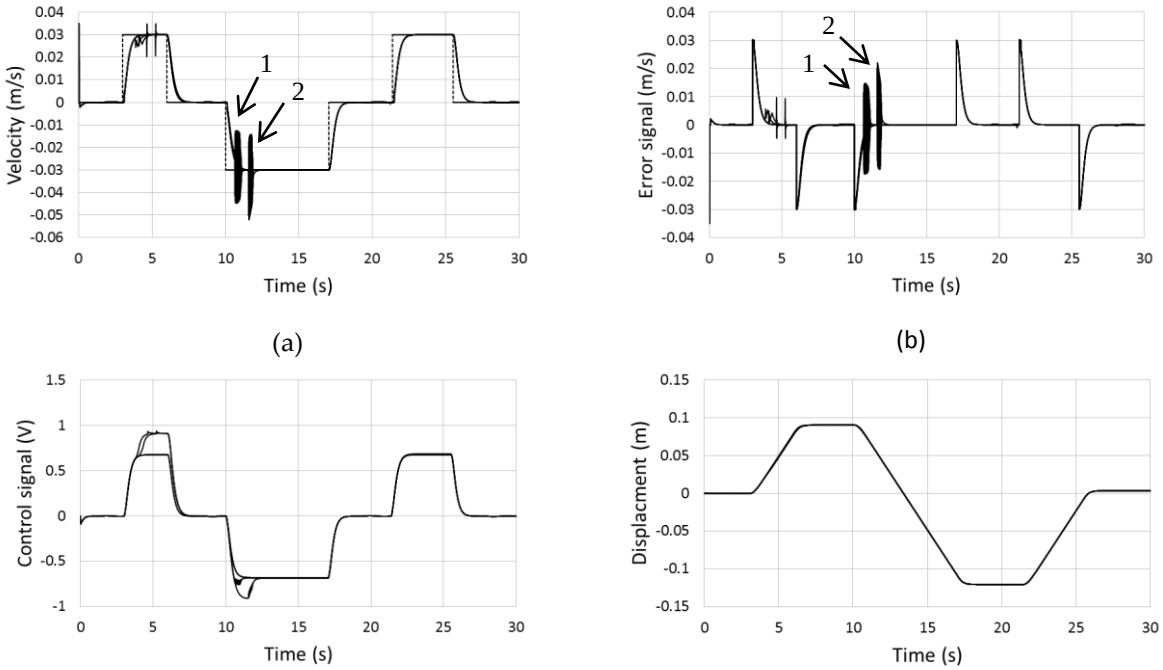

Figure 6.24 Closed loop simulation results for configuration 1 for zero kg, 41 kg, 122 kg, 245 kg, 368 kg mass attached, reference velocity of 0.03 m/s where regions 1 and 2 show undesirable velocity for loads 245 kg and 368 kg, respectively: (a) desired velocity (dotted) and actual response (solid) (m/s); (b) error signals (m/s); (c) control signals (V); (d) displacements of actuator (m).

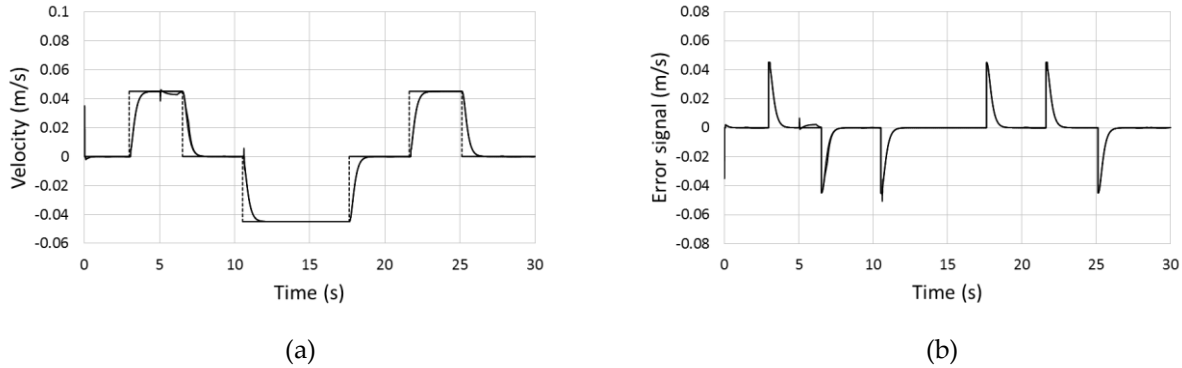

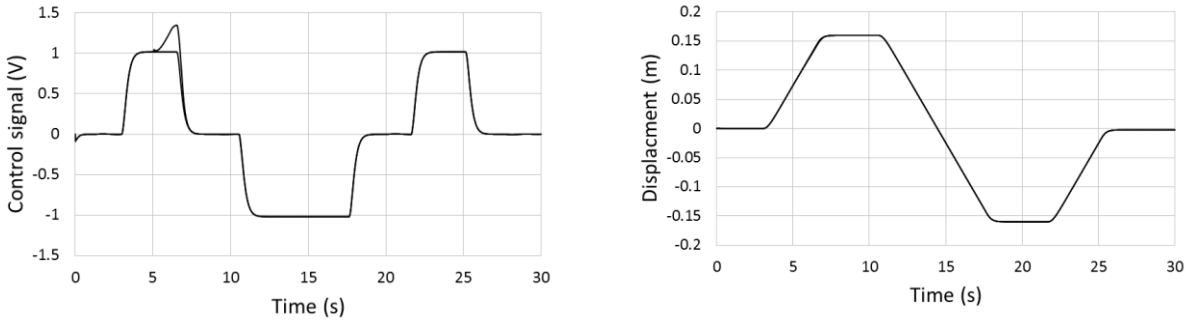

(c) (d)

Figure 6.25 Closed loop simulation results for configuration 1 for zero kg and 41 kg mass attached, reference velocity of 0.045 m/s: (a) desired velocity (dotted) and actual response (solid) (m/s); (b) error signals (m/s); (c) control signals (V); (d) displacements of actuator (m).

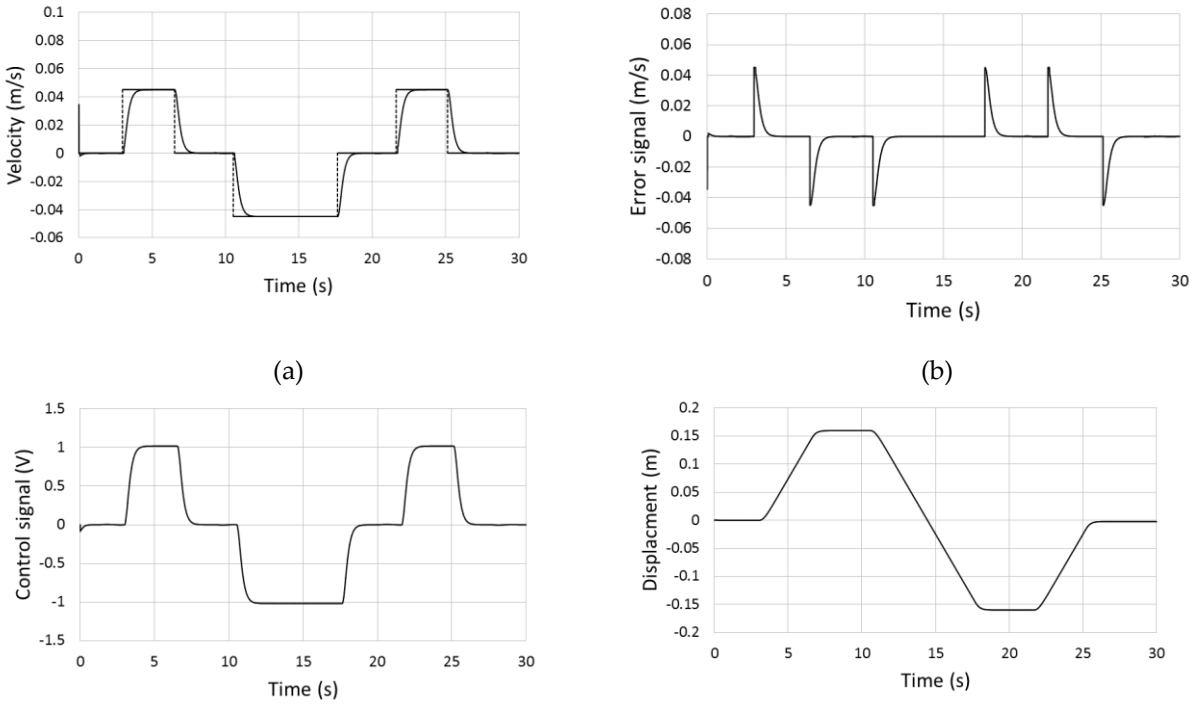

(a) (b)

(c) (d)

Figure 6.26 Closed loop simulation results for configuration 1 for 41 kg mass attached, reference velocity of 0.045 m/s: (a) desired velocity (dotted) and actual response (solid) (m/s); (b) error signal (m/s); (c) control signal (V); (d) displacement of actuator (m).

6.4. Experimental evaluation

Open loop experimental tests are followed by closed loop experiments for configuration 1. Open loop performance of configuration 1 is shown in Figure 6.25.

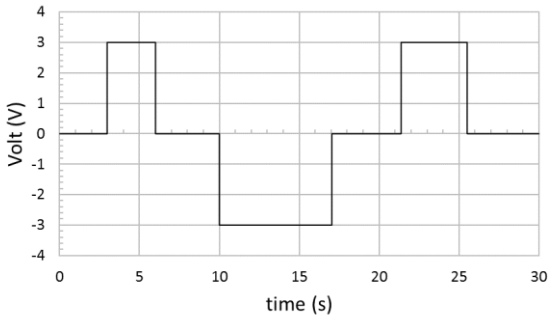

(a)

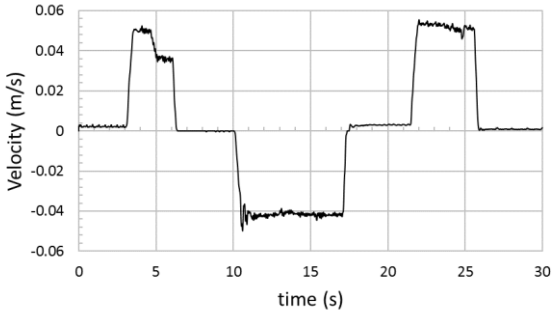

(b)

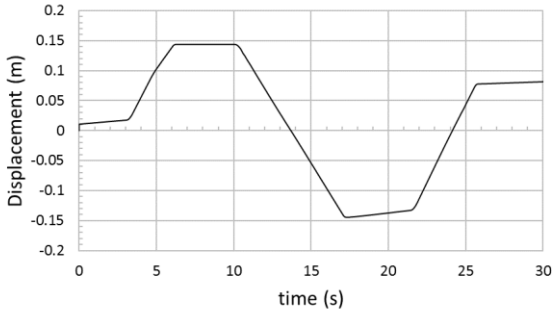

(c)

Figure 6.27 Experimental Open loop response of configuration 1 at Zero kg mass attached and 1.18 V: (a) input signal (V) including 1.82V for dead zone; (b) velocity of actuator (m/ s); (c) displacement of actuator (m).

At zero load and low velocity the bias force effect (due to charge pressure and area difference between two sides of single-rod actuator) can be seen in the beginning of motion at zero input which results in non-zero velocity. Vibrations in velocity while in retraction can be seen clearly in Figure 6.25[11].

While closing the loop(Figure 6.26), the controller is able to maintain zero velocity at zero input in presence of bias force, although we have a small constant control signal at beginning of

motion primarily due to opening of pilot operated check valves at zero load, bias force due to charge pressure and dominating friction. It should be noted that the controller is able to track the desired input and reach steady state values in both directions.

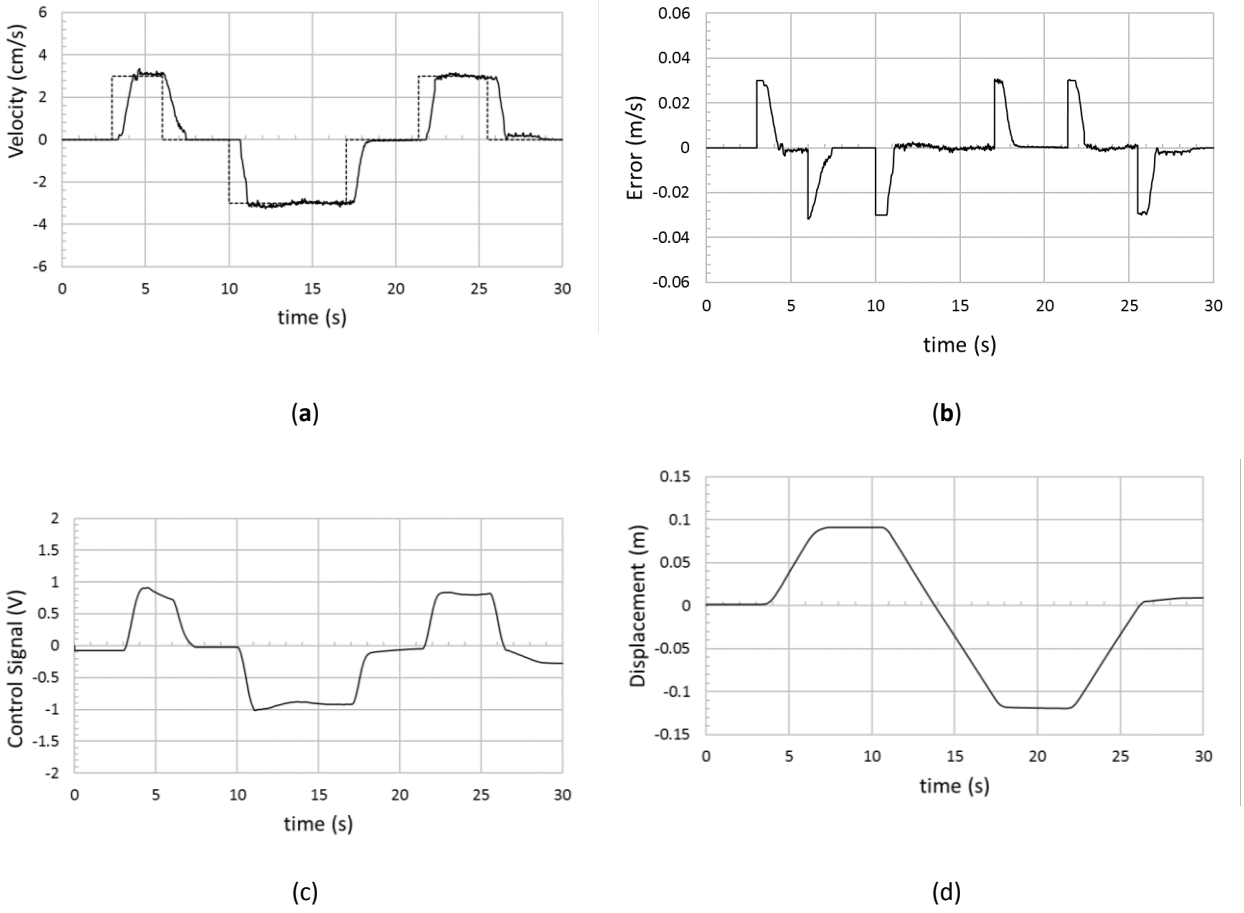

Figure 6.28 Experimental Closed loop response of configuration 1 with zero kg mass attached: (a) desired velocity (dotted) and actual response (solid) (m/s); (b) error (m/s); (c) control Signal (V); (d) displacement of actuator (m).

6.5. Design of QFT Controller for hydraulic circuit with configuration 2

For hydraulic circuit with configuration 2, P(s,β), C2(s) and F2(s) denote uncertain plant, controller and prefilter respectively. C2(s) and a prefilter F2(s) is designed in order to meet the performance criteria. At each frequency, the frequency response set for the entire range of parametric uncertainties, $P(s,\beta)$, is a template for configuration 2; template 02 includes

frequency response set for P(s,β) where β = $[f_{05}, f_{06}, f_{01}, f_{02}, f_{03}]$· for circuit configuration 2 (as α for configuration 1, table 6.1).

Q_a, Q_b, Q_A , Q_B , Q_1 and Q_2 represent flows at two pump ports, at two actuator ports and POCV valves respectively (fig 3.2). $\dot{p_A}$, $\dot{p_B}$, $\dot{p_a}$ and $\dot{p_b}$ represent pressure differentials on left and right side of actuator and pump ports respectively.

If states x_1 represents displacement, x_2 is velocity, x_3 is pressure on left port of actuator, x_4 is pressure on right port of actuator, x_5 is pressure on left port of pump, x_6 is pressure on right port of pump, and assuming $x_3 = x_5$ and using same procedure as in section 6.2 we get:

$$\frac{X_2(s)}{V_e(s)} = \frac{g_{06}}{g_{01}s^2 + g_{02}s + g_{03}} \tag{6.56}$$

where g_{06}, g_{01}, g_{02} and g_{03} are constants. Note that this equation represents a second order transfer function for configuration 2.

6.5.1 System identification for family of linear transfer functions

In order to get more accurate transfer function for circuit configuration 2, same input chirp excitation signals were used as in configuration 1. Figure 6.27 shows a symmetrical input chirp excitation signal with a maximum value of 2.68 V used. Displacement, velocity responses obtained for circuit configuration 2 are shown for 122 kg load attached.

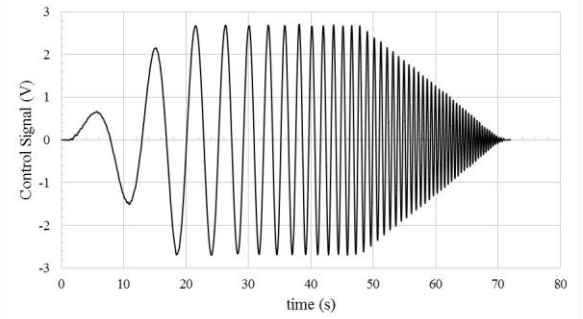

(a)

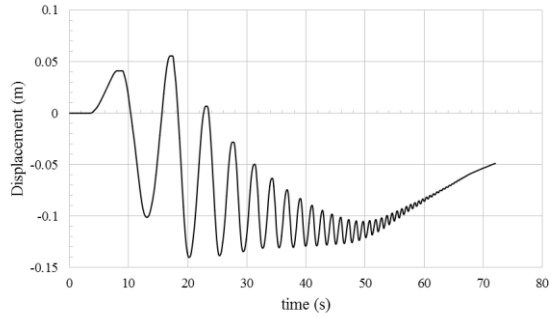

(b)

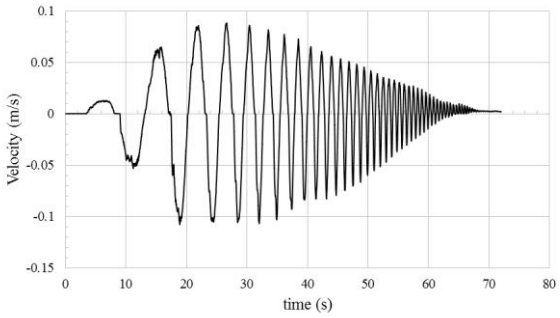

(c)

Figure 6.29 System response for input chirp excitation signal with a maximum of 2.68 V and 122 kg mass attached (configuration 2): (a) input chirp excitation signal with a maximum of 2.68 V; (b) displacement of actuator; (c) velocity of actuator.

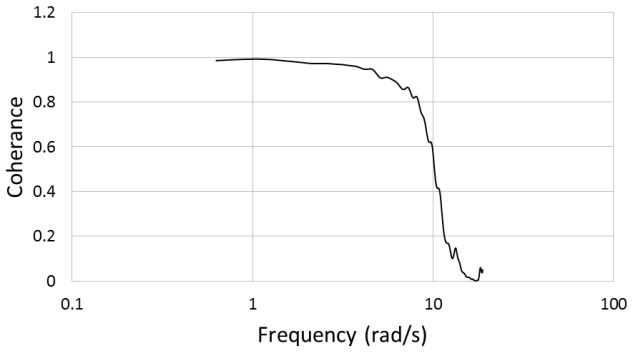

(a)

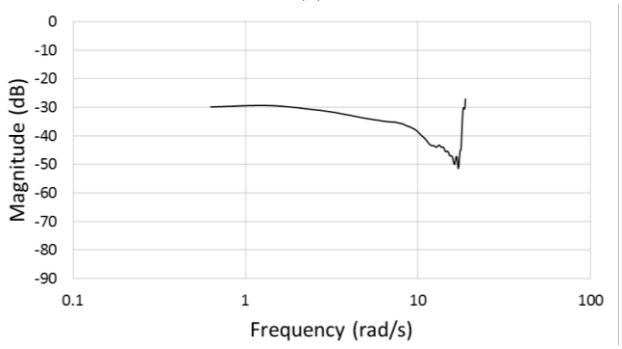

(b)

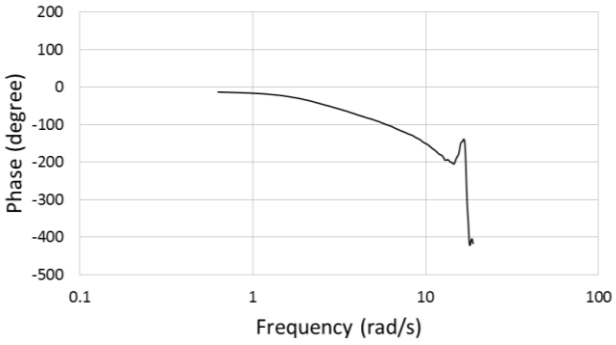

(c)

Figure 6.30 System identification results from CIFER for input chirp excitation signal with a maximum of 2.68 V and 122 kg mass attached (configuration 2): (a) coherence; (b) magnitude; (c) phase.

Figure 6.28 shows magnitude, phase and coherence obtained via system identification. In Figure 6.29 identified transfer function fitted with measured frequency response via CIFER for circuit configuration 2.

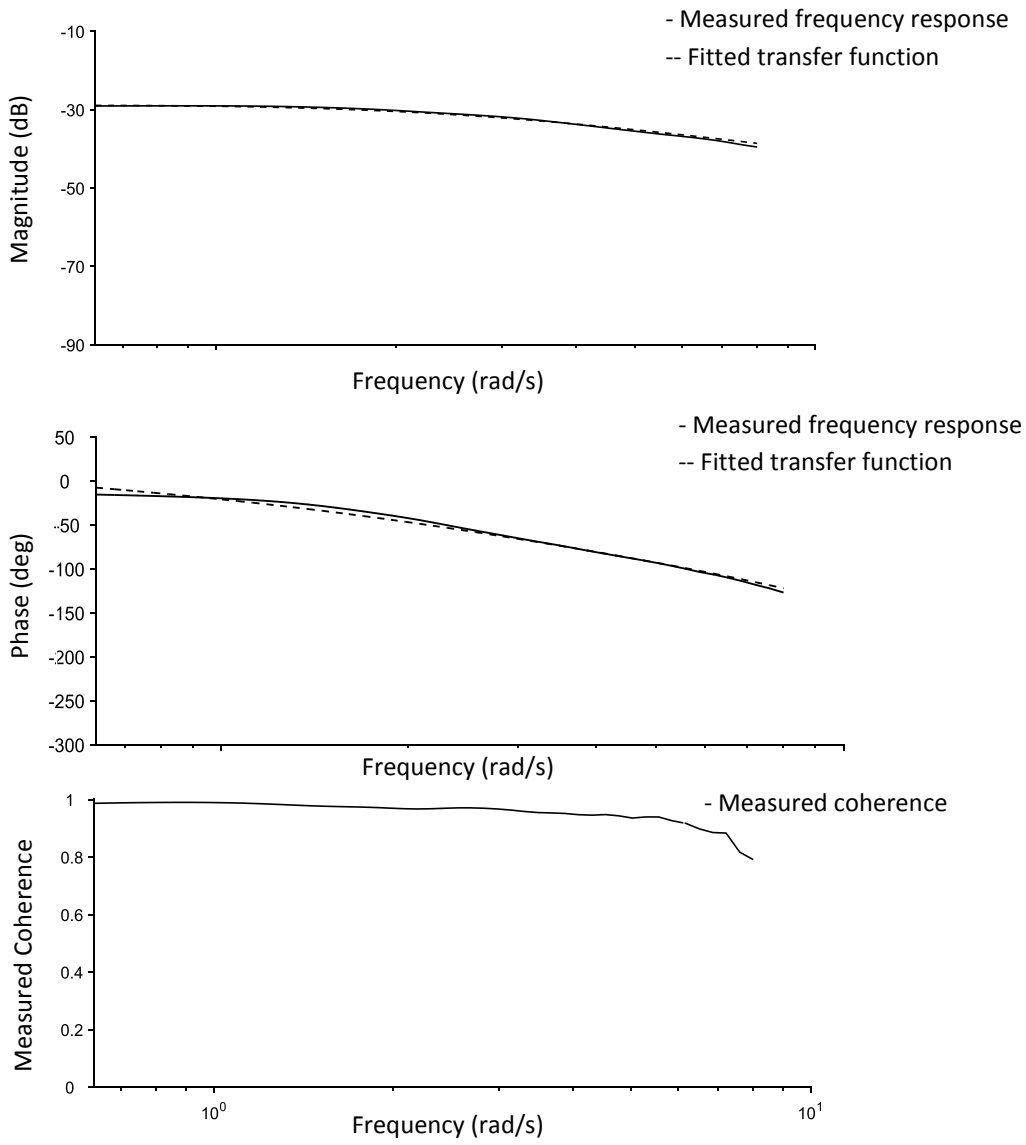

Figure 6.31 Comparison between experimental result and results obtained from system identification from CIFER for configuration 2: (a) magnitude; (b) phase; (c) measured coherence.

In Figure 6.30, at zero load and low velocity, the actuator moves towards retraction gradually, as retracting velocity is greater than extension in case of single-rod cylinders when no bias force effect (due to charge presure)is seen due to resistance added by incorporation of counter balance

valves in configuration. At high frequency and nearly zero velocity the system is seen slightly moving towards initial position from retracted state, due to its own weight.

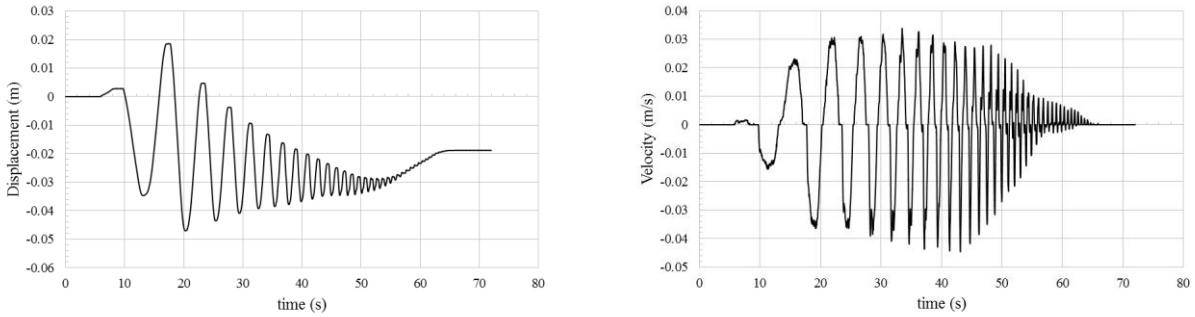

(a) (b)

Figure 6.32 Input chirp excitation signal with a maximum of 1.18 V and zero mass attached (configuration 2):(a) displacement of actuator; (b) velocity of actuator.

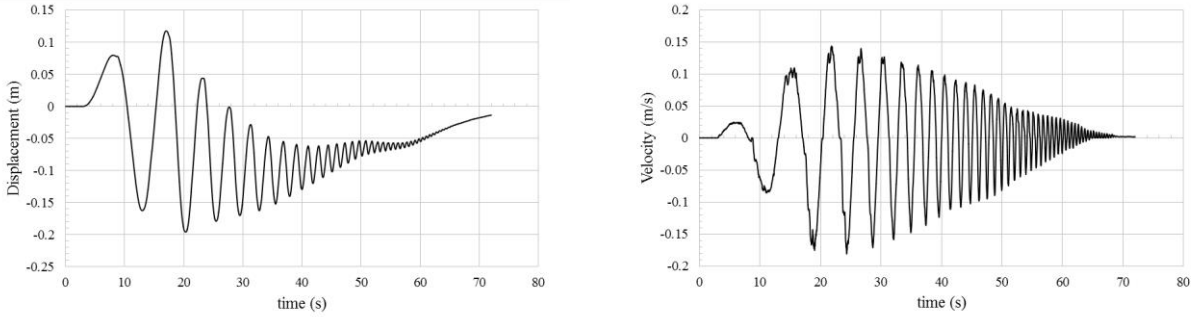

(a) (b)

Figure 6.33Input chirp excitation signal with a maximum of 4.18 V and 245 kg mass attached (configuration 2):(a) displacement of actuator; (b) velocity of actuator.

Figure 31 shows system response for 245 kg load and high velocity. With increase in frequency and time, actuator displacement shows similar behaviour (as Figure 6.30 at low velocity and zero load), although at low frequency actuator displacement is relatively symmetrical. This can be seen in velocity responses as well.

Magnitude, phase and coherance results obtained for configuration 2 at various loads and velocities are shown in Figure 6.32.

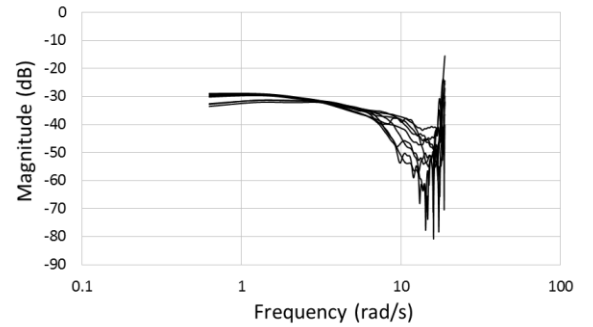

(a)

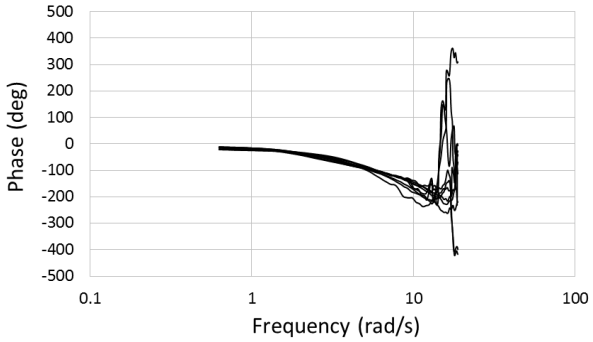

(b)

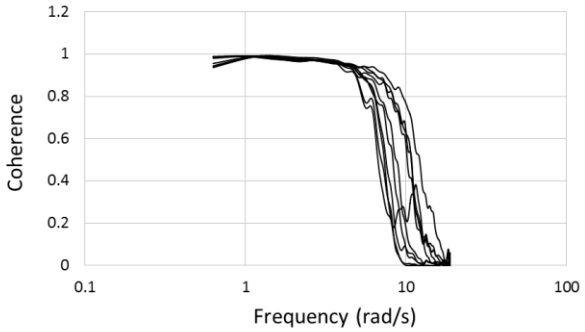

(c)

Figure 6.34Results from CIFER system identification (configuration 2) at different loads and velocities: (a) magnitude; (b) phase; (c) coherence.

The identified model parameters denoting a family of trasfer functions for circuit confugration 2 are shown in table 6.2. This constitutes the best fitted transfer function obtained from CIFER by

taking uncertainties at various loads and velocities into account, in case of configuration 2 for transfer function (TF2) used:

$$\frac{X_2(s)}{V_e(s)} = \frac{f_{05}s + f_{06}}{f_{01}s^2 + f_{02}s + f_{03}} \tag{6.64}$$

where f_{05}, f_{06}, f_{01}, f_{02} and f_{03} are constants obtained via system identification

Table 6.2. Range of parameters of transfer function of configuration 2 (TF2) for external mass attached 0 kg, 122 kg, 245 kg, 368 kg and voltage input signals of 1.18 V, 2.68 V and 4.18 V

f_{05}	f_{06}	f_{01}	f_{02}	f_{01}
0.010828-0.137649	**0.070368-0.873781**	**1**	**3.73427-8.48604**	**2.46266-32.9731**

Note that fourth type of chirp signal i.e. asymmetric type was also tested in configuration 2. Uncertainties were found to be within the above uncertainty range; hence confirming CIFER results do not depend much on type of chirp signal (symmetric or unsymmetrical) in this case.Based on these uncertainties, a QFT controller for configuration 2 is designed.

6.5.2 Verification of results

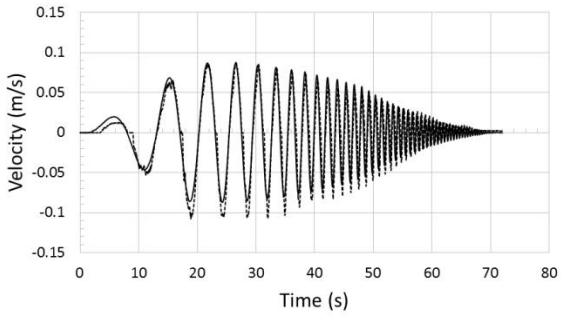

Figure 6.35 Experimental (dotted) and simulation (solid) results (configuration 2).

A family of transfer functions is obtained for configuration 2(uncertainities for configuration 2 are listed in table 6.2) using system identification and verified by comparing the results (Figure 6.33) with experiment tests(as done in case of configuration 1).

6.5.3 Family of transfer functions

Three square input signals (1.18 V, 2.68 V and 4.18 V) were tested (same as in case of circuit configuration 1) on family of transfer functions obtained in order to test open loop performances of configuration 2. Results are shown in Figures 6.34-6.36.

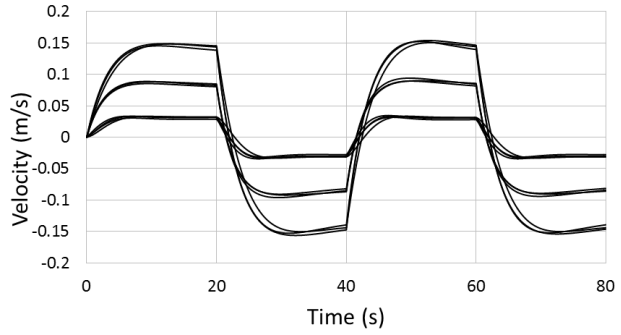

Figure 6.36 Open loop response for family of transfer functions obtained from cifer (configuration 2).

6.5.4 Bode plots and step response

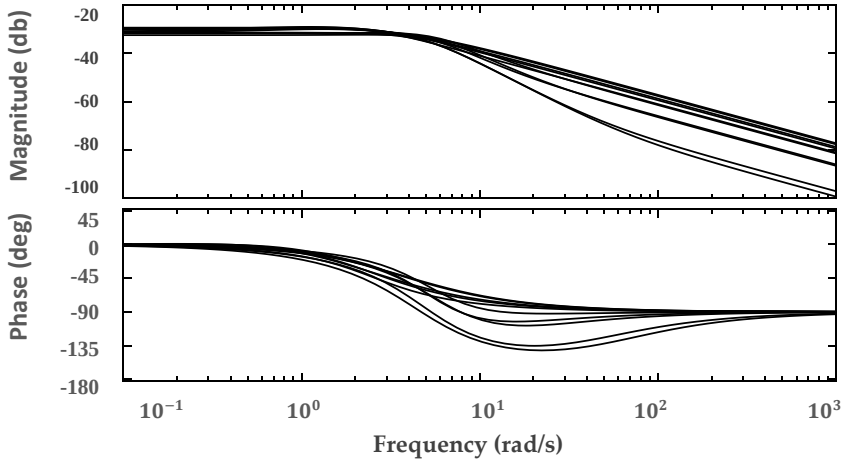

Figure 6.37 Frequency responses of uncertain plant considering variable velocity and uncertain load variations (configuration 2).

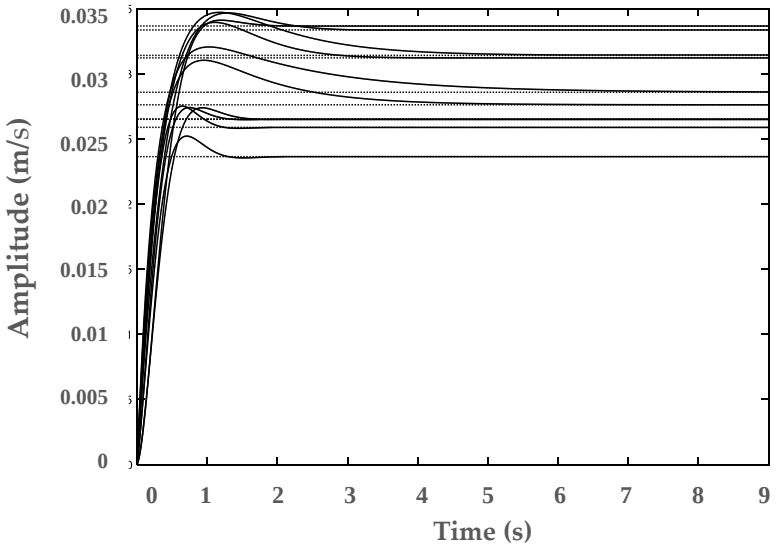

Figure 6.38 Open loop step response for uncertain plant (configuration 2).

6.5.5 Controller Design 2

A controller is designed for configuration 2 using same QFT technique. P2(s, β), C2(s) and F2(s) denote uncertain plant, controller and prefilter respectively in case of configuration 2(Figure 6.37). The system was excited in a similar way as in configuration 1, using different chirp inputs at different loads.

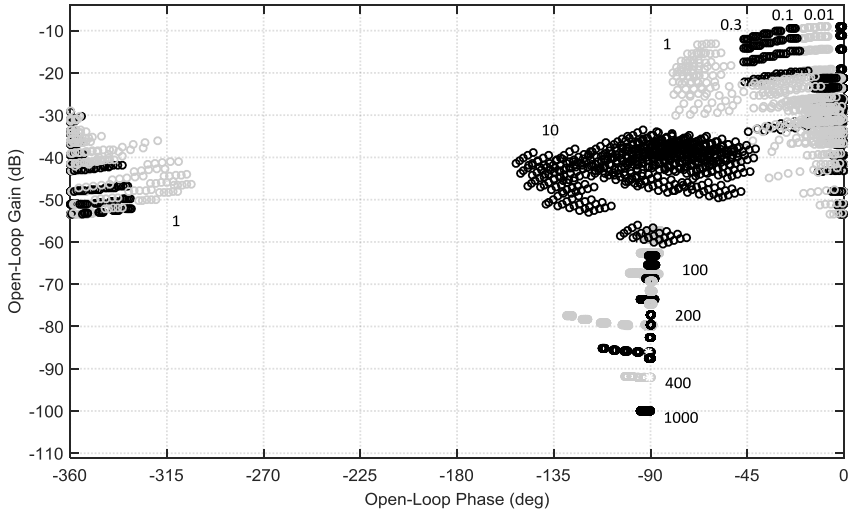

Figure 6.39 Plant templates at selected frequenciesr (configuration 2).

The parameter ranges of transfer function 02 considering different loads and velocities are shown in table 6.2 At each frequency, the frequency response set for the entire range of parametric uncertainties in configuration 2(template), say $P(s,\beta)$ where β represents set of uncertain parameters (as discussed in previous section 6.5) is shown in Figure 6.37. Two specifications for configuration 2 are discussed below:

Robust stability specifications: The peak magnitude of closed loop frequency responses is constrained:

$$\left| \frac{C_2(j\omega)P(j\omega,\beta)}{1+C_2(j\omega)P(j\omega,\beta)} \right| \leq 1.6 \text{ where } \omega \in [0\ \infty] \quad (6.65)$$

Tracking specifications: The closed loop reference tracking performance is restricted using tracking criteria:

$$T2\ (j\omega,\beta) = F2\ (j\omega)\frac{C_2(j\omega)P(j\omega,\beta)}{1+C_2(j\omega)P(j\omega,\beta)} \qquad (6.66)$$

$$T_{L2}(j\omega) \leq \left|\frac{C_2(j\omega)P(j\omega,\beta)}{1+C_2(j\omega)P(j\omega,\beta)}\right| \leq T_{U2}(j\omega) \qquad (6.67)$$

Where T_{L2} and T_{U2} are lower and upper bounds and are defined by designer. The upper bound has been constructed to have a maximum of 2% overshoot and 2% settling time of 0.737 sec. Lower bound has no overshoot and 2% settling time of 1.06 sec.

$$T_{L2}(s) = \frac{1}{1/30s^2+10.95/30s+1} \qquad (6.68)$$

$$T_{U2}(s) = \frac{1}{(1/15s+1)(1/3s+1)(1/4s+1)(1/5s+1)(1/60s+1)(1/20000s+1)} \qquad (6.69)$$

Step responses of T_{L2} and T_{U2} are plotted in Figure 6.38. The resulting combined bounds at each selected frequency are plotted in Figure 6.39.

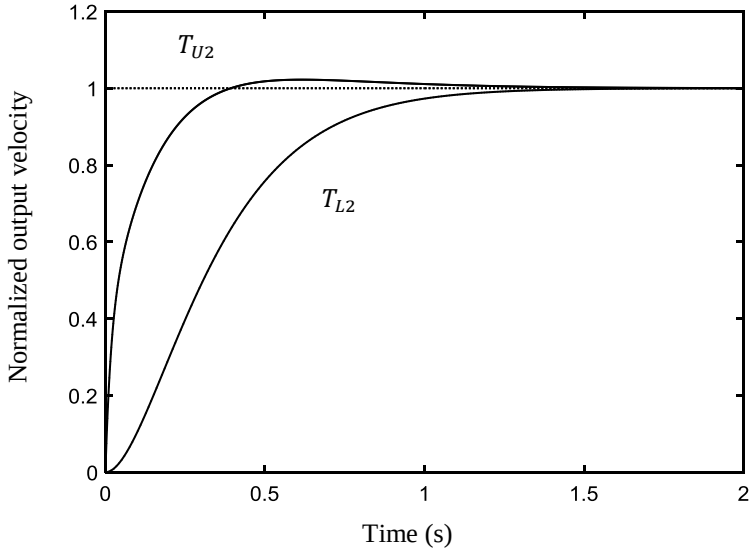

Figure 6.40 Time responses of tracking bounds (configuration 2).

Lastly, controller and prefilter is designed for configuration 2. A nominal plant $P_2(j\omega,\beta_0)$, is chosen such that it satisfies the QFT bounds $B_2(\omega\ )$ at each frequency. The process of shaping

the nominal loop transfer function L_{20} (jω, β_0) = $C_2(j\omega)$ $P(j\omega, \beta_0)$ is done for $C_2(j\omega)$as was done in case of $C_1(j\omega)$. The uncompensated and compensated nominal loop transmission functions are shown in Figure 6.40 and 6.41 respectively. A prefilter $F_2(s)$ is then designed to put the closed loop frequency responses in the desired tracking envelope using bode plots (Figure 6.42 and 6.43). In Figure 6.43 some frequency responses may seem as not meeting the specifications, but it should be noted that maximum frequency of interest is 7.5 rad/s only. The controller and prefilter designed are as:

$$C_2\ (s) = \frac{50528(1/23.66s+1)(1/8.6s+1)}{(1/1944s+1)(1/44.72s+1)} \tag{6.70}$$

$$F_2\ (s) = \frac{0.047594(s+44.66)(s+47.82)}{(s+7.495)(s+13.56)} \tag{6.71}$$

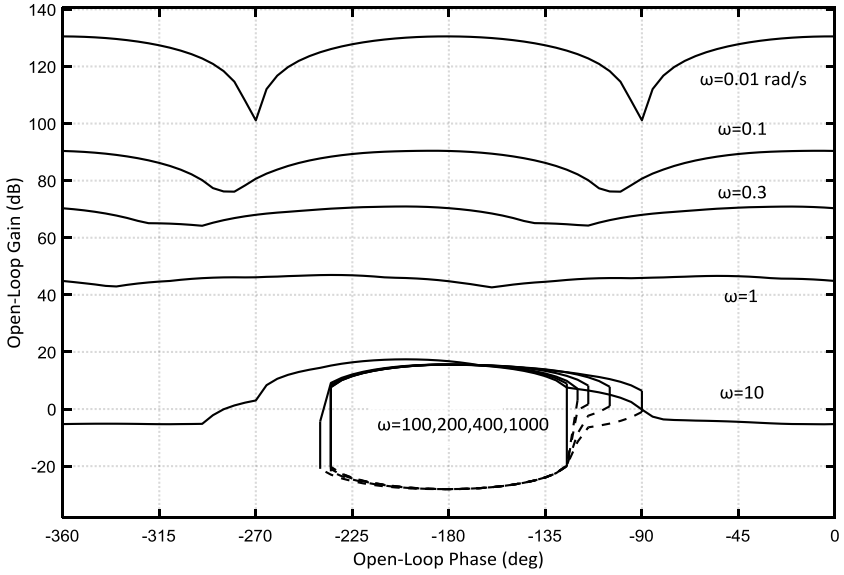

Figure 6.41 QFT combined bounds for selected design frequencies (rad/s) (configuration 2).

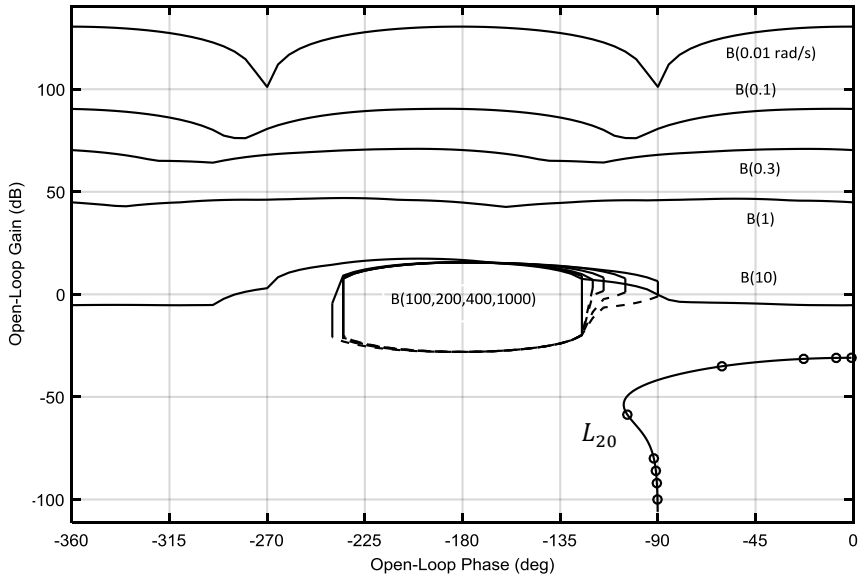

Figure 6.42 QFT bounds and nominal loop transmission function without controller (configuration 2).

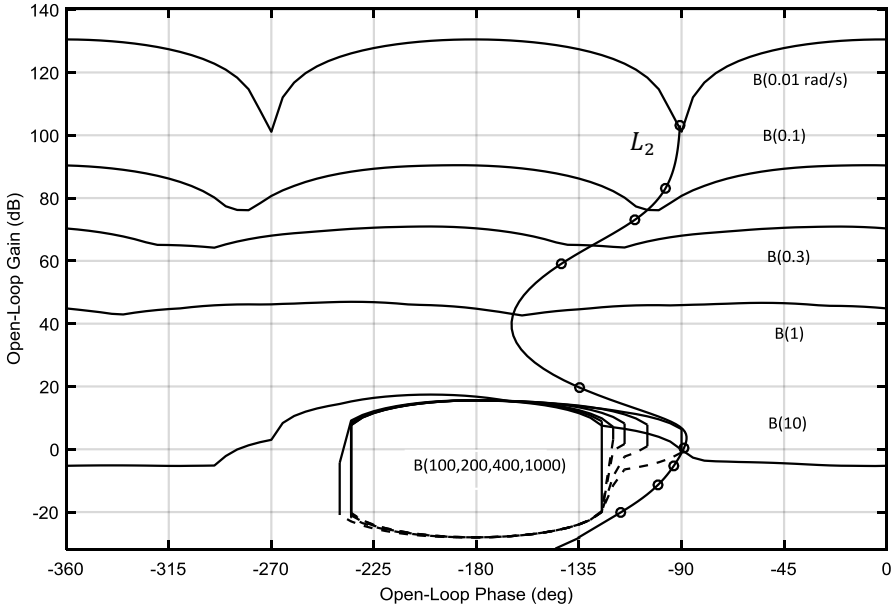

Figure 6.43 QFT bounds and nominal loop transmission function with QFT controller (configuration 2).

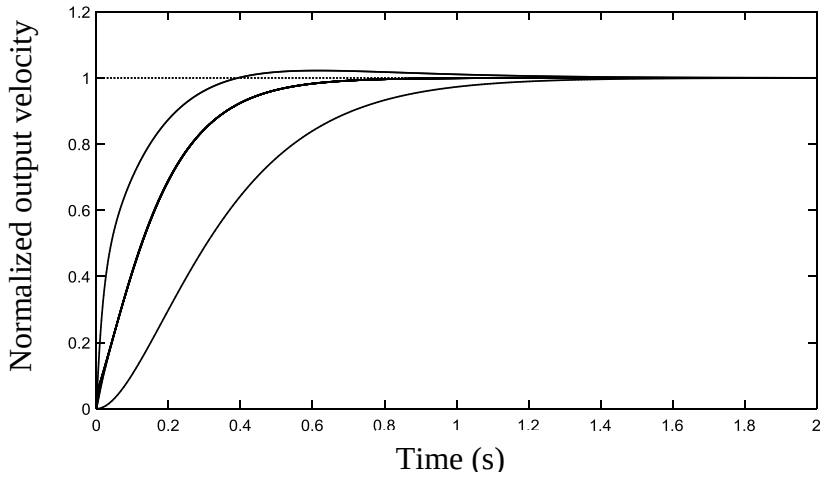

Figure 6.44 Step responses using QFT controller and prefilter for entire range of parametric uncertainties (configuration 2).

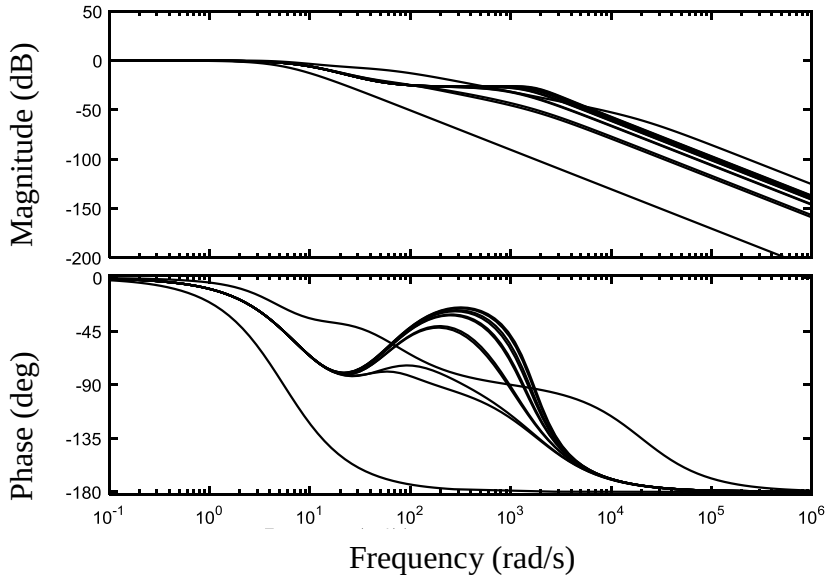

Figure 6.45 corresponding frequency responses of closed loop system using controller and prefilter for entire range of parametric uncertainties (configuration 2).

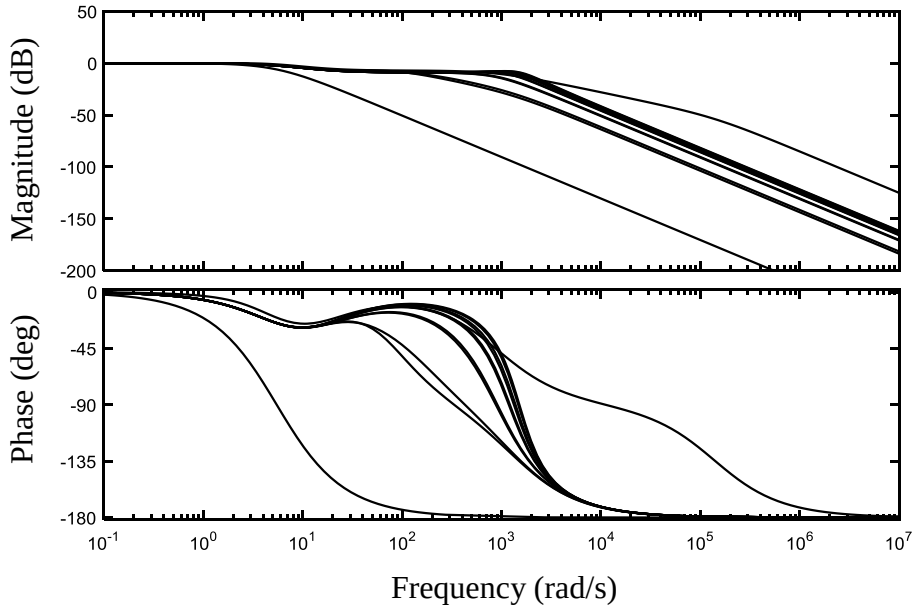

Figure 6.47 corresponding frequency responses of closed loop system using second set of controller and prefilter for entire range of parametric uncertainties (configuration 2).

In Figure 6.44 all frequency responses are within specifications, although a different controller and prefilter is used for this (and as such was not used in this research).

6.6. Simulation results:

For configuration 2, simulation results have been shown in Figure 6.45 for different loads tested. Controller is able to track the reference input in both extension and retraction. Design specifications are met in retraction, but for extension settling time is higher. This can be attributed to the difference in velocities of two sides in case of single-rod cylinders and incorporation of counterbalance valves in the circuit configuration which act as resistance. Furthermore, since a single transfer function is used to represent the system the controller performs better on one side than the other.

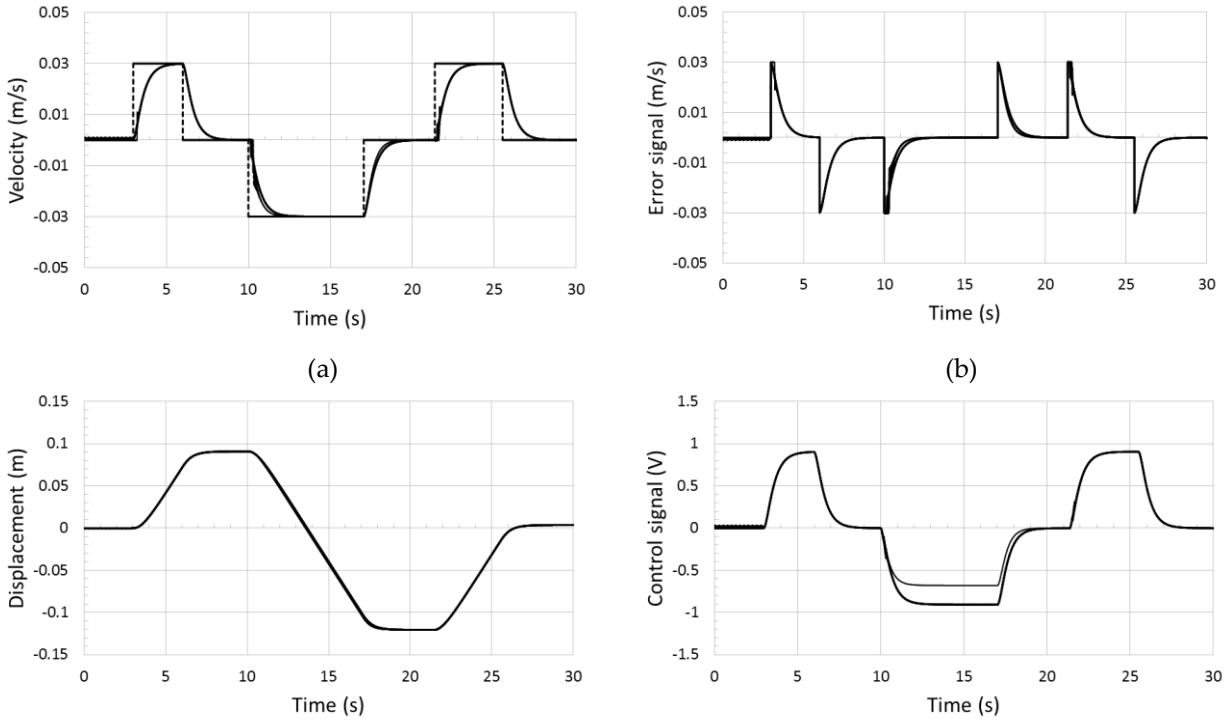

(a) (b)

(c) (d)

Figure 6.48 Closed loop simulation results for configuration 2 for loads zero kg, 41 kg,122 kg, 245 kg,368 kg mass attached, reference velocity of 0.03 m/s: (a) desired velocity (dotted) and actual response (solid) (m/s); (b) error signal (m/s); (c) control signal (V); (d) displacement of actuator (m).

Figure 6.46 shows closed loop simulation results for higher velocity and all tested loads.

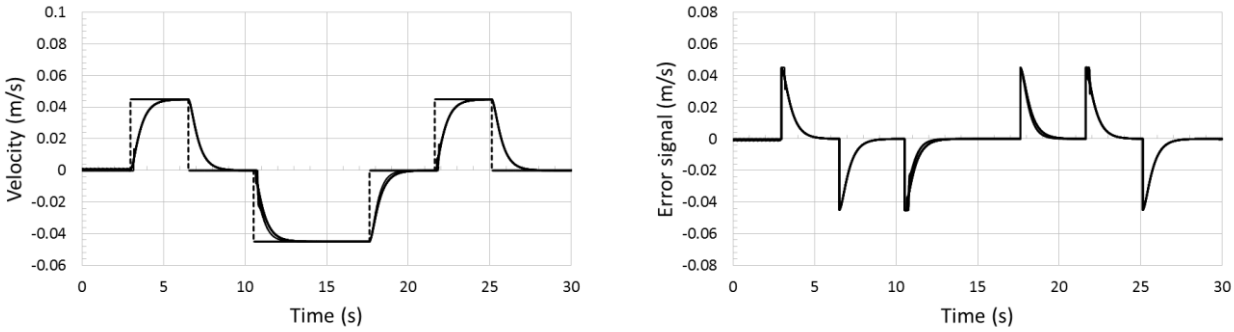

(a) (b)

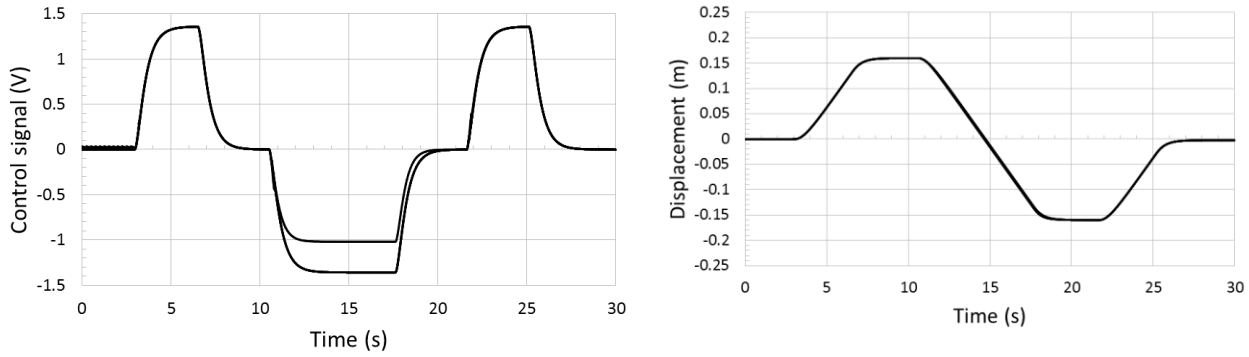

(c) (d)

Figure 6.49 Closed loop simulation results for configuration 2 for loads zero kg, 41 kg,122 kg, 245 kg,368 kg mass attached, reference velocity of 0.045 m/s: (a) desired velocity (dotted) and actual response (solid) (m/s); (b) error signal (m/s); (c) control signal (V); (d) displacement of actuator (m).

6.7. Experimental evaluation:

An open loop experimental response is shown in Figure 6.47 below. Bias force does not dominate at initial zero velocity and zero input (upto 3 second) as compared to configuration 1, due to the resistance created by incorporation of counterbalance valves in configuration 2.

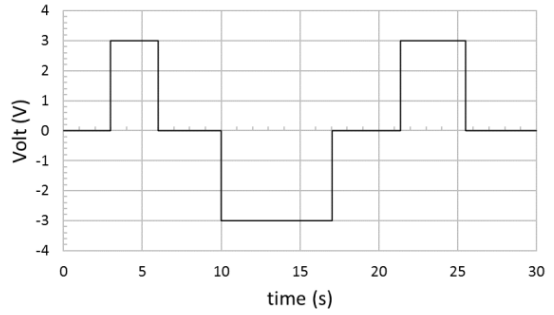

(a)

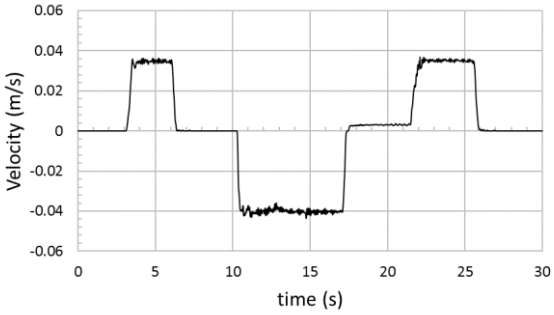

(b)

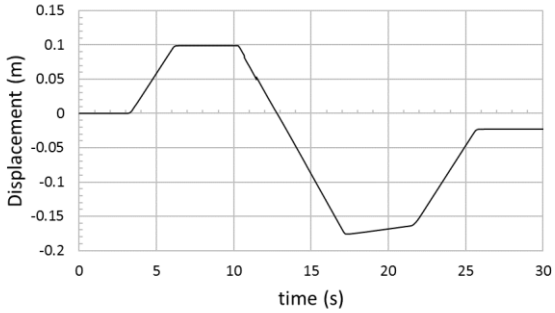

(c)

Figure 6.50 . Experimental Open loop response of configuration 2 with 1.18 V(excluding dead zone) and Zero kg mass attached: (a) input signal(V) including 1.82 dead zone; (b) velocity of actuator(m/ s); (c) displacement of actuator (m).

Figure 6.48 shows open loop response of configuration 2 at 41 kg mass and 1.18 V input signal.

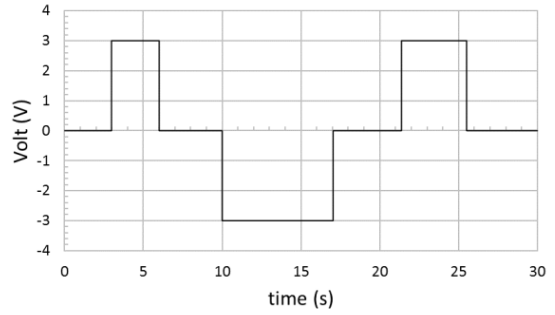

(a)

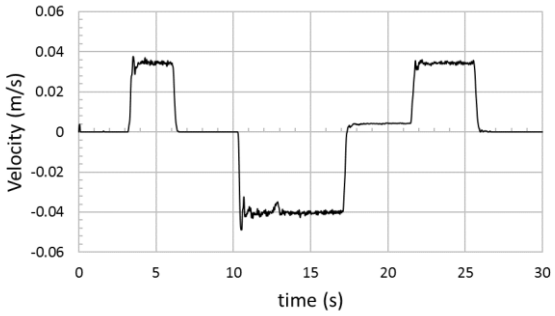

(b)

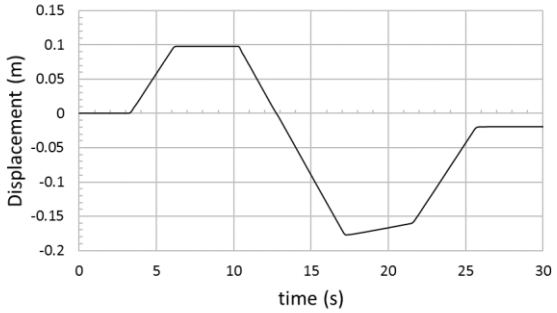

(c)

Figure 6.51 Experimental Open loop response of configuration 2 at 41 kg mass attached and 1.18 V: (a) input signal (V) including 1.82 dead zone; (b) velocity of actuator(m/ s); (c) displacement of actuator (m).

The closed loop response for configuration 2 for zero kg and 41 kg mass attached is shown in Figure 6.49 and 6.50 respectively. The controller performs well in retraction but is slower in case of extension, as was seen in case of simulation.

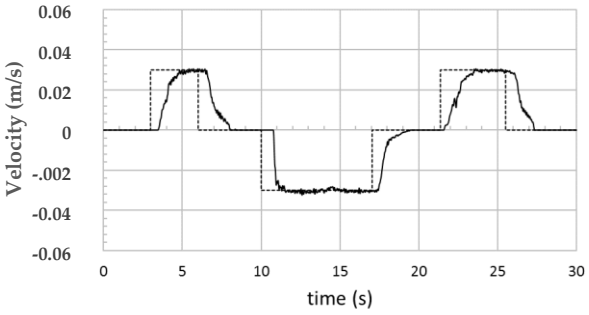

(a)

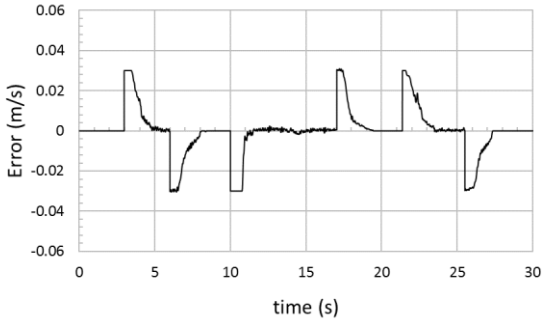

(b)

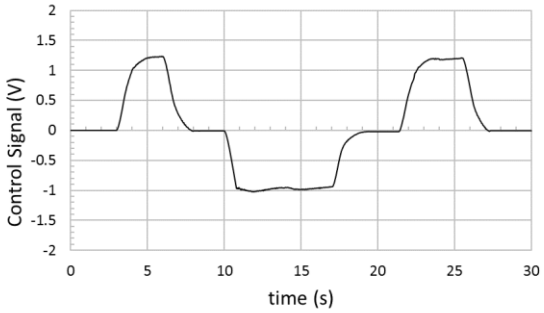

(c)

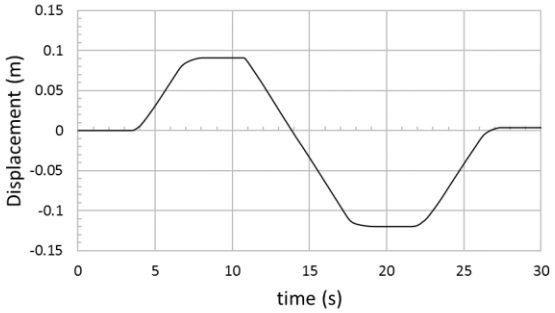

(d)

Figure 6.52 Experimental Closed loop response of configuration 2 at Zero kg mass attached: (a) desired velocity (dotted) and actual response (solid) (m/s); (b) error (m/s); (c) control Signal (V); (d) displacement of actuator (m).

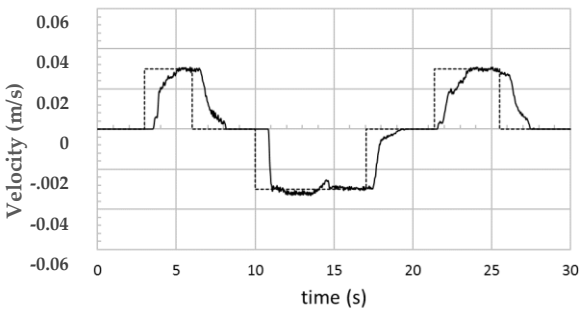

(a)

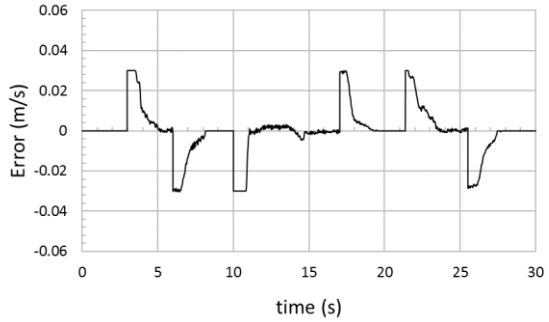

(b)

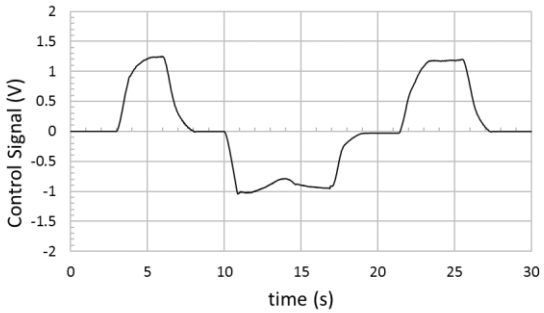

(c)

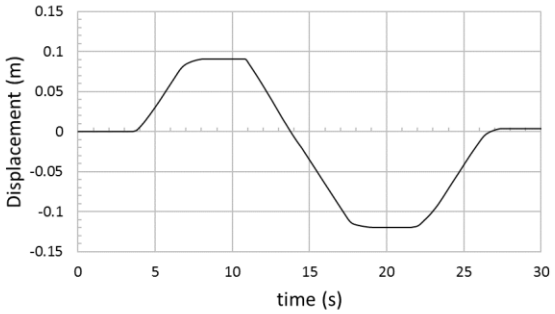

(d)

Figure 6.53 Experimental Closed loop response of configuration 2 at 41 kg mass attached: (a) desired velocity (dotted) and actual response (solid) (m/s); (b) error (m/s); (c) control Signal (V); (d) displacement of actuator (m).

6.8. Summary

In chapter 06 linearized models of configuration 1 and configuration 2 are obtained in order to deduce transfer functions for two configurations. System identification technique CIFER is used where frequency sweep signals are given as inputs to the system tested at various loads. Results in case of configuration 1 show that system has a tendency to move towards extension when input chirp excitation signals are used (although retraction is supposed to be quicker; a single-rod system) especially at low loads or low velocities. This is because resulting bias force dominates the configuration and pushes actuator towards extension. This effect can be seen clearly at beginning of motion and at high frequencies tested. In case of configuration 2 results show that system has a tendency to move towards retraction (which is expected in a single-rod system due to difference in area, charge pressure and quick retraction), hence showing that bias force does not dominate configuration 2. But the resistance added in the configuration due to incorporation of counter balance valves affects the performance at the beginning of motion and at high frequencies tested. At high loads inertia affects the performance of the system. A family of transfer functions is obtained (discussed in next chapter) where results are verified with experimental tests (using same input excitation signals). Time and frequency responses of family of transfer functions obtained are shown.

Measured and fitted transfer functions for two configurations are also compared. System identification technique incorporates the effects of variations in load and velocity in the transfer functions, derived. Vectors representing uncertain parameters in plant for each hydraulic configuration are defined. Controller design for both configurations is discussed. Closed loop simulation results are shown for various loads and velocities. In case of configuration 1, at low loads and low velocities controller is able to track the desired input signal within design specifications, while as at higher loads and velocities, performance is affected by overlapping of areas of pilot operated check valves. Experimental closed loop results are also shown. In case of configuration 2, simulation results show that controller is able to track desired input signal all loads and velocities. All design specifications are met in retraction, while as settling time for

extension is higher. This is supported by experimental results as well. Closed loop responses for optimized hydraulic configuration configurations are also shown.

Chapter 7

Conclusions

7.1. Contributions made in this thesis

In this thesis closed-loop velocity control of variable displacement pump-controlled hydraulic circuits for two configurations was presented. Two hydraulic configurations of interest were discussed where one circuit used pilot operated check valves (commonly used) while the other used counterbalance valves (new design).The contributions made in this work are as follows:

1. A methodology for optimal hydraulic component selection (optimal component sizing) which helps to choose an optimal hydraulic circuit design was proposed. It involved optimization of parameters of hydraulic components in open loop and hence improved performance of pump-controlled single-rod systems, based on simulation models and experimental data at different loads and velocities. The results obtained after optimization showed that in both configurations the performance of system was improved. In configuration 1, the undesirable velocity regions were not seen when 10 parameter optimization was used. Simulations were supported by experiments.
2. Experiment-based novel system identification approach applied and validated on two distinct hydraulic configurations at different loads and velocities using special input chirp excitation signals was presented. Uncertainties found were used to make velocity controllers for two circuits.
3. Simple-to-implement velocity controllers were designed based on Quantitative Feedback Theory (QFT) design technique by taking variations in load and velocity into account. Parametric uncertainties obtained from system identification were included in the design of

controllers. Simulation results for configuration 1 showed that the designed controller can track the desired reference signal within design specifications, but the closed loop performance was affected by undesirable velocity regions due to dominating nature of charge pressure and friction. Simulation and experimental results for configuration 2 showed that designed controller was able to track desired reference signals. Controller designed was also tested on optimized hydraulic circuit configuration.

On the basis of analysis done and results obtained; some research questions are answered as:

1. In order to design a simple-to-implement velocity controller, where variations in load, velocity and circuit design are taken into account, the proposed methodology for optimal component selection is to be followed. Then experiment-based novel system identification approach is used to find a family of transfer functions (based on uncertainties found). This is followed by validation of results.
2. In order to choose an optimal hydraulic component for a given hydraulic configuration optimal sizing of hydraulic components is important. Starting with mathematical model, initial component selection involves choosing certain parameters which need to be further optimized. Next an optimization criterion is proposed which is then followed by verification.
3. In system identification a frequency sweep signal is given as input to the system. System uncertainties for different loads, velocities and circuit designs are obtained. Comprehensive identification from frequency responses helps us to distinguish and control each hydraulic circuit better.
4. Undesirable performance in certain regions of operation was no longer seen as a result of optimization. Circuit configuration 1 performs better after optimization (no undesirable velocity regions) and hence optimization is recommended. But for configuration 2, optimization can be an option to improve performance.

7.2. Future work

Future work should focus on following issues:

1. The results obtained by using the methodology proposed for optimal hydraulic component selection can be improved by taking more component parameters into account.
2. Linearized models cannot represent different types of non-linear phenomenon accurately but can be pretty much approximate. Charge pressure dominates hydraulic configuration 1 and so does overlapping of areas of pilot operated check valves. Hence there is a need to represent each circuit configuration more accurately using nonlinear modelling.
3. Different types of controllers can be tested on two hydraulic circuits discussed. Different sets of transfer functions can be used in extension and retraction.

References

1. Q. Zhongyi, Q. Long and Z. Jinman, " Review of energy efficient direct pump controlled cylinder electro-hydraulic technology", *Renewable and Sustainable Energy Reviews,* vol. 35, pp. 336–346, 2014.

2. J. Zimmerman, M. Pelosi, C. Williamson and Ivantysynova, "M. Energy consumpion of an LS excavator hydraulic system", in *Proceedings ASME International Mechanical Engineering Congress and Exposition*, Seattle, WA, USA, vol. 1, pp. 117–126, 2007.

3. L. Wang, W.J. Book and J.D. Huggins, "A Hydraulic circuit for single rod cylinder", *ASME J. Dyn. Syst. Meas. Control,* vol. 134, pp. 1-11, 2011.

4. E. Jalayeri, A. Imam and N. Sepehri, "A throttle-less single rod hydraulic cylinder positioning system for switching loads", *Case Stud. Mech. Syst. Signal Process,* vol. 1, pp. 27–31, 2015.

5. E. Jalayeri, A. Imam, T. Zeljko and N. Sepehri, "A throttle-less single-rod hydraulic cylinder positioning system: design and experimental evaluation", *Adv. Mech. Eng.*, vol. 7, pp.1–14, 2015.

6. A. Imam, M. Rafiq, E. Jalayeri and N. Sepehri, "Design, implimantation and evaluation of a pump-controlled circuit for single rod actuators", *Actuators,* vol 6(1), pp. 10-15, 2017.

7. R. Rahmfeld and M. Ivantysynova, "Developing and control of energy saving hydraulic servo drives", in Proceedings of the first *FPNI-PhD symposium*, Hamburg, pp.167–180, 2000.

8. J. Li, Y. Fu, Z. Wang and G. Zhang, "Research on fast response and high accuracy control of an airborne electro hydrostatic actuation system", in *2004 international conference on intelligence, mechatronics and automotion*, Changdu, China, 2004.

9. Z. Quan, L. Quan and J. Zhang, "Review of energy efficient direct pump controlled cylinder electro-hydraulic technology", *Renewable and Sustainable Energy Reviews*, vol. 35, pp. 336–346, 2014.

10. KG. Cleasby and AR. Plummer "A novel high efficiency electrohydrostatic flight simulator motion system", *Fluid power and motion control (FPMC 2008),* pp. 437-449, 2014.

11. A. Hewett, "Hydraulic circuit flow control", US Patent 5,329,767, 19 July, 1994.

12. R. Rahmfelda and M. Ivantysynova, “Displacement of controlled linear actuator with differential cylinder—a way to save primary energy in mobile machines”, in Proceedings of the Fifth *International Conference on Fluid Power Transmission and Control*, Hangzhou, China, vol 3–5, pp.296-301, April 2001.

13. H. Calishan, T. Balkan and B. E. Platin, "A complete analysis and a novel solution for instability in pump controlled asymmetric actuators", *Journal of Dynamic Systems, Measurement, and Control*, vol. 137, pp. 1-14, 2015.

14. C. Williamson and M. Ivantysynova, “Pump mode prediction for fourquadrant velocity control of valveless hydraulic actuators”, in Proceedings of the 7th JFPS *International Symposium on Fluid Power*, Toyama, Japan, vol.15–18, pp. 323–328, September 2008.

15. G. Altare and A. Vacca, “Design solution for efficient and compact electro-hydraulic actuators”, in Proceedings of the *Dynamics and Vibroacoustics of Machines* (DVM2014), Samara, Russia, pp.15–17, September 2014.

16. L. Ali, S. L. Sabat, and S. K. Udgata, “Particle swarm optimisation with stochastic ranking for constrained numerical and engineering benchmark problems”, *International Journal of Bio-Inspired Computation*, vol. 4, pp. 155–166, 2012.

17. C. C. Tseng, J.G. Hsieh and J. H. Jeng, “Active contour model via multi-population particle swarm optimization”, *Expert Systems with Applications*, vol. 36, pp. 5348–5352, 2009.

18. X. Fu, W. Liu, B. Zhang and H. Deng, “Quantum behaved particle swarm optimization with neighborhood search for numerical optimization”, *Mathematical Problems in Engineering*, vol.2013, pp.1-10, 2013.

19. V.L. Huang, P.N. Suganthan and J.J. Liang, “Comprehensive learning particle swarm optimizer for solving multiobjective optimization problems”, *International Journal of Intelligent Systems*, vol. 21, issue2, pp. 209-226, Feb 2006.

20. H. Han, W. Lu and J. Qiao, “An adaptive multiobjective particle swarm optimization based on multiple adaptive methods*”, IEEE Transactions on Cybernetics*, vol.47, pp. 9-17, Sept.2017.

21. K. Butt, R.A. Rahman, N. Sepehri, and S. Filizadeh, “ Globalized and bounded nealder-mead algorithm with deterministic restarts for tuning controller parameters; method and application”, *Optimal Control Applications and Methods*, vol.38, pp. 1042-1055, March 2017.

22. R. Chelouah and P. Siarry, “Genetic and nelder-mead algoritms hybridized for a more accurate global optimization of continuous multiminima functions”, *European Journal of Operational Research*, vol. 148, Issue 2, pp. 335-348, July 2003.

23. J.A. Guin, “Modification of complex method of constrained optimization”, *The Computer journal*, vol.10, pp. 416-417, 1968.

24. A. Alleyne and R. Liu, “Systematic control of a class of nonlinear systems with application to electro hydraulic cylinder pressure control”, *IEEE Transaction on Control System Engineering*, vol. 8, pp. 623-634, 2000.

25. N. Niksefat and N. Sepehri, “Robust force controller design for a hydraulic actuator based on experimental input-output data,” *Proceedings of the American Control Conference*, vol. 5, pp. 3718-3722, 1999.

26. N. Niksefat and N. Sepehri, “Design and experimental evaluation of a robust force controller for an electro-hydraulic actuator via quantitative feedback theory”, *Control Engineering Practice*, vol. 8, pp. 1335-1345, 2000.

27. N. Niksefat and N. Sepehri, “Designing robust force control of hydraulic actuators despite system and environmental uncertainties”, *IEEE Control Systems Magazine*, vol. 21, pp. 66-77, 2001.

28. M. Clerc and J. Kennedy, “The particle swarm: explosion, stability and convergence in a multi-dimentional complex space”, IEEE transactions on evolutionary computation, vol.6, pp. 58-73, 2002.

29. J. Kennedy, C. Sammut and G.I. Webb “Particle swarm optimisation”, in Encyclopedia of machine learning springer, 2011.

30. G. Ren, J. Song and N. Sepehri, “Fault-tolerant actuating pressure controller design for an electro-hydrostatic actuator experiencing a leaky piston seal”, Journal of Dynamic Systems, Measurement and Control, vol. 139, page 6, 2017.

31. M.B. Tischler and R.K Remple, “Aircraft and rotorcraft system identification: engineering, methods with flight test examples”, *American Institute of Aeronautics and Astronautics, Reston, Virginia*. ISBN: 978-1563478376, 2006.